A NONLOCAL APPROACH TO STUDY QUASI BRITTLE FRACTURE WITH GRAPH BASED FINITE ELEMENT ANALYSIS

A Dissertation

by

HO YONG SHIN

Submitted to the Graduate and Professional School of
Texas A&M University
in partial fulfillment of the requirements for the degree of

DOCTOR OF PHILOSOPHY

Chair of Committee,	Junuthula N. Reddy
Committee Members,	Arun Srinivasa
	Prakash Thamburaja
	Thomas Lacy Jr.
	Mary Beth Hueste
Head of Department,	Guillermo Aguilar

December 2022

Major Subject: Mechanical Engineering

ABSTRACT

Concrete is the most widely used quasi-brittle material in building and infrastructure constructions. Such structures can be exposed to various types of load conditions. Some of these can potentially result in the catastrophic fracture of such structures. Hence, it is imperative to study and understand the damage behavior of quasi-brittle materials in order to design the most optimal concrete-material composition and structure to prevent total failure of the structure.

Various numerical models have been developed over the years to describe the characteristics of damage behavior in quasi-brittle materials. However, the following limitations exist with proposed models: (a) in extended finite element method (XFEM), a special finite element is required rather than using existing conventional finite elements; (b) in peridynamics, a substantial reformulation of the conventional balance laws introduces additional complexity; and (c) in phase field model, a crack closure behavior is described with a complex energy decomposition.

In this thesis, a multiple cracking model is developed to overcome the the limitations of these existing models, where the model is formulated using the thermodynamically-consistent two- and three-dimensional Graph-based Finite-Element Analysis (GraFEA) framework. The key features of the model are as follows: (a) there is no need to reformulate the fundamental balance laws, (a) a discrete number of microcrack planes are introduced at each material point to describe a probabilistic description of damage evolution, (c) a purely kinematic approach to representing crack opening and closing is introduced, and (d) conventional elements typically found in the libraries of existing finite-element codes can be used to mesh the structures.

The developed theoretical and computational approach has been used to simulate concrete fracture under quasi-static and low-speed impact conditions. Also, a fracture length scale controlled gypsum-based composite material is fabricated to study the fracture behavior under impact loading conditions. The obtained experimental data are used in the validation of the three-dimensional non-local GraFEA simulation. The crack patterns and load-time curves from the simulation are matched well with the experimental data.

DEDICATION

To my parents and wife, for their unconditional love and support.

ACKNOWLEDGMENTS

First and foremost, I want to thank Dr. J. N. Reddy for being my advisor. Throughout my doctoral studies, his support, patience, and mentoring have been an enormous encouragement. His passion for research has always inspired me to drive my research. Also, I sincerely cherish his words and advice on how to live a meaningful life both as an engineer and a responsible societal member. I would like to take this moment to express my sincere gratitude to Professor Reddy to welcome me to his research group and guide me to finish my doctoral studies.

And I would like to thank my committee members, Dr. Arun Srinivasa, Dr. Prakash Thamburaja, Dr. Thomas Lacy Jr., and Dr. Mary Beth Hueste, for their support and crucial feedback on my dissertation. The work that has been carried out in this dissertation would never be achieved without the technical guidance of Drs. Arun Srinivasa and Prakash Thamburaja.

Dr. Prakash Thamburaja provided me special support throughout my doctoral degree study. He taught me how to implement a material model in the commercial finite element analysis software and knowledge about nonlocal fracture analysis. I truly enjoyed every moment of working with him and his teaching was a great help to conduct my research. I would like to express my sincere gratitude to him for his thoughtful guidance throughout my dissertation study.

I'm truly grateful to my colleagues in the Center of Innovation in Mechanics for Design and Manufacturing for being good friends throughout my graduate student life. I will miss the times we had together either at the helpful group meetings or during the lab social times.

Finally, I want to express my love and gratitude to my family. Their love and support is the major source for continuing my doctoral studies and completing this dissertation work.

CONTRIBUTORS AND FUNDING SOURCES

Contributors

This work was supported by a dissertation committee consisting of Professor J. N. Reddy (as the advisor), Professor Arun Srinivasa (as a member), Professor Prakash Thamburaja (as a member), Professor Thomas Lacy Jr. (as a member) of the Department of Mechanical Engineering, and Professor Mary Beth Hueste (as a member) of the Department of Civil Engineering.

The theoretical formulation of the multiple cracking model and GraFEA framework were developed by Professors J. N. Reddy, Arun Srinivasa, and Prakash Thamburaja. All other work conducted for the dissertation was completed by the student independently.

Funding Sources

Financial support for this research work was provided by O'Donnell Foundation Chair IV at Texas A&M University, the Engineering Research and Development Center (ERDC), the Army Futures Command, and the Graduate Teaching Assistantship from the College of Engineering at Texas A&M University.

TABLE OF CONTENTS

Page

LIST OF FIGURES

FIGURE Page

LIST OF TABLES

TABLE Page

1. INTRODUCTION AND LITERATURE REVIEW[1]

Concrete is the most widely used quasi-brittle solid in the construction of buildings and various infrastructure projects [1]. The primary role for the concrete portion of a structure is to support the loads on the structure and also to protect the structure from failing under various load conditions. In particular, dynamic-load conditions, where the loading duration is short but with a high-intensity force, can be a severe cause for the total failure of a concrete structure. Examples of dynamic load conditions are impact from a projectile, explosion, or wave propagation caused by earthquakes. Therefore, it is crucial to study and understand the damage behavior of quasi-brittle material, especially concrete, under quasi-static and dynamic loading conditions in order to design the most optimal concrete material composition and structure to have high energy-absorption to prevent total failure of the structure.

1.1 Characteristics of quasi-brittle material fracture

Figure 1.1 shows a typical response of a concrete sample under a low-strain rate tensile deformation. The appreciable nonlinear response prior to reaching peak stress after the initial linear elastic response is caused by microcracking in the concrete sample. That is, at some point before reaching the peak stress, microcracks begin to localize into a macro-crack that eventually propagates post-peak stress deformation [5]. Under displacement-controlled conditions, the displacement during the post-peak stage consists of opening of the macro crack accompanied by stress relaxation. Strain softening is observed under steady-state propagation of such cracks (see Fig. 1.1). It should be noted that the strain-softening response is a dominant feature of the concrete response.

For a microscopic description of the fracture and cracking process in quasi-brittle materials, it can be aided by the illustrations shown in Fig. 1.2 [4]. Cracks in concrete may generally evolve

[1]Reprinted from the original reference of "Experimental, theoretical and numerical studies on plain concrete fracture in the low-strain rate regime—A state-of-the-art review" by Ho Yong Shin, Carson Lawrence, Kalyan Raj Kota, Prakash Thamburaja, Arun Srinivasa, Thomas E. Lacy Jr., and Junuthula Reddy, 2021. *Mechanics of Advanced Materials and Structures* , 1-45, https://doi.org/10.1080/15376494.2021.2011501.

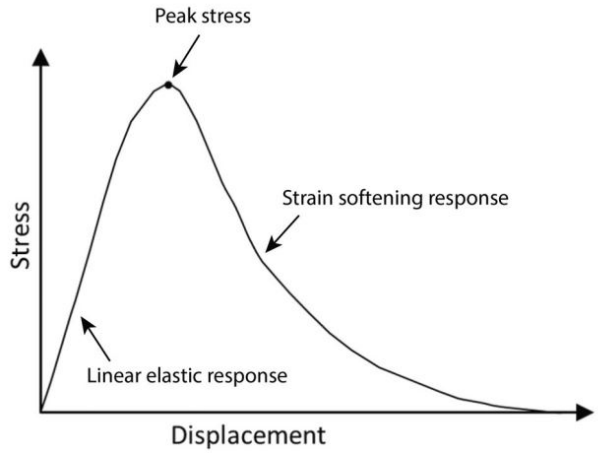

Figure 1.1: Typical concrete response subjected to tensile loading. The highlighted portions of the stress-displacement curve provide information regarding the linear elastic stiffness (typically within 30% of the peak load [2]), the peak stress and strain-softening characteristics of the material [3].

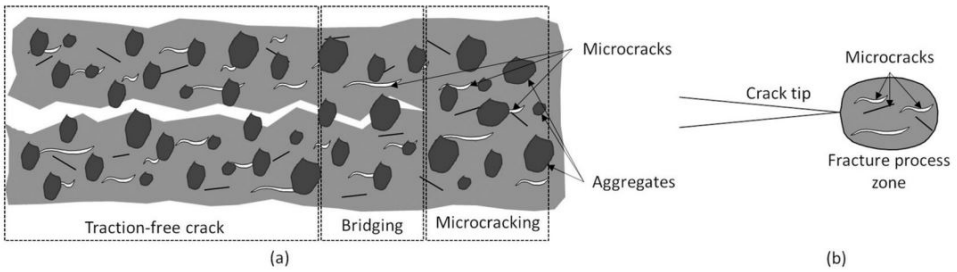

Figure 1.2: Concrete fracture [4]: (a) A schematic figure of crack growth (b) Strain softening fracture process zone.

from pre-existing numerous flaws[2], such as air pockets, pre-cracked aggregates, weak bonds between aggregates and matrix. When the material in a given structure reaches its maximum tensile strength, cracking will occur. Cracks generally propagate in a direction following the weakest resistance in the material. As shown in Fig. 1.2(a), microcracks form ahead of a macroscopic crack, which consists of a bridged crack directly behind the tip with traction-free crack faces further behind the tip [6]. As cracking occurs, the fracture front is blunted by a region of microcracking typically referred as *fracture process zone* (FPZ, shown in Fig. 1.2(b), see also the work of Bazant [7]). From Fig. 1.2, it can be clearly seen the microscopic complexity of the fracture process in concrete, and a significant number of experimental and theoretical/numerical works have been devoted to characterizing the macroscopic and microscopic aspects of concrete fracture.

Cementitious materials like concrete are highly heterogeneous by design. Such materials generally exhibit high compressive strength, low tensile strength, and brittle failure under tensile loading. They also display a highly nonlinear stress-strain behavior in compression and flexure, which is mainly attributed to an imperfect bonding between the aggregate particles and the cementing paste. Crack growth analysis of concretes have shown the presence of microcracks prior to loading. The population of microcracks evolves (in size and number of cracks) with load application. The crack propagation in concrete is accompanied by a process zone of variable size [4]. Several approaches such as statistical [8], energetical, and fractal theories have been analyzed by Carpinteri *et al.* [9] to study the size-scale effects on the strength and toughness of the concrete. However, the application of statistical approaches were limited due to lack of reliable experimental data at the time [8]. The effects of microstructural parameters such as aggregate size, and macroscopic parameters, such as specimen dimensions, on the brittle fracture of concrete have been experimentally investigated by Issa *et al.* [10] and was observed that the fracture energy was proportional to the size of the specimens and maximum aggregate size. The presence of aggregates dictates the tortuosity of fracture paths and the fracture toughness. Such effects of specimen size and aggregate

[2]Here, the terms “crack" and “flaw" are used interchangeably. All cracks can be considered flaws but not all flaws can be considered as cracks. The distinction is the sharpness of the crack tip, a crack being with a very small radius of curvature.

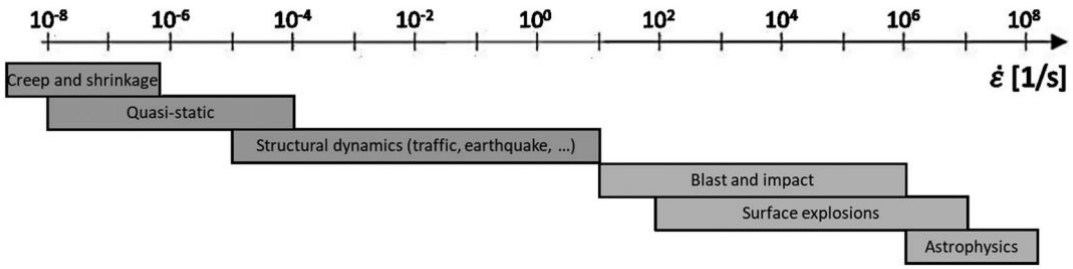

Figure 1.3: Physical events associated with the magnitude of strain-rate. Note that the low strain-rate regime encompasses structural dynamics events such as vehicle traffic and earthquake loading [4] which significantly affects concrete-based civil structures.

size have been analyzed by applying fracture mechanics formalisms by Issa *et al.* [11]. When a growing crack reaches an aggregate, it either goes around or penetrates through it. Since the fracture energy of the interface is typically smaller than the fracture energy for the aggregate [10, 11], a crack more often travels around the aggregate resulting in bridging (*cf.* Fig. 1.2). Large aggregate sizes will result in higher fracture toughness due to there higher surface area which provides higher bond strength between the aggregates and the cement. The size dependence of the fracture energy has also been analyzed and validated by Bazant *et al.* [12].

Generally, the fracture behavior exhibited by concrete can be broadly categorized into two regimes: (1) the fracture exhibited in the low strain-rate regime (which encompasses creep fracture, quasi-static fracture, and structural dynamics-based fracture induced by vehicle traffic and earthquake loading) and (2) fracture exhibited in the high-strain rate regime (which encompasses blast/impact events and surface explosions). This information is succinctly displayed in Fig. 1.3.

1.2 Experimental method for describing quasi-brittle material fracture

The focus of this section is to examine various quasi-static mode I and mixed-mode fracture experimental methods from the literature for plain concrete. An overview of the experimental methods for characterizing concrete fracture is covered in this section.

Concrete mode I fracture testing on concrete is carried out either directly by applying a tensile load orthogonal to the desired crack direction, or it is done indirectly by applying a different load-

ing scheme (such as compression or bending load) that will result in tensile stresses orthogonal to the crack direction. Several variants of both direct tensile tests and indirect tensile tests have been proposed, and a selection of them are described herein. These tests have been used to provide Young's moduli, Poisson's ratios, fracture toughness, crack paths, stress-strain relationships, *etc.* to characterize concrete material properties, which is necessary for the validation of various numerical models. Mixed-mode fracture is recognized to be one of the most frequent failure modes of concrete structures [13]. This mode is a combination of opening and shearing fracture, and its study is very important to fully understand the quasi-static fracture behavior of concrete. This generally involves the application of both a tensile load and a shear load sequentially or simultaneously. Following the review of the experimental methods, a summary of advantages and disadvantages of the experimental methods is presented at the end of the section.

1.2.1 Direct opening mode fracture

A fundamental experimental procedure for characterizing fracture of quasi-brittle material is through a simple tensile testing with Mode I fracture. A basic version of these tests, known as the notched prism test method, consists of one end of a specimen being fixed while a tensile load is applied to the other end. A simple specimen geometry for this test method is a prism, typically rectangular in cross-section. However, a plain prism does not provide *a priori* knowledge of the location a crack will begin from; thus, to provide a starting point for crack propagation, Gopalaratnam *et al.* [14] proposed the addition of one or more notches in the midsection of the prism. This provides controlled, easily observable crack growth with a clear starting point. A diagram of a typical testing setup is shown in Fig. 1.4.

Hordijk [3] performed quasi-static tensile experiments on notched prism specimens by gluing the samples of various dimensions to end plates that were then fixed to the testing rig. These samples were tested in displacement-control with a loading rate of 0.8 μm/s (over a length of 50 mm) to obtain a quasi-static stress-displacement relationship. Displacement was measured with extensometers affixed to the corners of the specimens. The effects of specimen length and cross-sectional area at the notch were observed through four geometries: Types A, B, C, and D. Types

A, B, and C had cross-sectional areas $s_2 \times a$ (see Fig. 1.4) of 60×50 mm^2 ($s_1 \times a$ of 50×50 mm^2 at the notch) and lengths of 250, 125, and 50 mm, respectively. Type D had the same length as type A of 250 mm, but it had a reduced cross-sectional area of 50×40 mm^2 (40×40 mm^2 at the notch). The stress-displacement curves of these tests are seen in Fig. 1.5. It can be seen that the concrete shows very stiff behavior pre-peak load, and then a softening response post-peak load. Hordijk attributes the deviation of type C (the shorter specimen) to the influence of the much stiffer end plates preventing lateral displacements (and therefore increasing the rotational stiffness) on the specimens with a small length. Hordijk also notes that the shorter specimens (B,C) showed more uniform crack trajectory perpendicular to the loading direction, while the longer specimens (A,D) exhibited more nonuniform crack trajectory. This was attributed to the higher rotational stiffness of the shorter specimens.

Sorelli *et al.* [15] performed uniaxial tensile experiments on concrete specimens of $100 \times 200 \times 40$ mm^3 with a single triangular notch of depth 15 mm. The tests were conducted with a displacement controlled method at the crack mouth opening with a rate of 1 μm/min before the

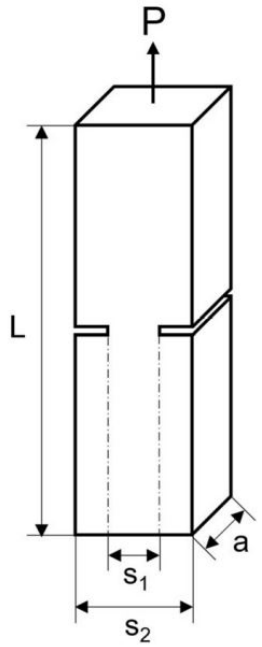

Figure 1.4: Geometry and loading conditions for a tensile notched prism sample [14].

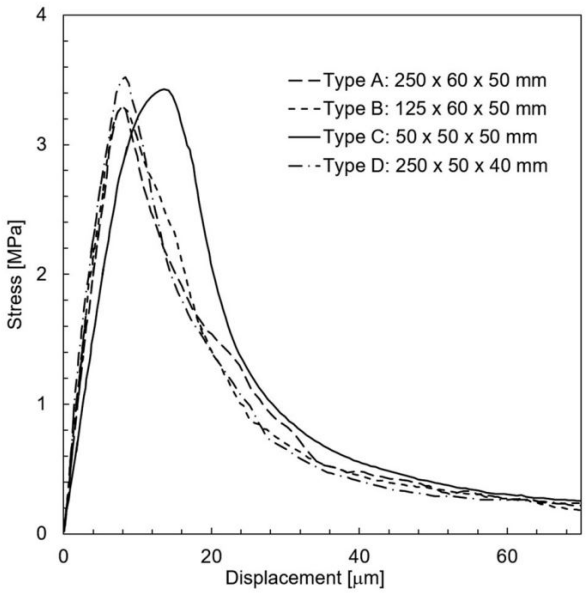

Figure 1.5: Stress-displacement curves for the notched prism test from Hordijk [3]. The quasi-brittle nature of the concrete is seen in the very stiff response before the peak load and the gradual softening response after the peak load.

peak load and 2 μm/min after the peak load. For a description regarding other works on uniaxial tensile experiments on plain concrete, please refer to [16].

A drawback of testing notched specimens is the introduction of a nonuniform stress distribution around the notch. To avoid this, Ren and Houben [17] devised a tensile test method on unnotched cylinders. The specimen geometry, shown in Fig. 1.6 [17], minimizes stress concentrations with its second order parabolically varying cross-section. The specimens were glued to endcaps that were affixed to the test rig to ensure an even distribution of load transfer. The purpose of the tests was to observe the effects of curing age of plain concrete; thus, ages of 1, 2, 3, 5, 7, 14, 28, and 90 days were tested. Aggregate size effects were also studied with one set of specimens containing a maximum aggregate size of 6.3 mm and a second set containing a maximum aggregate size of 16 mm (denoted as "type 6.3" and "type 16", respectively). The quasi-static tests were displacement controlled with a rate of 0.1-0.05 μm/s depending on the age of the specimen being tested. Some examples of the force-displacement responses for both aggregate types is shown in Fig. 1.7, and an example of the crack propagation is shown in Fig. 1.8. It can be seen that for both

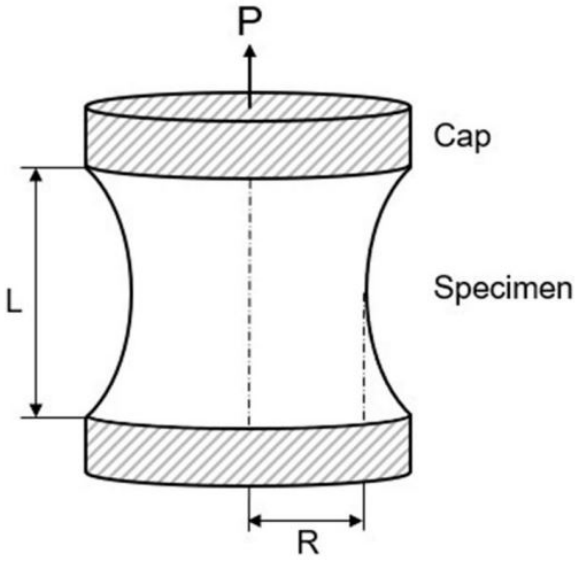

Figure 1.6: Geometry and loading conditions for an unnotched cylinder test [17]. The length $L =$ 90 mm, and the radius $R = 50$ mm at the center and 80 mm at the ends.

types 6.3 and 16, a longer curing age resulted in significantly higher peak loading and pre-peak load stiffness. However, longer curing age also resulted in a more brittle response in the post-peak load region.

Van Vliet *et al.* [18] performed uniaxial quasi-static tensile tests on dog bone-shaped prismatic specimens of plain concrete, with the geometry shown in Fig. 1.9. The specimens were glued to load platens. The tests were displacement controlled to study the structural size effect on the nominal strength and the fracture energy. To do this, various sizes were tested, with d values ranging from 50 to 1600 mm and r values ranging from 36.25 to 1160 mm. Also studied was the effect of moisture on the concrete by curing a "wet" series of specimens at higher humidity and applying moist cloths on the specimens prior to testing. The displacement rate of 0.028 μm/s was applied until the linearly varying displacement transducers (LVDTs) reached the maximum range of 500 μm. Because of this limitation, the large "wet" specimens were not taken to their ultimate load before the test was concluded. Force-displacement curves for the tests are shown in the cited paper. The larger specimens showed much higher peak loads in all cases, and the smallest specimens showed the largest deviations in repeated tests. Van Vliet *et al.* attribute these

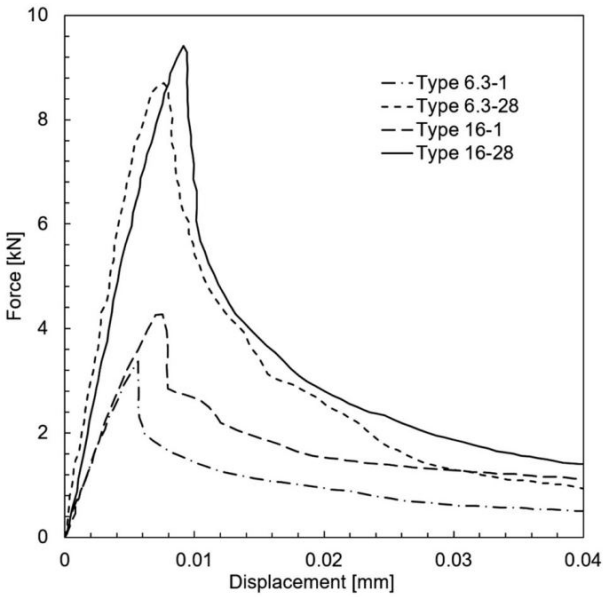

Figure 1.7: Load-displacement curves for unnotched cylinder test from Ren and Houben [17]. The "-1" and "-28" refer to specimens cured for 1 day and 28 days, respectively. The "6.3" and "16" refer to maximum grain size. Note that the longer curing time leads to much higher peak stresses but a much steeper drop-off, indicating a more brittle response. Furthermore, a larger maximum grain size leads to a higher peak load prior to strain-softening.

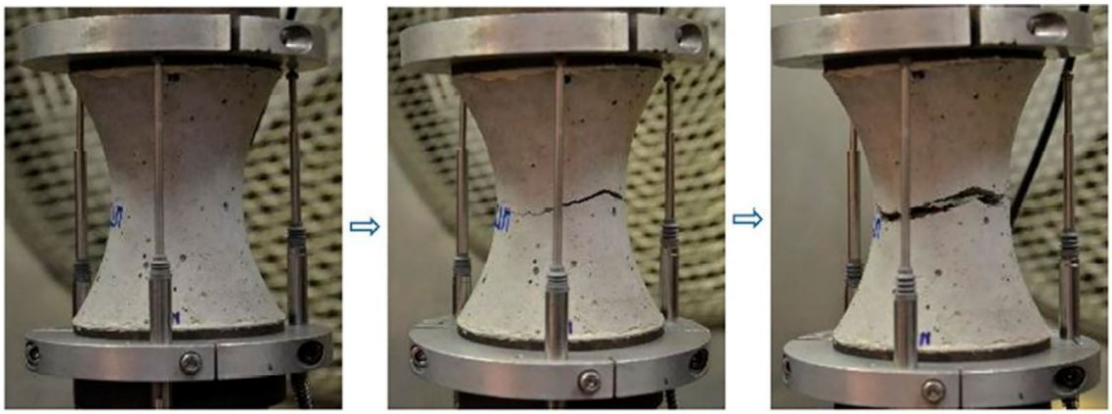

Figure 1.8: Crack propagation for an unnotched cylinder test from Ren and Houben [17].

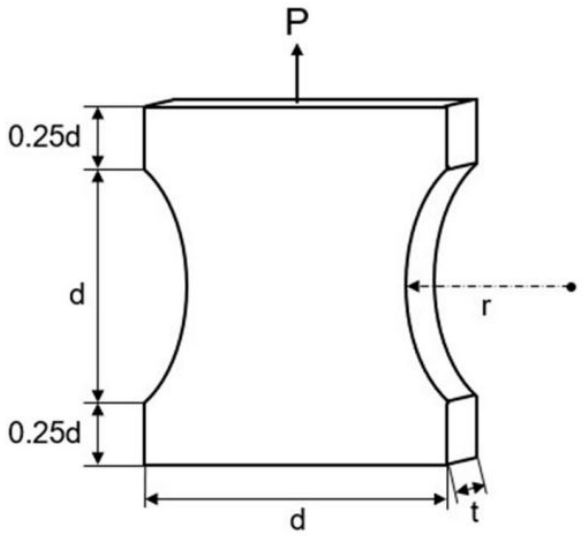

Figure 1.9: Geometry and loading conditions for a dog bone specimen test [18]. The lengths $d =$ 50, 100, 200, 400, 800, and 1600 mm, corresponding to the radii $r =$ 36.25, 72.5, 145, 290, 580, and 1160 mm respectively. The thickness t for all samples was 100 mm.

large deviations to the larger relative size of the aggregates in the fracture region of the smaller specimen size leading to less uniformity in the stress at the fracture region. The “wet" specimens showed lower strength values when compared with the “dry" specimens. This could be caused by internal stresses resulting from differential shrinkage as the specimens begin to dry out.

A common test method for the characterization of fracture in metals is the compact tension test method, in which square-shaped notched specimens are loaded in tension via internally attached rods. Fernández-Canteli *et al.* [19] proposed the modified compact tension test method to characterize fracture of concrete. The specimens used for this test method are disc-shaped with a standard diameter of 150 mm and a notch cut along the radial direction of the specimen from the edge to a point near the center. Holes are then drilled in the specimen perpendicular to the notch, and two steel bars are glued to the two halves created by the notch. This setup can be seen in the schematic shown in Fig. 1.10. The rods are pulled in tension, resulting in crack growth from the tip of the notch. A displacement-controlled loading scheme is used with a rate of 0.5 mm/min. An example of the generated crack path for these experiments is shown in Fig. 1.11. The concrete specimen shows very stiff behavior before the peak load is reached and then a gradual softening

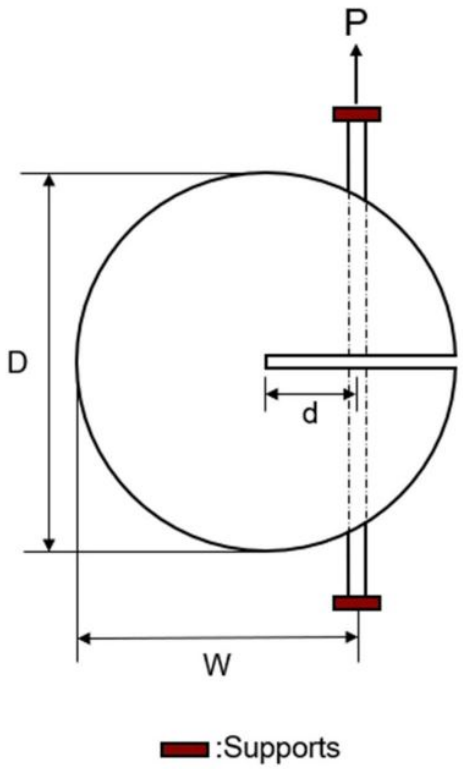

Figure 1.10: Geometry and loading conditions for a modified compact tension test [19]. The specimen diameter $D = 153$ mm, the length of $W = 116.4$ and 114.3 mm, the length of $d = 40.2$ and 32.9 mm, the radius of the rods was 8 mm, and the specimen thickness was 63.5 and 68.6 mm.

once fracture occurs at the peak load.

1.2.2 Indirect opening mode fracture

The cracked chevron notched Brazilian disc (CCNBD) test method can be applied to study both mode I and mode II fracture [20]. This test is performed on disc-shaped specimens with a chevron notch cut along the radial direction extending in opposite directions at the center of the specimen. The specimen is then subjected to a compression load along the radial direction, and the orientation of the notch with respect to the loading points (defined as angle β) determines the mode of fracture being tested. Wei *et al.* [20] performed mode I and mode II CCNBD tests with the geometry shown in Fig. 1.12. The angle β used for the mode II tests was determined by Wei *et al.* to be 28°. The team used a displacement-controlled load rate of 0.005 mm/min. Examples

Figure 1.11: Crack propagation for a compact tension test from Fernández-Canteli *et al.* [19].

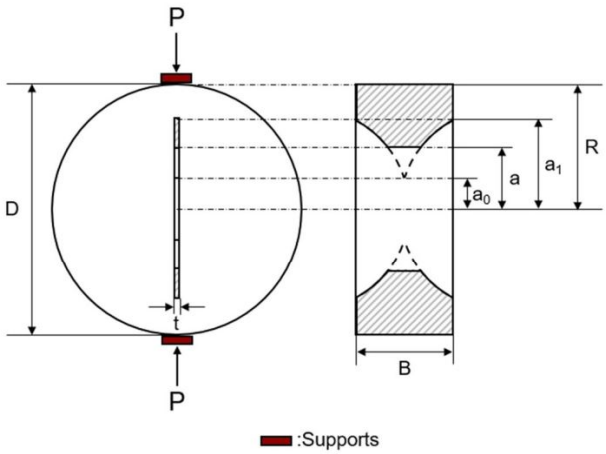

Figure 1.12: Geometry and loading conditions for a mode I ($\beta = 0°$) cracked chevron notched Brazilian disc test [20]. The dimensions tested were $R = 36.9$ mm, $a_0 = 9$ mm (average), $a_1 = 26.8$ mm (average), and $B = 30.2$ mm (average).

of force-displacement curves for both modes are shown in Fig. 1.13, and typical crack propagation paths are shown in Fig. 1.14. The curves do not approach zero load at the end due to unstable crack growth splitting the specimen into two halves, at which point the test was concluded.

The three-point bend test (TPBT) method is used as an indirect method of studying the mode I

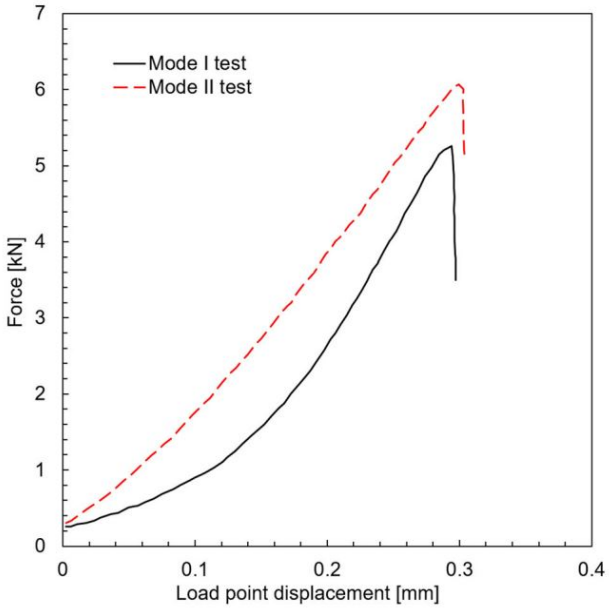

Figure 1.13: Load-displacement curves for the Brazilian disc test with mode I and mode II load application from Wei *et al.* [20]. This experimental data suggests that the peak load is sensitive to testing modes whereas the applied displacement where cracking occurs is insensitive to testing modes.

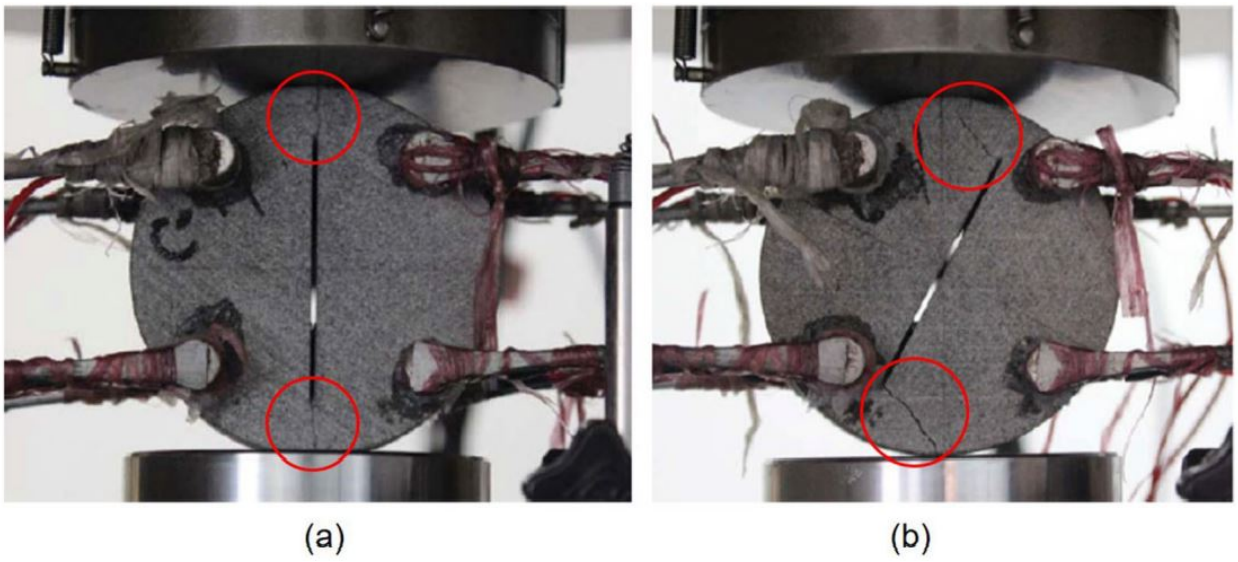

Figure 1.14: Crack propagation for a Brazilian disc test from Wei *et al.* [20], where (a) shows a mode I test and (b) shows a mode II test.

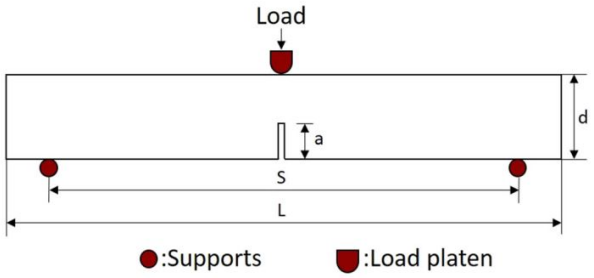

Figure 1.15: Geometry and loading conditions for symmetric three-point bending test [23].

concrete fracture [21]. The limitations of uniaxial tensile test methods, such as rotation of the end platens, load eccentricity, and a nonuniform glue bonding of concrete specimens with end platens, can be circumvented with this method. A stable analysis was achieved by placing the specimen on two supports and applying the load at the midspan of the beam. Sufficient machine stiffness is important to obtain the stable fracture of a concrete specimen, where the stiffness of the machine has to be greater than the steepest slope of the softening part of the force–deflection curve [22]. From the data obtained by the conducted uniaxial tensile test, the characteristic length l_{ch} of the beam for conducting a stable bending test was determined with the Eq. (1.1)

$$l_{ch} = \frac{EG_f}{f_t^2} \tag{1.1}$$

where G_f is the fracture energy, E is Young's modulus, and f_t is the tensile strength [23]. The stiffness of the testing machine was determined with the consideration of a specimen size and calculated specimen characteristic length [22]. The rectangular TPBT specimen has a machined notch starting from the bottom of the surface at the center of beam. The standard shape of the specimen is shown in Fig. 1.15. The load cell attached to the bottom of the steel actuator measures the applied load and a clip gauge attached to the notch provides a crack mouth opening displacement (CMOD) value. The CMOD value was used as a feedback signal to ensure a constant cross-head displacement rate.

Bažant [24] performed a series of tests to study the size effect and fracture energy of concrete

and mortar specimens. The nominal standard strength of structure is size independent in plastic limit analysis or elasticity with strength limit. However, in the case of quasi-brittle material such as concrete, the nominal strength depends on a size of structure [25]. A size effect law is an equation derived from dimensional analysis to describe effects of specimen size and maximum aggregate size on the nominal strength at failure, where the law considers the length of the FPZ as a constant material property. A different length of FPZ will result in different failure behavior according to the size effect law. To study the effect of specimens size, four different values of beam depth ($d = 1.5, 3, 6,$ and 12 in) were used in each type of test specimen. The length, span and notch depth of the specimen were decided based on the beam depth as (length, span, notch depth = 8/3d, 5/2d, 1/6d). The notch width was 0.1 in. The thickness of the specimen was either 0.75 in or 1.5 in. The maximum aggregate size of 0.5 in. was used for concrete specimens. The maximum aggregate size of mortar specimens was 0.19 in. The study showed that the fracture energy was similar for three-point bending specimens, edge-notched specimens, and specimens under eccentric compression in both cases of concrete and mortar specimens. The analysis of the results with the size effect law showed that due to the difference in the size of the FPZ, the three different specimen types showed a different shape of size effect law graph. For the TPBT, the ligament of the specimen was experiencing both tensile and compressive stress states and the area of the ligament under the tensile stress was larger than the tensile stress ligament area of eccentric compression specimen. This induced a medium size of the FPZ of TPBT specimens and the plot of size effect law placed between the edge-notched specimen and the eccentric compression specimen.

Tang *et al.* [26] captured a full-field displacement of beam specimens with an electronic speckle pattern interferometry (ESPI) technology, which is using the interaction between two coherent laser beams. Two types of plain concrete were tested in this study: a high strength concrete (HSC) containing a superplasticizer and a normal strength concrete (NSC) having no plasticizer. Compressive strength of the HSC and NSC was 90 MPa and 40 MPa. The low water to cement ratio and added super plasticizer increase the strength of HSC. The specimen dimension used in the study was (length $\times$ depth $\times$ thickness $= 710 \times 150 \times 80$ mm^3) with 600 mm of clear span. The depth and

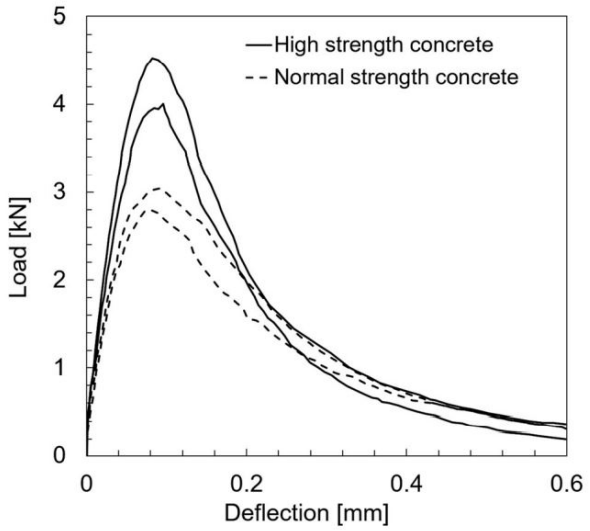

Figure 1.16: Load-deflection curves of the normal and high strength concrete [26]. The low water to cement ratio and added super plasticizer increase the strength of high strength concrete. The dimension of the beam was (length $\times$ depth $\times$ thickness = 710 $\times$ 150 $\times$ 80 mm^3) with 600 mm of clear span. The depth and thickness of notch were 45 mm and 3 mm. A load was given by a displacement controlled actuator with a rate of 0.01 mm/min.

width of the notch were 45 mm and 3 mm. The experiments were conducted by a displacement controlled method with an actuator applying load on a specimen. A loading rate for the experiments was 0.01 mm/min. The CMOD was measured with clip gauge at the notch and the midspan deflection was measured with a LVDT. The load-displacement curves from the experiments are shown in Fig. 1.16. The minimum and maximum values of experimental data are bounded by solid or broken lines of each concrete type in the figure. Due to the difference of the individual specimens and the heterogeneity of the concrete, the experimental results have not appeared as a single curve but bounded between two lines. As seen in the figure, the load-displacement curves from the HSC specimen show a higher peak load than the NSC due to the different mixture compositions. The FPZ was qualitatively studied through a measured strain field by ESPI. A fully developed FPZ length at the 33% of peak load in a post-peak region was nearly 2.7 times of the maximum aggregate size. Bažant presented similar result that the FPZ length, which is indicating uniformly distributed microcracks, would be 3 times of maximum aggregate size [27].

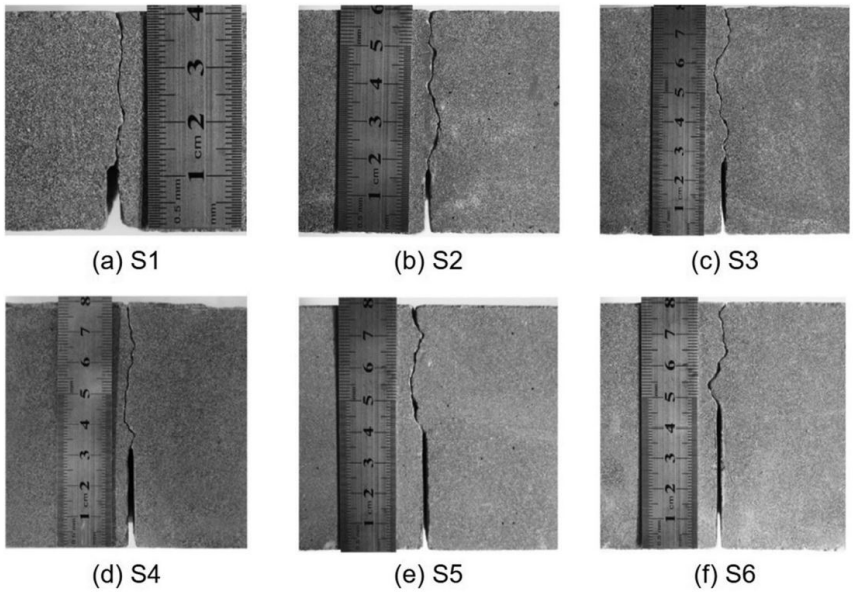

Figure 1.17: Crack path of specimens with various notch depths. The dimension of the specimens from S1 to S6 are shown in Table 1.1. A loading rate was 0.005 mm/min and controlled by the CMOD. All crack paths initiated at the notch tip and propagated through a center region of the beam [28].

Wu *et al.* [28] conducted TPBT to study the properties of FPZ in concrete using the digital image correlation (DIC) technique. The DIC technique compares a reference image with a deformed image of the specimen to measure a deformation in the domain. In this study, a digital camera with a resolution of 1024×768 was used and the camera captured the deformed image once per second until the failure of the specimens. Six different sizes of specimens were used in the test and the size information is shown in Table 1.1. The thickness of all the specimens was 40 mm. A load was given with a rate of 0.005 mm/min by the displacement controlled method. Four different notch-depth ratios of $\alpha = a/d = 0.3, 0.4, 0.5, 0.6$ were used to study the effect of notch depth size on fracture behavior of concrete. The study showed that the maximum length of the FPZ decreased as the notch depth to the specimen height ratio increased. The final crack trajectories of each specimen are shown in Fig. 1.17. The crack was initiated from the notch tip and spread out through the center portion of the beam.

Hordijk [3] proposed the four-point bending test (FPBT) method as a verification test for the

Table 1.1: Concrete specimens used in the study of Wu *et al.* [28]

Specimen	S1	S2	S3	S4	S5	S6
Span, S (mm)	160	240	320	320	320	320
Beam depth, d (mm)	40	60	80	80	80	80
Notch depth, a (mm)	12	18	24	32	40	48
a/d	0.3	0.3	0.3	0.4	0.5	0.6

uniaxial tensile test. The FPBT method was used in this study instead of TPBT, to avoid the disadvantage of TPBT, where the test introduced the compressive stresses in the fracture zone from the loading support which was parallel to the beam notch. The geometry and loading condition of the bending test are shown in Fig. 1.18. The depth d of the beam was 100 mm and three different depth of notches, $a = 10$, 30, and 50 mm, were tested at the beam bending station. The thickness and length L of the beam were 50 and 500 mm. LVDTs were attached to the concrete specimens to measure the deflection, while the average signal from the two LVDTs near the top surface was used as a control parameter of the testing machine. The deformation rate applied to the specimens was 0.16 μm/s. The load was measured at the load cell attached to the actuator and the deflection at the center of the beam was measured with two LVDTs. The material parameters of the concrete were measured from cube tests with a specimen size 150 mm^3 and a deformation-controlled uniaxial tensile tests. The load-deflection curves of the three different types of a notched specimen are shown in Fig. 1.19.

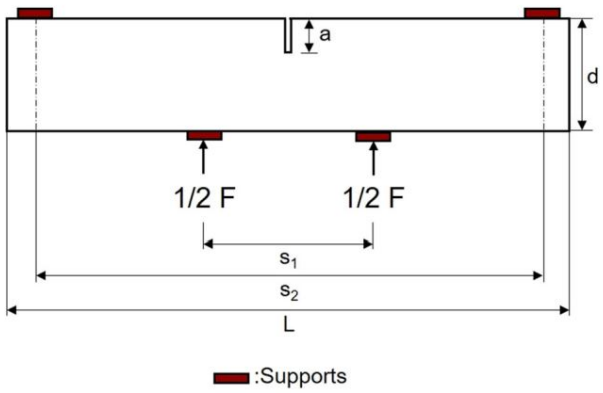

Figure 1.18: Geometry and loading conditions for four-point bending test [3].

Yin *et al.* [29] conducted FPBTs to study the fracture properties of concrete. The load given by the two load platens induced pure bending condition near the midspan notch section. Tensile crack propagation was initiated at the tip of the notch as the load increased. The specimen dimension used in the study was (length $\times$ depth $\times$ thickness = 1000 $\times$ 200 $\times$ 120 mm^3) with 800 mm of clear span. The notch size for each specimen was corresponding to a crack-depth ratios of 0.2, 0.3, 0.4, 0.5 and 0.6. The maximum size of the coarse aggregate used in the study was 20 mm. The compressive strength f_c and elastic modulus E of the concrete were 40.78 MPa and 32.46 GPa. The load was controlled by a constant midspan displacement of 0.05 mm/min. The midspan deflection was measured with LVDTs and the CMOD was measured using a clip gage. A crack propagation path for the specimen of each notch size are shown in Fig. 1.20. The crack propagation was started from a notch tip at all specimens. A deviation of the crack propagation path away from the notch plane was detected from the visual inspection of crack paths, where the influence of coarse aggregate on the crack propagation path could be the main reason for this deviation.

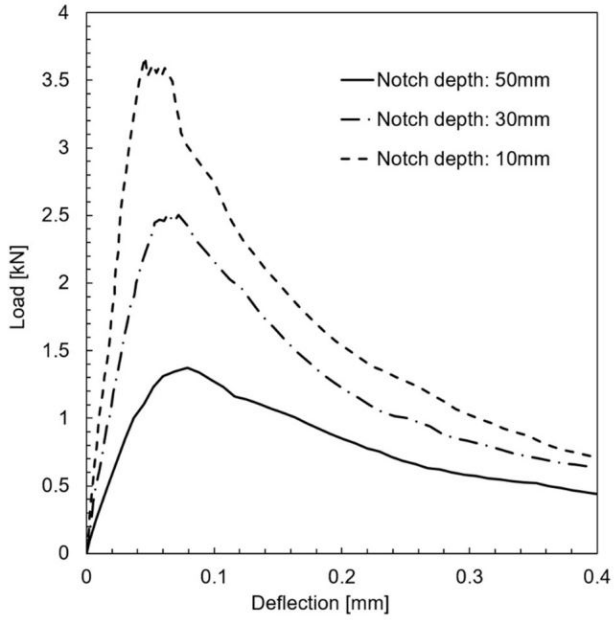

Figure 1.19: Load-deflection curves of the three different notched specimens under the monotonically increasing deflection [3]. The peak force increases with reducing notch depth. The dimension of the beam was (length $\times$ depth $\times$ thickness = 500 $\times$ 100 $\times$ 50 mm^3) with 450 mm of clear span. A rate of loading was 0.16 μm/s and an average deformation was used as a control parameter.

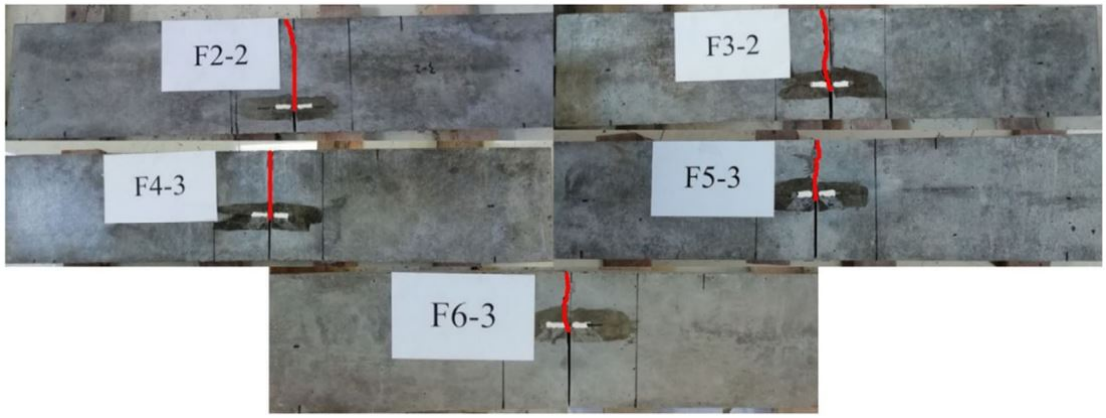

Figure 1.20: Crack propagation path of each specimen with different notch size. The dimension of the beam was (length $\times$ depth $\times$ thickness = 1000 $\times$ 200 $\times$ 120 mm^3) with 800 mm of clear span. The tests were displacement controlled with 0.05 mm/min of loading rate. All the specimens showed main crack propagation path at the center of a beam. Five different notch-depth ratio(0.2, 0.3, 0.4, 0.5, 0.6) were used in the experiments and labeled as (F2, F3, F4, F5, F6) [29].

For each experiment, a load-deflection and a load-CMOD curve were generated [29]. The load-deflection curves showed softening behavior after the peak load, where the specimens with the initial crack-depth ratios of 0.2 and 0.3 showed more brittle behavior due to a dissipation of relatively high amount of stored elastic energy at fracture, which is shown in the Fig. 1.21.

The gradual decrease of the maximum load was observed at the load-CMOD curves corresponding to the gradual increase of critical CMOD. The fracture energy of the different tests was calculated by using the area under the load-deflection curve. An exponential function was used to fit the load-deflection curves to calculate the area. Although the area under the load-deflection curve is getting large as the notch-depth ratio decreases, the increased crack surface area induced the calculated average fracture energy of specimens with different crack-depth ratio showed similar fracture energy. The total average value of the fracture energy of normal strength concrete was 201.285 N/m, which was similar with the results from other researchers.

1.2.3 Mixed mode fracture

A simple experiment devised to test mixed-mode fracture of concrete is a modified TPBT method. This was done by Wu *et al.* [13] using rectangular beams with a two-segmented notch,

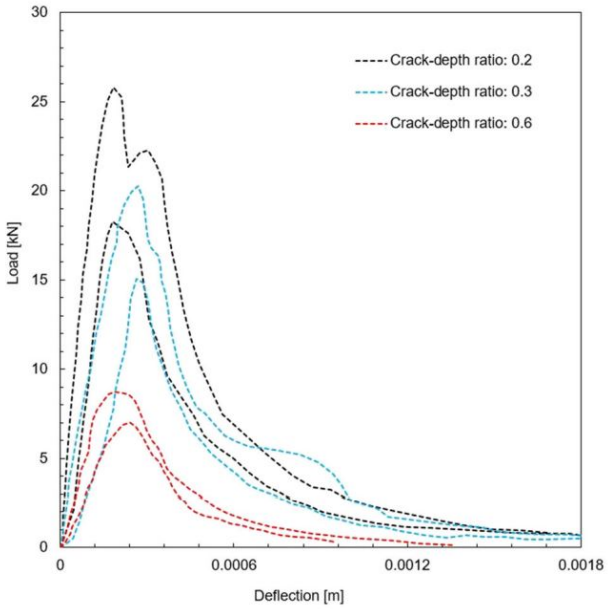

Figure 1.21: Load-deflection curves of the specimens with different crack-depth ratios. The experimental data are bounded by upper and lower limits with different colors for the different crack-depth ratios. Comparing to the result of a crack-depth ratio of 0.6, the case of crack-depth ratio of 0.2 and 0.3 show steeper decrease of load after the peak load [29].

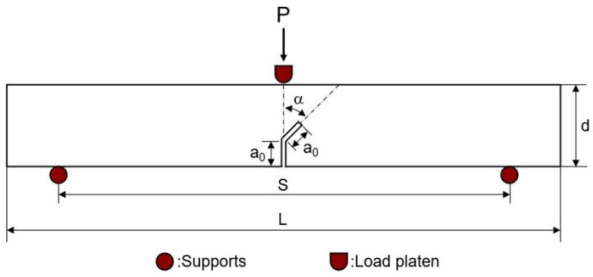

Figure 1.22: Geometry and loading conditions for a modified three-point bending test [13]. The dimensions tested were $L = 700$ mm, $S = 600$ mm, and $d = 150$ mm (ranges for a_0 and α are given in the text). The thickness was 40 mm.

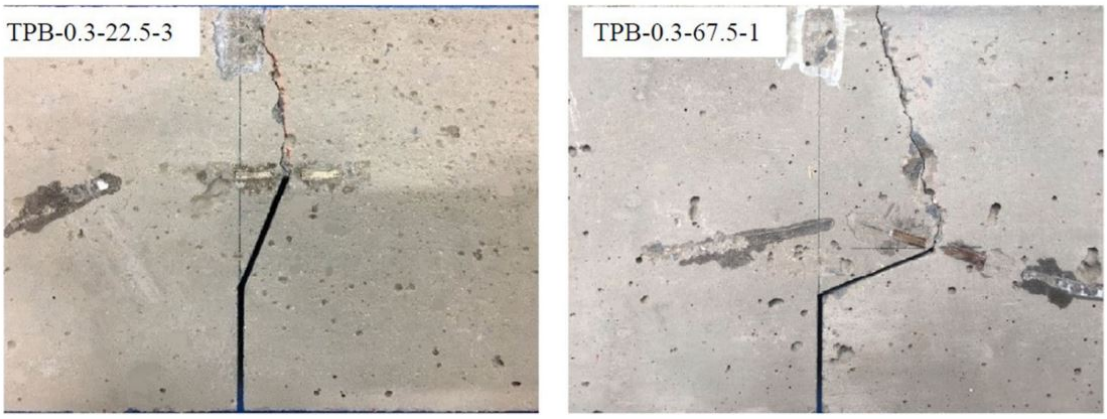

Figure 1.23: Crack propagation for a modified three-point bending test from Wu *et al.* [13]. These samples have $a_0 = 45$ mm and $\alpha = 22.5°$ (left) and $67.5°$ (right).

with the second notch segment measured at an inclination angle α with respect to the first notch segment, as seen in Fig. 1.22. The angle α can range from 0 to 90°. Wu *et al.* studied the behavior of specimens spanning a wide variety of inclination angles (0, 22.5, 45, 67.5, and 90°) and notch lengths (30, 45, 60, and 75 mm). The specimen geometries tested were $700 \times 150 \times 40$ mm^3. The team placed strain gauges at the notch tips and measured both CMOD and crack mouth shearing displacement (CMSD). Load-strain curves with respect to both CMOD and CMSD were obtained using a displacement controlled rate of 0.012 mm/min. The results can be found in the cited paper. For both CMOD and CMSD strains, the same brittle pre-peak load behavior and softening post-peak load behavior are shown. The crack paths (with the exception of some tests with an inclination angle of 90°) initiated at the tip of the inclined notch segment and grew toward the point of load application, which can be seen in Fig. 1.23.

Unlike the modified TPBT, the modified FPBT differs greatly from its mode I counterpart. Rather than applying the load symmetrically about a single notch in the specimen like the mode I test method, the mixed-mode specimens consist of two notches on opposite sides. The notches are the same dimensions and aligned with the center line of the specimen. The compressive load is then applied with the opposite sides being offset toward opposite sides, as shown in Fig. 1.24 [30]. The asymmetry of this setup results in shear cracking as well as opening cracking.

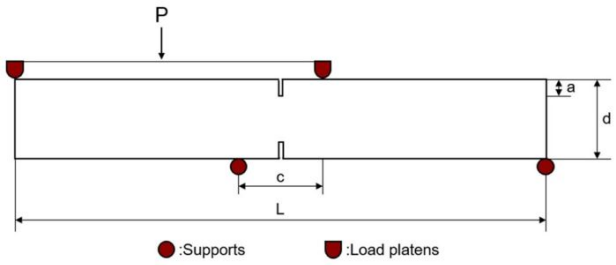

Figure 1.24: Geometry and loading conditions for a mixed-mode four-point bending test.

One of the earliest examples of this test method was performed by Bažant *et al.* [31] in the late 1980s. Other influential studies were carried out by Bocca *et al.* [30] in the following years. Swartz *et al.* [32] also performed similar experiments, as well as a modified version to include axial loading. Considering all these studies, there is much data on size effects of the specimens, size effects of the notches, and the effects of curing conditions. In all cases, experiments were carried out under displacement-controlled quasi-static loading conditions. In general, the observed crack paths initiate at the notch tips and grow in a curved fashion toward the middle load point on the opposing side of the specimen.

Winkler proposed the L shaped panel test method in his studies [33, 34]. In these studies, L shaped panels were affixed to the testing machine according to the configuration shown in Fig. 1.25. The lower edge was held as a fixed boundary condition, and the vertical support on the horizontal leg applied the tensile load. The tests were performed under displacement control of 0.02 mm/min. In addition to plain concrete, Winkler also tested fiber-reinforced panels. The load-displacement curves in terms of the vertical displacement at the point of load application for the plain concrete specimens are shown in Fig. 1.26.

1.2.4 Summary of the experimental methods

Simple mode I fracture experiments are an effective method of determining the fracture properties of concrete. The notched prism test method, the simplest in specimen geometry, allows one to directly measure the material properties. However, gripping the specimen with the test fixture becomes a challenge. Typically, end caps are glued to the specimen, which must be carefully se-

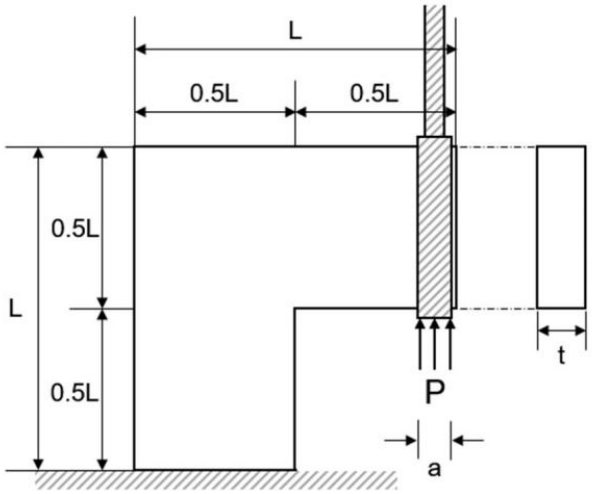

Figure 1.25: Geometry and loading conditions for the L shaped panel test [33]. The dimensions tested were $L = 500$ mm, $t = 100$ mm and $a = 40$ mm.

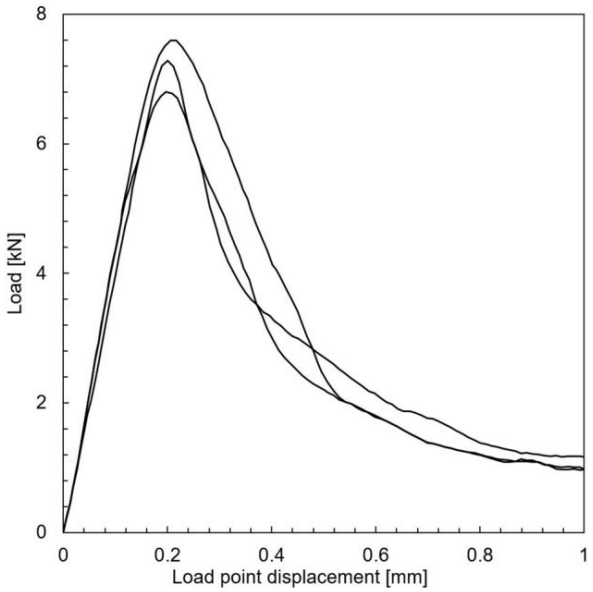

Figure 1.26: Load-displacement curves for three L shaped panel plain concrete tests with the same preparation, properties, and loading from Winkler [33] showing the typical concrete response.

lected to prevent adhesive failure, and the experimental data may need correction to account for the adhesive's effects. The gripping of the end platens can also produce unwanted rotation reactions in the specimen, resulting in unwanted stresses. Also, nonuniformities can arise around the notch, which could adversely affect the data.

To avoid preparing a notch in a specimen, the unnotched cylinder test method and the dog bone specimen test method utilize parabolically and circularly varying midsections, respectively, as the fracture zone. These allow *a priori* knowledge of the location of crack initiation without the nonuniform stresses that can arise around a notch. The issues with gripping the specimen in the test fixture, however, still remain. The specimen geometries are also more complex compared with the notched prism test method.

The modified compact tension test method shares many advantages and disadvantages with the notched prism test method; it retains a simple specimen geometry with a notch and adhesives for gripping with the test fixture. Rather than using end caps, however, the modified compact tension test method uses steel rods glued to the inside of the specimen, which can be easier to affix to a variety of test machines, but the adhesive effects must still be accounted for. Rotation effects must also be accounted for, unless measures (such as rotating eye nuts) are incorporated at the grips to eliminate the unwanted rotation reactions.

Indirect tensile test methods overcome the limitations of the direct tensile test, which are related to the load eccentricity, unwanted rotation reactions of the end platens, and adhesive bonding at the grip sections. The Brazilian disc test method, for example, eliminates gripping issues by utilizing a compressive load along the radial direction of a disc-shaped specimen. This offers simple specimen geometry with no adhesives needed, but the material properties cannot be directly measured and must be derived from the measured data. This test method can also be extended to CCNBD test method, which uses a chevron notch to test both mode I and mode II fracture.

The TPBT method has the advantage of the easy experimental setup and free of gripping issues, but the frictional force at the support and compressive stresses in the fracture zone are the main drawbacks of the method. The FPBT method is a similar experimental method to the TPBT

method, but the FPBT method uses two inner loading pins to give a constant bending moment. The wide range of zero shear force zone between the two inner pins ensures a stable stress state at the tip of a notch. Since the loading parts have two pins, the experimental setup becomes more complicated compared to the TPBT.

Because mixed-mode fracture is the most common fracture mode encountered by concrete structures, several mixed-mode experimental methods have been developed. The modified TPBT method is identical to the standard TPBT method, but the extended, angled notch provides the shear stresses for mixed-mode fracture. This means that all the advantages and disadvantages from the standard TPBT method are retained. The modified FPBT method, while rataining many of the advantages and disadvantages of the modified TPBT method, is more complex than the modified TPBT method, with two notches needed in the specimen and more loading points.

The L shaped panel test method provides a known origin point of crack propagation without the use of a notch. However, the nonstandard specimen geometry and the complex test setup make it a difficult test to perform. Similar to the notched prism test method, gripping issues are present, with adhesives needed for attachment to the test fixture and the possibility of unwanted rotation reactions needing correction.

1.3 Numerical methods for describing quasi-brittle material fracture

In this Section, a review of the prevailing theoretical and computational works which deal with modeling fracture in plain concrete is presented.

Before embarking on the review of the prevailing theoretical and computational works, a brief description of the physical process for governing fracture in concrete is presented since it is central to the development of the aforementioned modeling tools: the structural characteristic of concrete, which is the mixture of cement and aggregates, bring two main features in modeling of fracture process of concrete. The strain-softening and diffuse crack pattern of FPZ arise from the formulation, evolution, and coalescence of microcracks in concrete. These features are related to the regularization method to address the damage propagation in quasi-brittle material like concrete. The various experiments already showed the softening behavior of concrete in the post-peak region [35]. The

heterogeneity and brittleness of material characteristics cause progressively distributed damage, such as dispersed microcracks and void formation, which make this particular fracture behavior of concrete [36]. Hillerborg *et al.* [37] proposed the cohesive crack model for concrete describing the gradual softening of stress due to the increasing displacement of crack opening. The model assumed the remaining ligaments of the formulated crack would transfer the stress until the opening displacement reach the critical opening displacement. The monotonic decreasing function was used to express the softening behavior, where the critical opening displacement was decided from the consideration of energy balance.

The diffuse characteristic of the FPZ in concrete was seen in the image obtained from the x-ray investigation [38], which indicated the formation of a microcrack zone near the notch tip with increasing loading condition. The densely distributed microcracks in the FPZ were captured with the acoustic emission technique, where 95% of the acoustic energy emission originated from the FPZ [38]. The diffuse characteristic of the FPZ can be addressed with the nonlocal regularization method since the method has the characteristic length scale in the formulation. The concept of the nonlocal method, which considers the interaction among the elements inside of the nonlocal zone, is suitable to model the effect of generated microcracks on the FPZ [39]. Bažant *et al.* [40] used a nonlocal regularization method with the smeared cracking model to improve the limitations of the local model, such as spurious mesh sensitivity and directional bias of the mesh. The damage variable for the strain softening was defined as a function of nonlocal strain, which was the spatial averaging of the positive part of maximum principal strain. The Gaussian distribution function was used as a weight function of the nonlocal integral formulation. Jirásek [41] incorporated the integral based nonlocal formulation into a continuum damage mechanics model to predict the damage propagation in concrete. The weighted spatial average of the equivalent strain was used as a driving force of the damage evolution. The physical interpretation related the maximum aggregate size to the internal length scale, where the 2.7 times of maximum aggregate size was recommended to use as a length scale of the nonlocal averaging method [42]. Giry *et al.* [43] proposed the stress-based nonlocal integral method which had a nonsymmetric integral domain at

the vicinity of the boundaries. The weight function of the nonlocal formulation was dependent on the direction and intensity of the principal stresses of the neighboring points.

The implicit gradient enhancement method is also considered as a nonlocal regularization method, where the nonlocal strain is obtained from the Helmholtz equation. The expanded equivalent local strain through the Taylor series is incorporated into the integral type of nonlocal formulation to derive the differential equation of the nonlocal strain, which contains the nonlocal length scale parameter [44]. The homogeneous Neumann type boundary condition was introduced to ensure that the average of nonlocal strain over the entire domain would be the same with the average of the damage-equivalent local strain [45]. The two governing equations, which are the momentum equation and the Helmholtz equation with nonlocal strain, are solved simultaneously by a coupled numerical scheme. Zreid *et al.* [46] used an implicit gradient enhancement to regularize their implementation of a microplane damage-based model. The modified form of von Mises equivalent strain incorporating the volumetric and deviatoric parts of microplane strain was used as an equivalent strain term in Helmholtz equation [47]. Poh *et al.* [48] used over-nonlocal gradient enhancement as the regularization method for the plastic-damage model to represent damage evolution in concrete. The internal damage parameter was incorporated into the integral formulation, which lead to the gradient enhancement equation for the nonlocal internal damage parameter. The effective internal parameter was defined as the weighted sum of the local and nonlocal internal damage parameters, which was introduced in the damage parameter expression. The damage parameter reduced the nominal stress according to the evolving damage in concrete.

The aforementioned studies presented various models of the strain-softening at FPZ to describe the response of the concrete under the evolving damage. The evolution of damage is controlled by the damage variable incorporated in the governing equations, which reduces the stiffness of concrete.

The subsequent sections review the various damage models for concrete fracture, from the traditional continuum-based approach to the discrete model of extended finite element method.

1.3.1 Crack band model

The crack band theory was introduced to address the gradual strain-softening in a heterogeneous material due to the formation of microcracking in mode I fracture [27]. The aggregate size considered in the theory was not relatively small compared to the structural dimension. The FPZ at the crack tip, also called as a crack band, was modeled as a densely distributed band of parallel microcracks having a blunt front. The finite elements with smeared crack were used to express the damaged material, instead of using discrete crack appearance as shown in line crack model [49]. The fracture strain ε_f was introduced to express an additional strain due to the opening of the microcracks. The fracture strain was defined as an average deformation due to microcracking divided by the crack band width w_c, where it incorporated the characteristic length of concrete into the damage concept. Without considering the rate effects, the fracture strain was defined as a monotonically decreasing function depending on the stress term in the loading direction, which is shown in Eq. (1.2)

$$\varepsilon_f = \frac{1}{C_f}(f_t - \sigma_3) \tag{1.2}$$

where C_f is the slope of the monotonic decreasing function; and f_t is the tensile strength. The parameters for the strain-softening behavior were defined with the material parameters from experiments. The definition of C_f and the critical strain ε_0 are shown in Eq. (1.3). The critical strain represents the point where the stress in the loading direction vanishes to zero. The fracture energy G_f is incorporated in the equation, which represents the energy consumed in opening the microcracks per unit area of plane.

$$C_f = \frac{f_t w_c}{2G_f},\ \varepsilon_0 = \frac{f_t}{C_f} \tag{1.3}$$

The formulated constitutive behavior under the softening range with principal stresses $\sigma_1, \sigma_2, \sigma_3$ and principal strains $\varepsilon_1, \varepsilon_2, \varepsilon_3$ is shown in Eq. (1.4)

$$\begin{Bmatrix} \varepsilon_1 \\ \varepsilon_2 \\ \varepsilon_3 \end{Bmatrix} = \begin{bmatrix} 1/E & -v/E & -v/E \\ -v/E & 1/E & -v/E \\ -v/E & -v/E & 1/(Ec_p) \end{bmatrix} \begin{Bmatrix} \sigma_1 \\ \sigma_2 \\ \sigma_3 \end{Bmatrix} \tag{1.4}$$

where E is the Young's modulus; v is the Poisson ratio; and c_p is the cracking parameter. The equation for the cracking parameter is shown in Eq. (1.5) and it varies within the range of $0 < c_p < 1$. The parameter $E_t = EC_f/(C_f - E)$ is the tangent softening modulus which represents the modulus of strain-softening region.

$$c_p = \frac{-E_t(\varepsilon_0 - \varepsilon_3)}{E\varepsilon_3} \tag{1.5}$$

The principal stress σ_3 along the loading direction decreased monotonically as the fracture strain increase, and it vanished when the fracture strain reached the critical strain. The effect of fracture strain was incorporated into the compliance matrix as a cracking parameter to address the stiffness reduction due to the evolving damage. It should also be noted that the original version of the crack band model has been augmented to include a microplane model (more on this shortly) description in order to simulate shear cracks in concrete [50].

In a crack band model, the width of the damage band is dependent on the chosen element size. Therefore, results from simulations using the crack band model will be mesh-dependent [51]. However, for computational purposes, the width of the element-wide band may be adjusted if the strain-softening modulus is adjusted so as to preserve the same fracture energy, and such a study has been conducted by Bazant and Oh [27].

1.3.2 Microplane model

In the microplane models of Bažant *et al.* [50] which are *specific* to modeling the deformation response of concrete, each microplane represents the contact surface (or plane of separation)

between neighboring particles in concrete [see Fig. 1.27(a)]. The response of a element is then obtained from orientation averaging of a large number of spring-dashpot models with a limiting boundary (see Fig. 1.27b). These individual springs and dashpots are referred to as microplanes by Bazant and co-workers.

With ε_{ij} being the macroscopic strain tensor, the normal strain ε_N in the microplane model (see Fig. 1.28) is calculated as

$$\varepsilon_N = n_i n_j \varepsilon_{ij} \tag{1.6}$$

where $n_i (i = 1, 2, 3)$ is the Cartesian coordinates components of unit normal vector $\boldsymbol{n}$ of the microplane, is split into a volumetric portion $\boldsymbol{\varepsilon}_V$ (which is the same for all microplanes) and a "deviatoric" portion $\boldsymbol{\varepsilon}_D$ by

$$\varepsilon_V = \varepsilon_{kk}/3\,, \quad \varepsilon_D = \varepsilon_N - \varepsilon_V \tag{1.7}$$

where the repeated indices represent summation over $i = 1, 2, 3$. Furthermore. the two resolved shear strain components ε_M and ε_L on the microplane (see Fig. 1.28) are defined as

$$\varepsilon_M = m_i n_j \varepsilon_{ij}\,, \quad \varepsilon_L = l_i n_j \varepsilon_{ij} \tag{1.8}$$

where $m_i (i = 1, 2, 3)$ and $l_i (i = 1, 2, 3)$ are the Cartesian coordinates components of unit vectors orthogonal to the normal vector on the microplane, and $\mathbf{l} = \mathbf{m} \times \mathbf{n}$.

Along the the use of the Hill-Mandel macrohomogeneity condition, the macroscopic stress components on the microplane, $\boldsymbol{\sigma}$ are obtained from the individual microplane responses averaged over a suitable number of microplanes (while using a kinematic constraint between the macroscopic and microscopic variables), that is,

$$\boldsymbol{\sigma} = \frac{3}{2\pi} \int_\Omega \mathbf{s}\, \mathrm{d}\Omega \tag{1.9}$$

where Ω is a surface of a unit hemisphere centered at the material point, and $2\pi/3$ its volume.

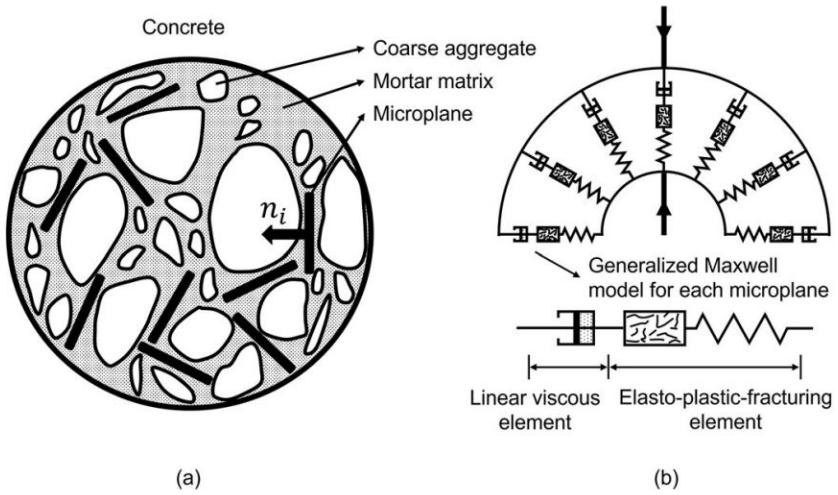

Figure 1.27: (a) System of discrete microplanes which are the contact surfaces (or plane of separations) between neighboring particles in concrete, and (b) microplane systems (for normal response) and generalized Maxwell model for each microplane. The figure is reused with permission from ASCE [52].

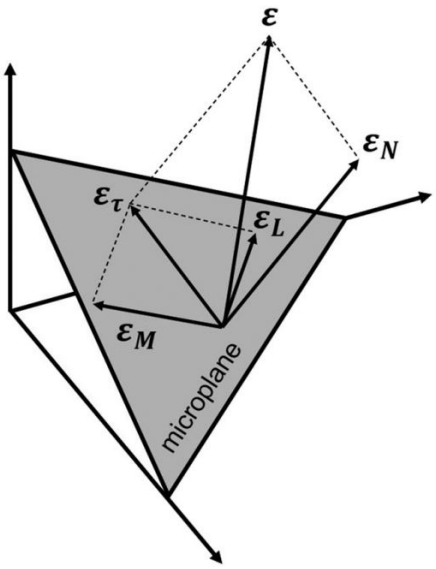

Figure 1.28: Decomposition of the total macroscopic strain tensor on the microplane. ε_τ represents the microplane shear strain component [53].

Furthermore, the tensor $\mathbf{s}$ is given by

$$\mathbf{s} = \sigma_N \mathbf{n} \otimes \mathbf{n} + \sigma_L \text{sym}\,(\mathbf{l} \otimes \mathbf{n}) + \sigma_M \text{sym}\,(\mathbf{m} \otimes \mathbf{n}) \tag{1.10}$$

with the constitutive response of the stress components σ_N, σ_L and σ_M on the microplane respectively given by

$$\sigma_N(t) = \mathcal{F}^t_{\tau=0}(\varepsilon_N(\tau), \varepsilon_T(\tau)), \tag{1.11}$$

$$\sigma_L(t) = \mathcal{G}^t_{\tau=0}(\varepsilon_N(\tau), \varepsilon_T(\tau)), \tag{1.12}$$

$$\sigma_M(t) = \mathcal{H}^t_{\tau=0}(\varepsilon_N(\tau), \varepsilon_T(\tau)) \tag{1.13}$$

where $\mathcal{F}$, $\mathcal{G}$ and $\mathcal{H}$ are functionals of the history of the microplane strains at time t, and $\varepsilon_T(\tau)$ is the shear strain resultant on the microplane with components ε_L and ε_M. It is important to note that the functionals $\mathcal{G}$ and $\mathcal{H}$ are the same except they give different projections on axes L and M, respectively.

The microplane model of Bazant is one of the most popular approaches to modeling concrete softening response, in particular, it has been widely used to simulate the response under complex loading conditions including heavy confinement where the peak and post-peak response are quite different. The stress response is obtained by orientation averaging over 37 microplanes at each material point to obtain a better accuracy for far post-peak response (see Fig. 1.27b). Furthermore, Caner and Bazant [54] point out that the Poisson's ratio has to be less than 0.25 which is reasonable for concrete. They continue to identify some of the challenges in meeting the 2nd Law of Thermodynamics and their approach to addressing this issue.

Finally, with regards to regularization in a microplane framework, Bazant and Di Luzio [55] introduces a *nonlocal* version of a quantity f, that is, $\bar{f}$ which is calculated as

$$\bar{f}(\mathbf{x}) = \frac{\int_{\mathcal{R}} \upsilon(\mathbf{x} - \mathbf{x}') f(\mathbf{x}')\, \mathrm{dV}}{\int_{\mathcal{R}} \upsilon(\mathbf{x} - \mathbf{x}')\, \mathrm{dV}} \tag{1.14}$$

where $f(\mathbf{x}')$ is the quantity f at point $\mathbf{x}'$, and dV is a volume element. The region $\mathcal{R}$ is a sphere of radius equal to an intrinsic material length scale with point $\mathbf{x}$ being the centroid of the sphere, and point $\mathbf{s}$ being a material point within region Ω. Finally, $\upsilon(\mathbf{x}-\mathbf{x}')$ represents a kernel function. The user is free to assign a physical meaning to quantity f *e.g.* strain, stress or even components of the microplane strain, *etc.*

1.3.3 Continuum damage mechanics

The damage model based on the continuum mechanics explains the fracture of materials without introducing the complex description of microscopic damage initiation and evolution to the formulation. The heterogeneity of the damaged material, which is derived from the formulation of microcracks in the material, is homogenized with the damage variable in the continuum domain, where the damage variable introduced in the free energy formulation expresses the macroscopic evolution of damage. The stiffness of this element is continuously degrading as the damage variable evolves [56]. The damage variable can have different forms, such as scalar, vector or tensorial form. The scalar damage variable is used to address the formulation of randomly distributed microcracks in isotropic materials [57]. The vectorial or tensorial form of damage variable is used to represent the oriented microcracks, which can be the sources of anisotropic damage evolution [58]. The different expression of damage variable in opening and closing cracks of concrete was also studied, where the splitting of free energy into tension and compression part was made to study the unilateral effects of quasi-brittle material [59].

Richard *et al.* [60] proposed a continuum damage mechanics model which used a scalar damage variable to express the nonlinearities due to micro-cracking in concrete. The constitutive equations assumed two independent behaviors of the cracked surface, where the hydrostatic strain part of the state potential affected the cracks opening and closing and the deviatoric part of the strain and stress tensors were related to the frictional sliding. The strain energy was decomposed into two parts, which were spherical and deviatoric parts, to realize the constitutive assumptions. The state

potential equation related to the damage is shown in Eq. (1.15)

$$\rho\Psi_{damage} = \frac{\kappa}{6}\left((1-\zeta)\left\langle\varepsilon_{kk}\right\rangle_{+}^{2} - \left\langle-\varepsilon_{kk}\right\rangle_{+}^{2}\right) + (1-\zeta)\mu\varepsilon_{ij}^{D}\varepsilon_{ij}^{D} \tag{1.15}$$

where ρ is the mass density; Ψ_{damage} is the damaged state potential; κ and μ are the bulk and shear modulus; ζ is the scalar damage variable; ε_{ij} is the total strain tensor; and $\varepsilon_{ij}^{D} = \varepsilon_{ij} - (1/3)\varepsilon_{kk}\delta_{ij}$ is the deviatoric part of strain tensor, where δ_{ij} is the second order Kronecker tensor. The hydrostatic strain part was decomposed into positive and negative parts to model the stiffness recovery in the crack closure, where $\left\langle\varepsilon_{kk}\right\rangle_{+}$ represents the positive part of ε_{kk}. Even though the damage variable was introduced in both of the spherical and deviatoric part of the energy, the damage at compression only acts on the deviatoric energy part due to the introduced crack closure model. The effect of the sliding at the crack lips was considered in the total state potential with the additional term related to the damage variable and deviatoric component of free energy. The kinematic and isotropic hardening due to friction was also addressed in the state potential. The state equations were derived based on the Clausius–Duhem inequality [61] to assure thermodynamic admissibility. The threshold surface, where the positive value indicated the activation of damage, was defined with the damage energy released rate and thermodynamic force of isotropic hardening. The surface without the threshold managed the sliding mechanism which related to the thermodynamic force of the kinematic hardening. For the numerical implementation, the explicit form of damage variable was calculated following the calculation of Cauchy stress and friction stress tensor. The integral form of the nonlocal regularization method was used to avoid the strain localization, where the nonlocal damage threshold surface was defined with the nonlocal damage energy release rate. The proposed method was used to solve structural application problems, such as a direction tension test [62] and a notched concrete beam bending test [63]. The simulation results followed the experimental trend of the load-displacement curve, while the diffuse crack propagation path was observed from the nonlocal regularization. The comparison between simulation results and experimental data is shown in Fig. 1.19.

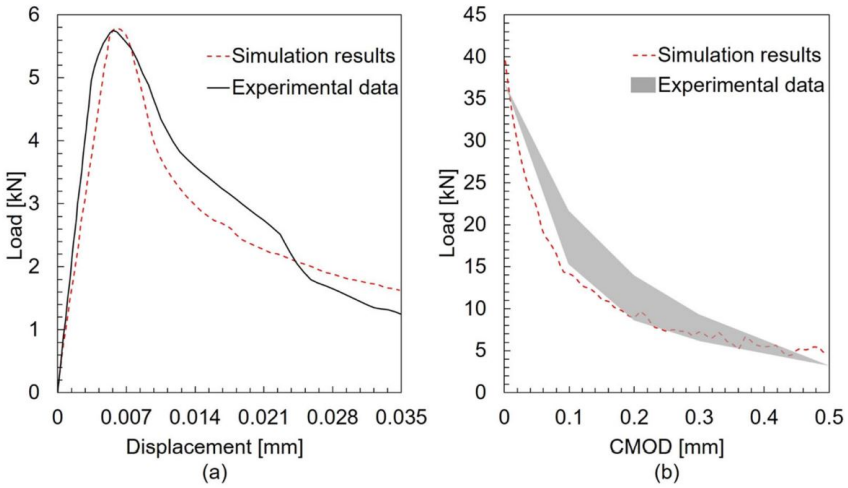

Figure 1.29: Load-displacement curves: (a) direct tension test and (b) single edge notched beam bending test [60].

Brünig *et al.* [64] formulated an anisotropic damage model in a continuum approach, where the formulation followed the second law of thermodynamics. The different values of the parameters in damage criteria were used depending on the stress state. The strain tensor was decomposed into elastic ε^{el} and inelastic part ε^{da}, followed by the kinematic concept suggested in previous work of modeling the damage behavior of ductile metals [65]. The decomposed strain tensor was used in the definition of specific mechanical work and the specific Helmholtz free energy ψ. The elastic part of the free energy was defined as a quadratic function of the elastic strain tensor and the decrease of energy due to damage was incorporated by the linear function of the damage strain tensor. The material parameters determined from the experimental data were included in the energy definition, where the parameters described the degradation of elastic properties due to the evolving damage. Two parameters were related to the isotropic growth in damage and the other two parameters represented the anisotropic damage evolution. The specific Helmholtz free energy also incorporated an additional internal mechanical state variable φ representing an equivalent damage strain measure. From the consideration of the second law of thermodynamics, the governing state

equation is derived as shown in Eq. (1.16)

$$\boldsymbol{\sigma} \cdot \dot{\boldsymbol{\varepsilon}}^{el} + \boldsymbol{\sigma} \cdot \dot{\boldsymbol{\varepsilon}}^{da} - \left(\rho \frac{\partial \psi^{el}}{\partial \boldsymbol{\varepsilon}^{el}} \cdot \dot{\boldsymbol{\varepsilon}}^{el} + \rho \frac{\partial \psi^{el}}{\partial \boldsymbol{\varepsilon}^{da}} \cdot \dot{\boldsymbol{\varepsilon}}^{da} + \rho \frac{\partial \psi^{da}}{\partial \varphi} \dot{\varphi} \right) \geq 0 \tag{1.16}$$

where $\boldsymbol{\sigma}$ is the stress tensor; ψ^{el} is the elastic part of the free energy; ψ^{da} is the damage part of the free energy; and ρ is the mass density. The governing state equation was reduced in the Kelvin inequality, which is shown in equation Eq. (1.17), with the consideration of the non-dissipative process of the reversible deformation. The thermic state equation governing the reversible deformation is shown in Eq. (1.18).

$$\boldsymbol{\sigma} \cdot \dot{\boldsymbol{\varepsilon}}^{da} - \rho \frac{\partial \psi^{el}}{\partial \boldsymbol{\varepsilon}^{da}} \cdot \dot{\boldsymbol{\varepsilon}}^{da} - \rho \frac{\partial \psi^{da}}{\partial \varphi} \dot{\varphi} \geq 0 \tag{1.17}$$

$$\boldsymbol{\sigma} = \rho \frac{\partial \psi^{el}}{\partial \boldsymbol{\varepsilon}^{el}} \tag{1.18}$$

The evolution of damage was governed by a damage surface, where the concept was similar to the yield surface in plasticity theory. The function of stress tensor and equivalent stress measure, which was a damage threshold, was used as a damage surface function representing the criteria of the damage initiation and evolution [66]. The damage strain rate was defined with the stress invariants and kinematic damage parameters depending on the stress state. The stress state was defined based on the stress triaxiality, which was the ratio of the mean stress and von Mises equivalent stress, and the Lode parameter, which was a function of principal stress components. The proposed damage model was calibrated with the experimental data [67] and the stress-strain curves from the simulation results were validated with the experimental curves in various stress states.

With regards to the traditional continuum damage mechanics-based model discussed above, there are some following issues which are important: (1) modeling of crack closure within a continuum damage mechanics framework and its numerical implementation is not straightforward even for isotropic materials [68]; and (2) a traditional continuum damage mechanics-based model like the one discussed above does not contain an intrinsic material length scale (it is a local model),

and will therefore exhibit mesh sensitivity in their application into a computing framework. With regards to regularization, in a continuum damage mechanics framework, regularization can be handled in a nonlocal framework (for example, using Eq. (1.14) as pursued in [69] and [70]) or a gradient-type approach as done in a phase field framework.

1.3.4 Phase field model

This model introduces an additional field variable, which is called a phase field, that is used to formulate a free energy of the material. The free energy functional includes both the phase field itself as well as its gradient (which is used for regularization). The mechanical equilibrium of the system is obtained by minimizing the energy functional with respect to the displacements. The evolution of the phase field is related to the Volterra derivative of the energy functional with respect to the phase field variable ζ [71]. The phase field itself is used to represent the damage zone similar to continuum damage models. The gradient of the phase field introduces a length scale. This length scale causes a regularization or diffusive factor [72].

The application of phase field models to simulate quasi-brittle fracture was introduced recently, in static [73] and dynamic [74] cases. Miehe *et al.* [72] presented a finite element method where the phase field parameter is treated as a nodal variable.

The general phase-field equations can be derived as follows: with ψ being the free energy density and the global stored energy functional Ψ given by

$$\Psi = \int_{\mathcal{R}} \psi(\mathbf{u}, \nabla\mathbf{u}, \zeta, \nabla\zeta)\,\mathrm{dV} \tag{1.19}$$

where $\mathbf{u}$ is the displacement vector and ζ being the phase-field or damage variable with $0 \leq \zeta \leq 1$, it can be expressed

$$\frac{\delta\Psi}{\delta\mathbf{u}} = \mathbf{b} \tag{1.20}$$

$$\frac{\delta\Psi}{\delta\zeta} + \frac{\delta\Phi}{\delta\dot{\zeta}} = 0 \tag{1.21}$$

where δ is the Volterra derivative, $\mathbf{b}$ the body force vector and $\Phi \geq 0$ the dissipation potential.

Eq. (1.20) represents the equilibrium equation whereas Eq. (1.21) represents the evolution equation for the phase-field variable ζ. It is important to note that a phase-field value $\zeta = 0$ represents an undamaged material whereas a phase-field value of $\zeta = 1$ represents a fully-damaged material.

For the derivation of the specific phase-field governing equations, there are generally two ways to proceed from this point: (1) In the work of Miehe *et al.* [72] and Wu [75], the free energy density $\psi = \hat{\psi}(\nabla \mathbf{u}, \zeta)$ and the dissipation potential $\Phi = \hat{\Phi}(\zeta, \nabla\zeta, \dot{\zeta}, \nabla\dot{\zeta})$, and (2) in the work of Narayan and Anand [76], the free energy density $\psi = \hat{\psi}(\nabla \mathbf{u}, \zeta, \nabla\zeta)$ and the dissipation potential $\Phi = \hat{\Phi}(\dot{\zeta})$, and this method stays more true to traditional phase-field approaches. However, in both approaches, the intrinsic material length scale which tracks crack propagation is introduced through the $\nabla\zeta$ term.

As an example, from the work of Narayan and Anand [76], the regularization of a sharp crack in the calculations is provided by the intrinsic material length scale, r_ϕ which appears with the $\nabla\zeta$ term in the free energy density ψ, and it is calculated by

$$r_\phi = \Gamma/\psi_* \tag{1.22}$$

where the positive-valued material constant Γ is the energy dissipated per unit area of crack extension (determined from experiments), and ψ_* is a positive-valued fit parameter with units of energy per unit volume. Hence, the internal material length scale r_ϕ in the phase-field model is a numerical parameter. A possible way to provide a physical meaning to the parameter r_ϕ is to link it to the size of the FPZ.

This chapter will be concentrated on the phase-field-type models of Miehe *et al.* [72] and Wu [75]. In these models, a crack surface density function $\gamma(\zeta, \nabla\zeta)$ has to be specified. The expression for the crack surface density function is given by [75]:

$$\begin{aligned} \gamma(\zeta, \nabla\zeta) =& \frac{1}{c_0}\left(\frac{1}{r_\phi}\alpha_{cr}(\zeta) + r_\phi \left|\nabla\zeta\right|^2\right), \\ & c_0 = 4\int_0^1 \sqrt{\alpha_{cr}(\beta)}\,\mathrm{d}\beta \end{aligned} \tag{1.23}$$

where $\alpha_{cr}(\zeta) = \xi^*\zeta + (1-\xi^*)\zeta^2$ is the crack geometric function, and the parameter ξ^* is used to describe the diffuse pattern of the crack.

Following this, Wu [75] defines the global dissipation functional as

$$\Phi = \int_{\mathcal{R}} \left[G_f \dot{\gamma}(\dot{\zeta}, \nabla\dot{\zeta}; \zeta, \nabla\zeta) + \frac{1}{2}\eta^* \dot{\zeta}^2 \right] \mathrm{dV} \tag{1.24}$$

where G_f is the fracture energy, and η^* is the viscosity coefficient to describe the rate-dependent damage process.

Finally, the global stored energy functional and degradation function from Wu [75] respectively appears in Eq. (1.25) and Eq. (1.26) as

$$\Psi = \int_{\mathcal{R}} \psi(\boldsymbol{\varepsilon}, \zeta)\, \mathrm{dV} = \int_{\mathcal{R}} g(\zeta)\psi_0(\boldsymbol{\varepsilon})\, \mathrm{dV} \tag{1.25}$$

$$g(\zeta) = \frac{(1-\zeta)^p}{(1-\zeta)^p + a_1\zeta(1 + a_2\zeta(1 + a_3\zeta))} \tag{1.26}$$

where $\psi_0(\boldsymbol{\varepsilon})$ is the undamaged free energy density. The parameter a_1 is related to the internal length scale, and the parameters a_2, a_3 are determined from the material properties and calibrated based on the targeted softening law. The governing equilibrium and phase-field equations are then derived using Eqs. (1.20) and (1.21). Although Wu [75] suggests a relation described in Remark 2.4 in their work to address crack closure, they did not model crack closure in their simulations.

Remark: Another popular method pursued in the phase-field literature to address crack closure is the route adapted by Miehe *et al.* [72] where they split the free energy functional into “positive" (or tensile) and “negative" (or compressive) parts. The decomposition of the free energy into a positive part due to tension and a negative part due to compression was achieved with the spectral decomposition of the strain tensor. The definition of the tension and compression part of the free energy is shown in Eq. (1.27):

$$\psi_0^{\pm}(\boldsymbol{\varepsilon}) := \lambda_e \langle \varepsilon_1 + \varepsilon_2 + \varepsilon_3 \rangle_{\pm}^2 / 2 + \mu_e \left(\langle \varepsilon_1 \rangle_{\pm}^2 + \langle \varepsilon_2 \rangle_{\pm}^2 + \langle \varepsilon_3 \rangle_{\pm}^2 \right) \tag{1.27}$$

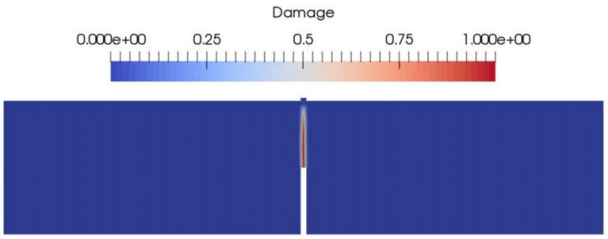

Figure 1.30: Damage contours in a three-point bending sample. The damage started from the notch tip and propagated toward the top surface. The internal length scale used for the simulation was $r_\phi = 2.5\ \mathrm{mm}$ [75].

The $\{\varepsilon_i\}_{i=1,2,3}$ are the principal strains, which are based on the strain tensor $\boldsymbol{\varepsilon}$. Two different ramp functions are used($\langle x\rangle_+ := [|x| + x]/2$, $\langle x\rangle_- := [|x| - x]/2$) to decompose the energy expression. The λ_e and μ_e are the elastic constants. With the decomposed energy, the free energy density was defined with a degradation function as shown in Eq. (1.28)

$$\psi(\boldsymbol{\varepsilon}, \zeta) = [g(\zeta) + k]\,\psi_0^+(\boldsymbol{\varepsilon}) + \psi_0^-(\boldsymbol{\varepsilon}) \tag{1.28}$$

where $g(\zeta) = (1-\zeta)^2$ is a degradation function; and k is a small positive number to ensure the well-posed numerical discretization method when the damage variable converges to $\zeta = 1$. The degradation function was only applied to the positive part of stored energy to model crack closure effects.

With regards to modeling concrete fracture using the phase field method of Wu [75], validation of their proposed method was conducted with respect to several boundary value problems, and one such result is shown in this paper, that is, the symmetric three-point bending simulation. The cracking (or damage) contour in the three-point bending sample is shown in Fig. 1.30 whereas the simulated force-displacement response from this simulation is plotted with respect to experimental data (the experimental results are bounded by the solid lines) in Fig. 1.31. The internal length scale used in the simulation was$r_\phi = 2.5\ \mathrm{mm}$. From these results, it can be seen that the phase-field method is able to simulate the output of this experiment to good accord.

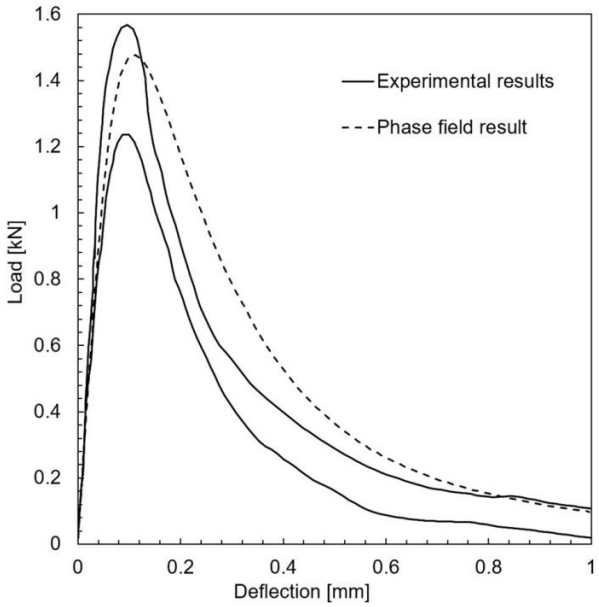

Figure 1.31: Load-deflection curve of the three-point bending test with the notched concrete beam specimen [75]. The parameters in the model were picked to match the experimental data to the extend possible.

1.3.5 Peridynamics model

The peridynamics model was introduced to overcome the limitation of the continuum mechanics viewpoint of damage, where the relative displacement and force formulation based on the partial derivatives in spatial coordinates could not be defined along the discontinuities [77]. The model uses integration to compute the force of the material point, rather than using differentiation. The special techniques, such as the redefinition of the domain near the cracked region, are not needed with this model since the integral based equations are still valid at the region of discontinuities. The nonlocality of the model is naturally introduced with the concept of the horizon, where the particles interact with each other. The equation of motion of peridynamics is shown in Eq. (1.29)

$$\begin{aligned} \rho\ddot{\mathbf{u}}(\mathbf{x},t) = &\int_R \boldsymbol{f}(\mathbf{u}(\mathbf{x}',t)-\mathbf{u}(\mathbf{x},t),\mathbf{x}'-\mathbf{x})\,\mathrm{dV} \\ &+\mathbf{b} \end{aligned} \tag{1.29}$$

where $\mathbf{u}(\mathbf{x}, \mathbf{t})$ is the displacement field at any point $\mathbf{x}$ in the reference configuration at time t; $\mathbf{b}$ is the body force density; ρ is the mass density and $\boldsymbol{f}$ is the pairwise force function. The pairwise force function is related to the constitutive behavior of the material, where it describes how the deformation affects the internal forces of the material. The fracture of the material is introduced with the concept of bond elongation. If the stretch between the two points exceeds the predefined limit, the bond is considered to be broken and the bond force becomes zero. While the peridynamic model has been successfully applied to the brittle fracture of solids [78], the progress is still needs to be made for the quasi-brittle fracture in concrete like materials.

Ni *et al.* [79] used the irregular distribution of material points generated from finite element mesh to simulate the quasi-brittle fracture of concrete-like material with peridynamic method. The integral expression of the equation of motion followed by the work from Silling *et al.* [78] with bond-based peridynamic model. The pairwise force function was defined by considering the effect of the bond-breakage and stretch of the bond. The proposed force function is shown in Eq. (1.30)

$$\boldsymbol{f}(\boldsymbol{\eta}, \boldsymbol{\xi}, t) = c\varrho(\boldsymbol{\eta}, \boldsymbol{\xi}, t) \left(\frac{\|\boldsymbol{\eta} + \boldsymbol{\xi}\| - \|\boldsymbol{\xi}\|}{\boldsymbol{\xi}} \right) \left(\frac{\boldsymbol{\eta} + \boldsymbol{\xi}}{\|\boldsymbol{\eta} + \boldsymbol{\xi}\|} \right) \tag{1.30}$$

where $\boldsymbol{\eta} = \mathbf{u}(\mathbf{x}', t) - \mathbf{u}(\mathbf{x}, t)$ is a relative displacement vector between two points $\mathbf{x}$ and $\mathbf{x}'$; $\boldsymbol{\xi} = \mathbf{x}' - \mathbf{x}$ is the relative position vector of two points; and $\|\boldsymbol{\xi}\|$ and $\|\boldsymbol{\eta} + \boldsymbol{\xi}\|$ are the norms of $\boldsymbol{\xi}$ and $\boldsymbol{\eta} + \boldsymbol{\xi}$. The parameter c is describing the local resistance of the bond stretch, where it assumed to be uniform in the peridynamics horizon, r_ϕ.

In the peridynamics approach, the horizon r_ϕ serves as the intrinsic length scale in the model, and therefore provides the regularization in the calculations. Visually, the horizon of material point x is depicted as the white circle surrounding the material point x, and r_ϕ is measured from material point x to the point on the circumference of the white circle. For this approach, the properties (bond force, driving force for fracture *etc.*) at material point x depends on its neighboring material points within the horizon. The description of the method to obtain the value of r_ϕ will be following shortly.

Looking at the specific case of plain stress, the parameter c is expressed as

$$c(\boldsymbol{\xi}, r_\phi) = \begin{cases} \frac{315E}{8\pi d {r_\phi}^3} \left[1 - \left(\frac{\|\boldsymbol{\xi}\|}{r_\phi}\right)^2\right]^2, & \text{when } \|\boldsymbol{\xi}\| \leq r_\phi \\ 0, & \text{when } \|\boldsymbol{\xi}\| > r_\phi \end{cases} \tag{1.31}$$

where d is the thickness of planar structure, and E is Young's modulus. The local characteristic function ϱ was applied to indicate whether the bond breakage had occurred between two points. The expression of this function is shown in the Eq. (1.32)

$$\varrho(\boldsymbol{\eta}, \boldsymbol{\xi}, t) = \begin{cases} 1, & s \leq s_0 \\ 0, & s > s_0 \end{cases} \tag{1.32}$$

where s_0 is the predefined critical stretch value. If the stretch s exceeds the critical value, then the bond breakage has occurred and the bond is considered to have no interaction. The critical stretch value was defined using the macroscopic fracture energy G_f where the expression is shown in the Eq. (1.33).

$$s_0 = \sqrt{\frac{5\pi d G_f}{8E r_\phi}} \tag{1.33}$$

Eq. (1.33) can be inverted to obtain the horizon length r_ϕ as

$$r_\phi = \frac{5\pi d G_f}{8E s_0^2} \tag{1.34}$$

Since G_o, E and s_0 are material-specific properties, and d is a geometric property, r_ϕ can be obtained by using Eq. (1.34).

In the numerical implementation, the material domain was discretized by the irregularly distributed quadrilateral elements and the barycentre of the elements were used as the material points for peridynamics calculation. The adaptive dynamic relaxation method was applied as the time integration scheme to simulate the quasi-static behavior of solids [80]. As for the numerical example, the brittle fracture under uniaxial tension in a plate with a circular hole was studied. The thickness

of the crack was more localized when the smaller value of the horizon size was used. The fracture simulation case with unilateral tension test upon a pre-cracked plate with an off-center circular hole showed a similar crack initiation and propagation trend compared to the results reported from Tabiei *et al.* [81].

Yang *et al.* [82] proposed the improved ordinary state-based peridynamics model which incorporated the cohesive crack growth for the fracture analysis of quasi-brittle materials. The state-based peridynamics model is different from the bond-based model, in the sense that the deformation of other bonds connected to the specific pair bond affects the interaction between two material points. The integral expression of Newton's second law in state-based peridynamics formulation followed the work from Silling *et al.* [83]. For describing the constitutive behavior of the linear elastic isotropic solids, the model from Madenci [84] was selected as the expression for the force density vectors. The damage initiation was explained with the bond stretch-based damage model, where it activated when the stretch of the bond exceeded the maximum tensile strain. The maximum tensile strain was defined as elastic modulus divided by the tensile strength. The influence of the damaged bond to the other bonds within the peridynamics horizon would gradually decrease as the damaged bond stretch increased. The bilinear softening curve was chosen to express the cohesive effect in the FPZ, which are shown in the Eq. (1.35) and Eq. (1.36)

$$\boldsymbol{f}(\boldsymbol{\xi},\boldsymbol{\eta}) = \left[\frac{s_c + (\gamma-1)s_0 - \gamma s}{s_c - s_0}(1-\beta) + \beta\right] f_{max}\frac{\boldsymbol{\xi}+\boldsymbol{\eta}}{|\boldsymbol{\xi}+\boldsymbol{\eta}|} \tag{1.35}$$

$$\boldsymbol{f}(\boldsymbol{\xi},\boldsymbol{\eta}) = \frac{\gamma(s_c - s)}{(\gamma-1)(s_c - s_0)}\beta f_{max}\frac{\boldsymbol{\xi}+\boldsymbol{\eta}}{|\boldsymbol{\xi}+\boldsymbol{\eta}|} \tag{1.36}$$

where $\boldsymbol{\xi}$ is the relative position vector; $\boldsymbol{\eta}$ is the relative displacement vector; s is the stretch in the bond; s_c is the final bond stretch; s_0 is the bond stretch at tensile strain; f_{max} is the pairwise force magnitude at bond stretch s_o; and $\beta = f_k/f_{max}$ and $\gamma = s_c - s_0/s_k - s_0$ are the shape factors. The Eq. (1.35) is valid in the range of $s_0 < s < s_k$ and Eq. (1.36) is valid for $s_k \leq s < s_c$. The information about the parameters s_k and f_k appear in Fig. 1.32, which shows the bilinear softening curve. The final bond stretch was defined based on the specific fracture energy G_F, where the

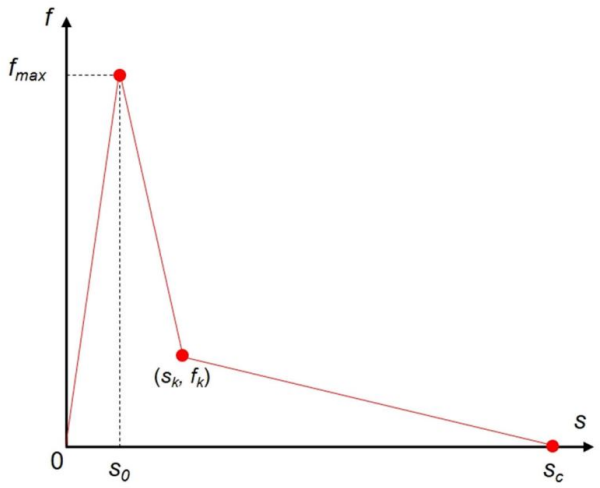

Figure 1.32: Bilinear softening degradation curve [82].

expressions for the two- and three-dimensional case is shown in the Eq. (1.37)

$$\begin{cases} s_c = \frac{3G_F\gamma}{hr_\phi{}^3 f_{max}||\boldsymbol{\xi}||(1+\gamma\beta)} + s_0 & \text{(2D case)} \\ s_c = \frac{8G_F\gamma}{\pi r_\phi{}^4 f_{max}||\boldsymbol{\xi}||(1+\gamma\beta)} + s_0 & \text{(3D case)} \end{cases} \tag{1.37}$$

where r_ϕ is the size of the horizon; h is the thickness; and w_d is the area under the degradation curve. For the numerical implementation of the governing equation, the dynamic relaxation method [85] was applied for quasi-static analysis. The validation of the proposed peridynamic model was conducted by comparing the numerical results with the experiment results in various numerical examples, including the three-point bending test [86], L-shaped panel test [34], and mixed-mode fracture in beam bending test [87]. The crack propagation path and load-displacement curve of the L-shaped panel test is shown in Fig. 1.33, where the experimental data of load-displacement curve is bounded by solid lines.

Cabral *et al.* [88] incorporated a bilinear law into the peridynamics model to calibrate the numerical models for the analysis of quasi-brittle fracture. The bilinear law applied in this work was based on the work from Hillerborg [89]. The bond-based peridynamics equation was used as the governing equation based on the work from Silling *et al.* [77]. The pairwise force function

was defined as a derivative of a micro-potential with respect to the relative displacement vector where the micro-potential represents an energy stored in an individual deformed bond. At the definition of the critical stretch value, the study used material toughness G_f as a reference value. The energy dissipated from the rupture of bonds in a control area should be equal to the toughness [78]. The specific fracture energy G_f of bonds were imposed with random values, where the values followed the Weibull extreme value distribution. Since the other parameters of the critical stretch were deterministic and the toughness distributed randomly, the critical stretch inherited the random distribution from the toughness G_f. Similar methods were proposed to realize the random nature of the material models, which considered the random orientation of grains [90]. For the numerical simulation, the study introduced numerical horizon $r_\phi{}'$, where it was different from the characteristic length of the material r_ϕ. The numerical horizon introduced the bilinear law to the bond by changing the definition of the critical stretch value. The modified expression of critical stretch s' and the numerical horizon $r_\phi{}'$ is shown in Eq. (1.38)

$$s' = \sqrt{\frac{RG_f}{Er_\phi{}'}}, \quad r_\phi{}' = \frac{r_\phi {s_0}^2}{s_p s_r} \tag{1.38}$$

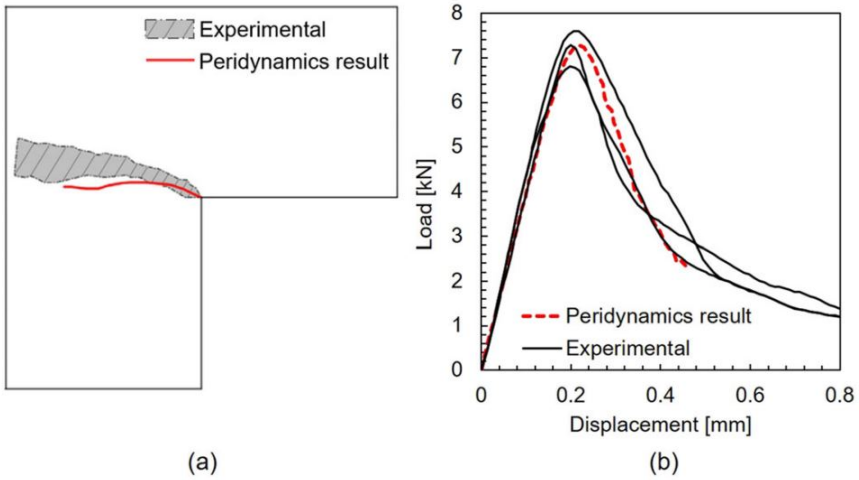

Figure 1.33: Comparison of numerical and experimental results of L-shaped panel test: (a) Crack propagation path (b) Load-displacement curve [82].

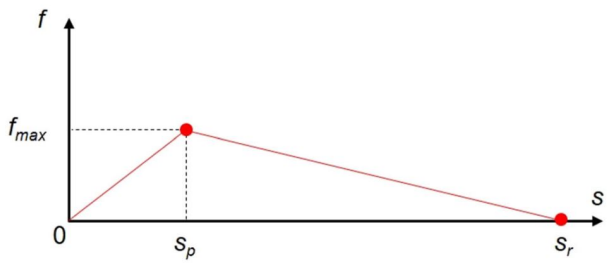

Figure 1.34: Bilinear constitutive law at the bond level [88].

where E is Young's modulus; R is the parameter depends on the dimension of the problem and Poisson's ratio; and s_p and s_r are the stretch parameters from the bilinear law shown in Fig. 1.34. The shape of the bilinear law is governed by the ratio of stretch parameters $K_r = s_r/s_p$ and the place of peak force was determined by the ratio of $(s_0/s_p)^2$. The parameter K_r was fitted with the experimental data. The numerical example was studied with the proposed method in the case of uniaxial tension test on sandstone bodies, where the validation of the results was conducted by comparing the results with the experimental results [91].

Wu *et al.* [92] used an intermediately homogenized peridynamics model, which was proposed by Chen *et al.* [93], to investigate the quasi-brittle fracture behavior of the concrete. An elastic stiffness of the bond for the pairwise force function was expressed with a two-dimensional conical micro-modulus in plane stress condition [94]. The model considered the mesoscopic heterogeneity nature of the concrete, where it composed of aggregates and cement mortar. The three types of the bond were defined, which were aggregate-aggregate bond, mortar-mortar bond, and aggregate-mortar bond. The first two bonds were for each of the phases and the last one was for the interface. The type of bond between two material points was decided based on the volume fraction of phases at the two endpoints. The volume fraction of each phase of the material was distributed uniformly in the simulation domain following the random distribution. The average material properties of aggregates and cement mortar were assigned to the interfacial bond. Since the fracture of concrete is controlled by the failure of mortar or the interface, the fracture criteria of the aggregate-aggregate bond used the fracture energy of the interfacial transition zone. The extra bond-failure criterion

proposed by Xu *et al.* [95] was used to remove the errors from the unbroken bonds bridging the crack. The validation of the proposed method was conducted by comparing the result from the anchor pull-out experiment on concrete [96]. Although the load-displacement curve from the proposed method showed fluctuations, the average trend of the curve followed the experimental result. The reason for fluctuations was explained by the large difference in the strain at the failure among the bonds.

The models described hitherto are based on refomulating constitutive models (such as the microplane model or the continuum damage model) or the governing equations (such as the phase field model or the peridynamics models). The next few models reformulate the computational implementation of fracture directly.

1.3.6 Extended finite element method

The extended finite element method (XFEM) aims to model problems containing singularities and discontinuities, which traditional interpolation are unable to do. These discontinuities can be cracks, grain boundaries, dislocations, or phase boundaries [97]. The process is performed by adding discontinuous functions to the traditional displacement field functions of FEM, a process commonly referred to as “enriching" the elements. Sets of elements containing the crack and crack tips are defined for the application of the discontinuous functions. An important advantage of this method is the ability to model the crack without remeshing the geometry to align the element edges with the discontinuity. The general equation for the XFEM crack displacement field is shown in Eq. (1.39)

$$\begin{aligned}\mathbf{u}(\mathbf{x}) = &\sum_{i\in I} N_i(\mathbf{x})\mathbf{u}_i + \sum_{i\in I_f} N_i(\mathbf{x}) J(f_{cr}(\mathbf{x}))\boldsymbol{q}_i^0 \\ &+ \sum_{i\in I_t} N_i(\mathbf{x}) \left(\sum_j \Lambda^{(j)}(\mathbf{x})\boldsymbol{q}_i^{(j)} \right)\end{aligned} \tag{1.39}$$

where the first term represents the elements of traditional FEM expression (set I), the second term represents the enriched elements at the crack face away from the tip (set I_f), and the third term represents the enriched elements at the crack tip (set I_t). Here $\mathbf{u}_i$ represents the displacement vector for element i, N_i represents the standard FEM shape functions for element i in each respective

element set, $\Lambda^{(j)}$ represents the set of j discontinuous enrichment functions applied to element i in set I_t, $\boldsymbol{q}_i^j$ represents the enrichment coefficients for element i in set I_t along with the set of j discontinuous enrichment functions, and $\boldsymbol{q}_i^0$ represents the enrichment coefficients for element i in set I_f. Finally, the function $J(f_{cr})$ is defined in Eq. (1.40)

$$J(f_{cr}) = \begin{cases} -1 & \text{if} \quad f_{cr} > 0 \\ +1 & \text{if} \quad f_{cr} < 0 \end{cases} \tag{1.40}$$

where function f_{cr} is a signed distance function to the crack such that sign determines which side of the crack the material point $\mathbf{x}$ is on.

Many developments have been made in recent years to apply XFEM to quasi-brittle materials like concrete. XFEM is very commonly combined with cohesive zone models for these materials. Moes *et al.* [98] performed this using a linear cohesive softening law. Cohesive zone modeling is described in more detail in the following section of this review. Moes *et al.* [98] used the Heaviside function to enrich the nodes of elements split by the crack, and for the nodes of the elements containing crack tips, a set of branch functions as seen in Eq. (1.41) from linear elastic fracture mechanics was used:

$$\begin{aligned} F(r_{cr}, \theta_{cr}) = \{ & \sqrt{r_{cr}} \sin\left(\frac{\theta_{cr}}{2}\right), \sqrt{r_{cr}} \cos\left(\frac{\theta_{cr}}{2}\right), \\ & \sqrt{r_{cr}} \sin\left(\frac{\theta_{cr}}{2}\right) \sin\left(\theta_{cr}\right), \\ & \sqrt{r_{cr}} \cos\left(\frac{\theta_{cr}}{2}\right) \sin\left(\theta_{cr}\right) \} \end{aligned} \tag{1.41}$$

where (r_{cr}, θ_{cr}) are the polar coordinates at the crack tip. However, since the stresses at the crack tip are not singular in cohesive zone modeling, alternative branch functions in which $\sqrt{r_{cr}}$ is replaced with r_{cr} or $r_{cr}^{3/2}$ or r_{cr}^2 are substituted for use. To determine the direction of crack growth, the

maximum circumferential stress criterion is used in the following manner:

$$\theta_{cr} = 2\arctan\left[\frac{1}{4}\left(\frac{K_I}{K_{II}} \pm \sqrt{\left(\frac{K_I}{K_{II}}\right)^2 + 8}\right)\right] \tag{1.42}$$

where θ is the direction of crack growth and K_I and K_{II} are the mode I and mode II stress intensity factors, respectively.

Another highly influential XFEM study for concrete was performed by Unger *et al.* [99] by again combining XFEM with the cohesive zone model. The incorporation of the XFEM enrichment functions is the same as in the work of Moes *et al.* [98] except for the addition of a correction for curved cracks. This correction is given by Eq. (1.43), and this θ_{cr} is substituted into Eq. (1.42).

$$\theta_{cr} = \arcsin\left(\frac{d_{cr}}{d_{tip}}\right) \tag{1.43}$$

Here d_{cr} is the shortest distance from the reference point to the crack and d_{tip} is the distance to the crack tip. The implementation of the cohesive zone is also improved by implementing a softening law that describes both normal and tangential tractions, as seen in Eq. (1.44).

$$\begin{aligned} w_{cr} &= \sqrt{u_n^2 + (\alpha u_t)^2}, \\ \sigma\left(w_{cr}\right) &= \begin{cases} K_p w_{cr} & \text{if } w_{cr} < w_{cr}^p \\ f_{ct} e^{\frac{-f_{ct}\left(w_{cr} - w_{cr}^p\right)}{G_f}} & \text{otherwise} \end{cases} \end{aligned} \tag{1.44}$$

Here w_{cr} is the total crack opening, u_n and u_t are the normal and tangential sliding of the interface surfaces, α is a material parameter that controls the weighting of the normal and tangential opening, w_{cr}^p is the crack opening at the peak load, K_p is the penalty stiffness, f_{ct} is the tensile strength of the interface layer, and G_f is the fracture energy. Three different criteria for crack direction determination are implemented and compared with experimental results; these include the maximum circumferential stress, the maximum energy release rate, and the minimization of total potential.

Zamani *et al.* [100] showed that high-order terms of asymptotic fields can be used for XFEM to

increase the accuracy of the stress distribution near the crack tip. Zamani *et al.* [100] performed this for both traction-free and cohesive cracks and tested stress intensity factor (SIF) criterion and stress criterion in the determination of crack growth direction. The full expressions for the enrichment functions are not shown here for the sake of brevity, but they can be found in the cited paper. Zamani *et al.* [100] showed that the higher order enrichment functions increased the accuracy of the simulations when compared to similar studies of lower order functions.

Next, aspects of regularization is discussed within the XFEM framework. In an XFEM framework, regularization can be handled along with the combination of a damage mechanics-based approach [101]. For example, in the work of Roth *et al.* [101], a regularized local anisotropic continuum damage approach is used to describe the first stage of the FPZ formation. Once the damage reaches a critical value, the analysis switches to a cohesive XFEM approach. Central to the approach of Roth *et al.* [101] is the calculation of the nonlocal stress at point $\mathbf{x}$, $\bar{\boldsymbol{\sigma}}(\mathbf{x})$ where

$$\bar{\boldsymbol{\sigma}}(\mathbf{x}) = \frac{\int_{\mathcal{R}} \upsilon(\mathbf{x}-\mathbf{x}')\boldsymbol{\sigma}(\mathbf{x}')\,\mathrm{d}\mathbf{x}'}{\int_{\mathcal{R}} \upsilon(\mathbf{x}-\mathbf{x}')\,\mathrm{d}\mathbf{x}'} \tag{1.45}$$

where $\boldsymbol{\sigma}(\mathbf{x}')$ is the Cauchy stress at point $\mathbf{x}'$, and $d\mathbf{x}'$ is a line element. The region $\mathcal{R}$ is a circle of radius equal to an intrinsic material length scale with point $\mathbf{x}$ being the centroid of the circle, and point $\mathbf{x}'$ being a material point within region $\mathcal{R}$. Finally, $\upsilon(\mathbf{x}-\mathbf{x}')$ represents a kernel function.

1.3.7 Cohesive zone model

The cohesive zone model (CZM) is a general fracture mechanics model that defines a cohesive zone around the crack tip. In this zone, the material experiences cohesive traction forces that weaken as the crack opens according to a softening law. As the separation of the crack faces approaches a critical value, the stresses in the cohesive zone gradually decrease until the critical length is reached (see Fig. 1.35) and the traction stresses become zero. This method was proposed by Hillerborg *et al.* [37] for concrete, and a full review of the method can be found in the review by Elices *et al.* [102].

The softening law can be considered as a material property, and it can be derived either from

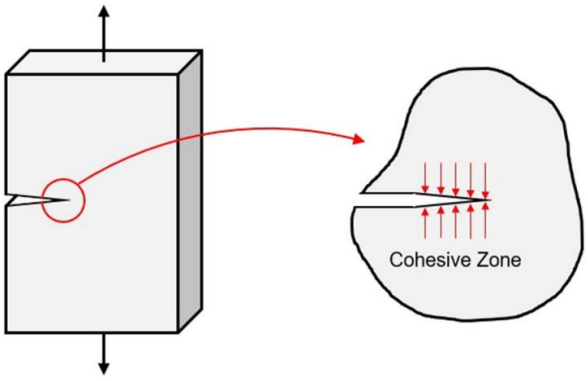

Figure 1.35: Representation of a cohesive zone near a crack tip [4].

experiments or from micromechanical models. Different formulations of softening laws are the basis for various research studies focused on CZM. Two important properties for defining the softening law are the the fracture energy G_f, and the characteristic length l_{ch}. The definition of G_f is shown in Eq. (1.46), and l_{ch} was previously defined in Eq. (1.1):

$$G_f = \int_0^{w_{cr}^c} \sigma_{czm}(w_{cr}) \mathrm{d}w_{cr} \tag{1.46}$$

In this equation, w_{cr} is the crack opening width, w_{cr}^c is the critical crack opening width at which cohesive traction becomes zero, and $\sigma_{czm}(w_{cr})$ is the cohesive traction as a function of the crack width. The characteristic length is an inverse measure of the brittleness of the material, and it is directly related to the size of the FPZ. The function $\sigma_{czm}(w_{cr})$ represents the softening, *i.e.,* how the stress will decrease as crack width increases. Hillerborg originally approximated this relationship with a simple linearly decreasing function, but many other relationships have been proposed, such as bilinear models, exponential models, and potential-based models. Park *et al.* [103] undertook a critical review of proposed constitutive relationships between the traction and displacement in the cohesive zone, particularly potential-based models.

Tijssens *et al.* [104] utilized a CZM method that incorporated an effective cohesive separation

that includes both normal separation and tangential separation as shown in Eq. (1.47).

$$\bar{\Delta}^2 = \Delta_n^2 + \alpha\Delta_t^2 \tag{1.47}$$

Here $\bar{\Delta}$ is the effective separation, Δ_n is the normal separation, Δ_t is the tangential separation, and α is a parameter to vary the weight of the tangential separation. This effective separation was incorporated into both linear and exponential softening functions. It was found that the exponential softening function was more accurate than the linear softening funcion, but further improvements were needed to gain better alignment with experimental results.

Roesler *et al.* [105] proposed a CZM method with a bilinear softening law for the purpose of modeling fracture behavior of concrete. For the bilinear softening law, the tractions increase until the critical traction is reached; after this point, the tractions begin softening in a linear fashion. Once the tractions reach a second critical value, another linear softening relation with a lower slope is employed. To characterize the softening law, initial fracture energy (G_0), total fracture energy (G_f), and the concrete tensile strength (f_t) were determined experimentally and used to calculate the coordinates of the softening curve. A parameter p of value between 0.15 and 0.33 is introduced and multiplied by f_t to determine the traction at the transition to the second softening curve. The horizontal axis intercepts of the two softening curves are described in Eq. (1.48).

$$w_1 = \frac{2G_0}{f_t}, \quad w_f = \frac{2}{pf_t}\left[G_f - (1-p)\,G_0\right] \tag{1.48}$$

Yang *et al.* [106] attempted to account for the heterogeneity of concrete by combining CZM with Monte Carlo simulations. Pre-inserted cracks were distributed in the material using Weibull random fields, and material property heterogeneities were randomly applied through various numerical algorithms. An effective crack separation was incorporated in the same manner as in [104] with an α value of 1. A linear softening law was applied to the randomly inserted cracks. Fracture properties were then randomly applied to the domain, resulting in a heterogeneous distribution of both preexisting cracks and fracture properties. Many tests were performed and studied to deter-

mine the statistical significance of the random properties. These were compared with homogeneous simulations, and the Monte Carlo simulations agreed more accurately with the experimental data.

An important disadvantage of the standard CZM is the inability to characterize the interaction between mode I loading and mode II loading for a mixed-mode case. While the other studies described before employed an effective crack opening to address this, Most *et al.* [107] proposed a solution to this using an energy-based meshless cohesive zone at the crack tip. Most used a hyperbolic yield surface to describe the fracture process as a function of a Coulomb friction coefficient and both shear and tensile strengths. The shear and tensile strengths were softened according to an exponential function shown in Eq. (1.49)

$$\begin{aligned} \chi &= \chi_0 - \chi_0 f_s \left(\frac{W_f}{G_f^I}, p_\chi^{sh} \right), \\ c &= c_0 - c_0 f_s \left(\frac{W_f}{G_f^{II}}, p_c^{sh} \right) \end{aligned} \tag{1.49}$$

where χ is the tensile strength, c is the shear strength, W_f is the fracture work, G_f^I is the mode I specific fracture energy, G_f^{II} is the mode II specific fracture energy, and the scaling function f_s represents softening controlled by the shape parameters p_χ^{sh} and p_c^{sh}. For this study, p_χ^{sh} and p_c^{sh} were chosen to represent an exponential softening curve. The results of this method were compared with standard CZM results and experimental data for mixed-mode tests, and the mixed-mode CZM results showed improved agreement with the experiments compared to the standard CZM results. An example of this comparison is shown for the L shaped panel test conducted by Winkler [33] in Fig. 1.36.

Because the CZM does not inherently describe a descretized finite element formulation, it is commonly combined with other fracture modeling methods described in this review, especially XFEM, peridynamics, and phase field approaches. These other frameworks will use CZM to describe the fracture criteria and the behavior of the traction stresses near the crack tip, but the remainder of the formulations remain the same. Thus, while regularization of CZM itself is not possible, regularization of the other methods that can incorporate CZM is a topic of interest.

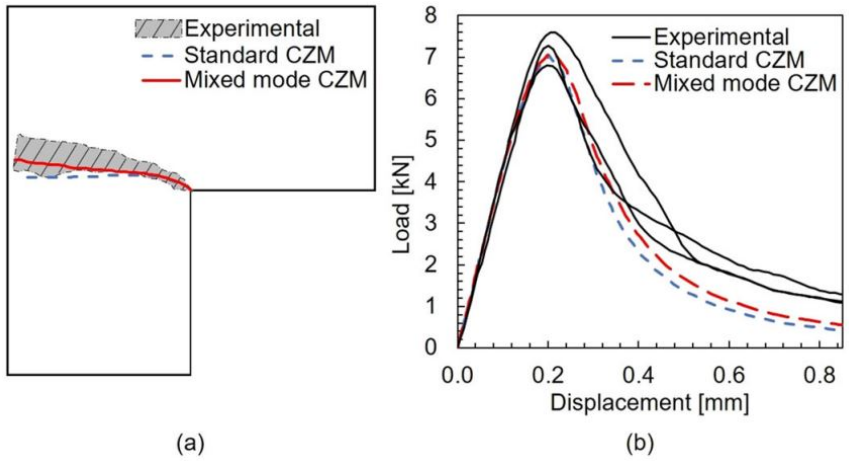

Figure 1.36: Comparison of numerical and experimental results of L shaped panel test for the improved CZM from Most *et al.* [107]: (a) Crack propagation path, and (b) Load-displacement curve.

1.3.8 Lattice discrete particle model

A lattice discrete particle (LDP) model considers the heterogeneous nature of concrete by introducing different phase materials of concrete [108]. Therefore, this method is an example of a *multiscale* approach for modeling concrete response. From the direct description of components of concrete, which are aggregates, mortar, and interfacial transition zone, the model has an advantage in representing heterogeneity and damage localization behavior in concrete compared to the continuum models [109]. The LDP model can be further improved considering the effect of chemical reactions, such as alkali-silica-reaction, on the damage behavior of concrete [110]. Since the model considers the size distribution of aggregates in concrete, a close relationship can be found with mesoscale modeling [111].

Concrete modeling with LDP consists of two major parts: generating lattice domain and imposing constitutive behavior at the interfacial transition zone [112]. The center of the coarse aggregates is dispersed in the numerical domain as nodal points either in regular or irregular grids. The nodal points are occupied with random poly-sized spheres, which represent aggregate particles. The size distribution of aggregate particles follows the sieve curve used in the target material, and the dis-

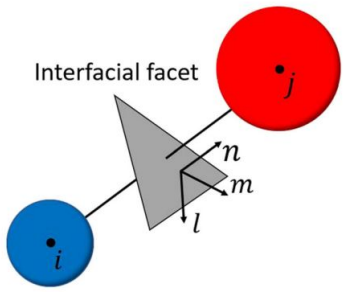

Figure 1.37: Schematic diagram for the lattic discrete particle method showing an interfacial facet between node i and node j. A possible crack can occur at surrounding facets of aggregate particles [109].

persed particles achieve densely graded distributions throughout the domain. The lattice system is generated by connecting nodal points of aggregates through Delaunay tetrahedralization, where the tetrahedral mesh edges define the connectivity of the nodes. Dual to the generated lattice system, the modified Voronoi diagram is applied to define the facets around each aggregate particle. The LDP cells are formed by facets surrounding an inside particle, and the facets of lattice cells are considered as locations of potential cracks. A rigid body motion decides the motion of every cell, and the constitutive behaviors of concrete are imposed on facets of the LDP cell [109]. The surface of facet perpendicular to the node i and node j is appeared in Fig. 1.37, where an unit vector $\boldsymbol{n}$ shows normal direction and unit vectors $\boldsymbol{m}$, and $\boldsymbol{l}$ show two shear directions of the facet.

The matrix expressions of stress $\boldsymbol{\sigma} = [\sigma_N \ \sigma_M \ \sigma_L]^{\mathrm{T}}$ and strain $\boldsymbol{\varepsilon} = [\varepsilon_N \ \varepsilon_M \ \varepsilon_L]^{\mathrm{T}}$ are defined on each facet with the normal and shear components as shown in Eq. (1.50)

$$\varepsilon_N = \frac{\boldsymbol{n}^{\mathrm{T}}\,[|\mathbf{u}_c|]}{l^e},\ \varepsilon_M = \frac{\boldsymbol{m}^{\mathrm{T}}\,[|\mathbf{u}_c|]}{l^e},\ \varepsilon_L = \frac{\boldsymbol{l}^{\mathrm{T}}\,[|\mathbf{u}_c|]}{l^e} \tag{1.50}$$

where $[|\mathbf{u}_c|]$ is a displacement jump between node i and node j; and l^e is a distance between the nodes. Before an inelastic behavior from damage, elastic behavior is imposed as constitutive

behavior on each facet. The equation for the elastic relation is shown in Eq. (1.51)

$$\boldsymbol{\sigma} = E_0 \boldsymbol{G} \boldsymbol{\varepsilon}, \quad \boldsymbol{G} = \begin{bmatrix} 1 & 0 & 0 \\ 0 & \alpha & 0 \\ 0 & 0 & \alpha \end{bmatrix} \tag{1.51}$$

where E_0 is an effective normal modulus; and α is a shear-normal coupling parameter.

Fascetti *et al.* [112] used an elliptical stress curve to address the boundary limits of the tension, compression, and shear stresses at the interfacial transition zone. If the stress state violates the predefined stress curve, the damage occurs at a facet, and the stress state follows an exponential decay to express softening behavior. A coupling strain w^* was introduced to represent the source of the cohesive response under a tension-shear interaction loading condition. The expression of the coupling strain is shown in Eq. (1.52)

$$\tan w^* = \frac{\varepsilon_N}{\sqrt{\alpha}\varepsilon_T} = \frac{\sigma_N \sqrt{\alpha}}{\sigma_T} \tag{1.52}$$

where $\sigma_T = \sqrt{\sigma_M^2 + \sigma_L^2}$ is a tangential stress. The effective strain and stress were defined as Eq. (1.53).

$$\varepsilon = \sqrt{\varepsilon_N^2 + \alpha \varepsilon_T^2}, \; \sigma = \sqrt{\sigma_N^2 + \frac{\sigma_T^2}{\alpha}} \tag{1.53}$$

The exponential decay form of the stress expression to express the softening behavior is shown in Eq. (1.54)

$$\sigma_b = \sigma_{h0} e^{-\frac{\bar{H}}{\sigma_{h0}} \langle \varepsilon_h - \varepsilon_{h0} \rangle} \tag{1.54}$$

where σ_{h0} and ε_{h0} are the effective stress and strain at the starting of damage for the element; and $\varepsilon_h = \sqrt{\varepsilon_{N,max}^2 + \alpha \varepsilon_{T,max}^2}$ is a history value of the effective strain achieved in the element. The subscript max describes the maximum value of strain achieved until a certain calculation step. The coefficient $\bar{H}$ in Eq. (1.54) is used to match the energy dissipation in the macroscale and mesoscale. The expression for the coefficients for the energy dissipation in pure shear and pure tension, H_s

and H_t, respectively, are shown in Eq. (1.55)

$$\bar{H}(w^* = 0) = H_s = \frac{2\alpha E_0}{(2\alpha E_0 G_s)/(\sigma_s^2 l^e) - 1},$$
$$\bar{H}(w^* = \pi/2) = H_t = \frac{2E_0}{(2E_0 G_t)/(\sigma_t^2 l^e) - 1} \tag{1.55}$$

where G_s and G_t are the material parameters which represent the mesoscale fracture energy in shear and tension, respectively; and σ_t, σ_c, and σ_s are the material parameters which address mesoscale limits in tension, compression, and shear. The material parameters of the Eq. (1.55) were determined from the experimental data. If the damage was not occurred either from pure tension($w^* = \pi/2$) or pure shear ($w^* = 0$), the coefficient $\bar{H}$ was having a form in Eq. (1.56)

$$\bar{H}(w^*) = H_s + (H_t - H_s)\left(\frac{2w^*}{\pi}\right)^{n_t} \tag{1.56}$$

where n_t decides the shape of the softening behavior. The proposed model also described the response of the concrete under the compressive stress state. The negative normal strain was decomposed into volumetric and deviatoric parts to address postpeak compressive behavior. Under the negative normal strain, the stress response followed perfectly plastic behavior for the positive volumetric strain and showed hardening behavior for the negative volumetric strain. The frictional behavior under the compression was described with an exponential law, where the expression was similar to the cohesive behavior expression of Eq. (1.54). The different definition of the coefficient $\bar{H}$ was used to describe the frictional behavior for the coupling strain range of ($-\pi/2 \leq w^* \leq 0$). The material parameters for the mesoscale model were determined through the conducted experiments with mortar specimens. The proposed model with the calibrated mesoscale parameters was validated through the compression test with concrete specimens by comparing stress-strain data.

Although the LDP model for the concrete modeling succeeded in representing softening behavior under tension-shear state and frictional behavior in compression state, a treatment of a crack closure is not available at the present moment. The mesh sensitivity test showed converged results

with the coarse and fine mesh, although a specific regularization method was not introduced in the LDP model [113]. A hint of regularization in the lattice model can be found in a nonlocal lattice spring model. The nonlocal lattice spring model calculates the total energy of a unit lattice cell with the consideration of the potential energies of the neighbor elements. With increasing the packing distance of neighbor lattice cells, the crack propagation path and the force-displacement curve show converging response [114].

2. MULTIPLE CRACKING MODEL UNDER GRAPH-BASED FINITE ELEMENT ANALYSIS[1]

A multiple cracking model combines the best features of damage mechanics (ease of implementation with thermodynamic consistency) and discrete crack models. The core idea is based on the notions of microcrack normals [115]. Marshall et al. [116] used such an approach combined with a modified Cosserat continuum model to develop models for microcracking in rocks. In contrast to these approaches where there is a single microplane normal that evolves with time, the approach developed by Bazant and coworkers [117] utilize constitutive relations for a single microplane and then integrate over all possible orientations of the microplane using the equivalent of a microplane orientation distribution function (ODF). However, the proposed model follows a different strategy, which may refer to as a "discrete microplane approach". Here instead of one microplane with an evolving normal or an evolving ODF, the model introduces a finite number of discrete microplanes where fracture can propagate. This is no doubt more restrictive than using the whole ODF but it is done keeping computational approaches in mind—the model will end up with the discretization of the microplane orientations anyway.

This approach has the added advantage of being able to accommodate single crack growth quite easily while allowing crack branching and oriented cracks, without the problems of crack spreading which is inherent in damage mechanics. Furthermore, in the model presented here, the elastic response is identical to that of a conventional elastic solid and it is only the fracture response that is nonlocal. By judicious separation of the crack opening description (which is purely kinematical in this approach) from crack kinetics, the model is capable of accommodating a wide range of different fracture criteria without having to modify the underlying finite element implementations. This ensures that the model can "piggy back" on existing or legacy finite element codes since it is an extension and not a reworking of the whole model. The model will focus only

[1]Reprinted from the original reference of "Multiple cracking model in a 3D GraFEA framework" by A.R. Srinivasa, H.Y. Shin, P. Thamburaja, and J.N. Reddy, 2021. *Continuum Mechanics and Thermodynamics* , 33, 1409-1428.

on small deformations for immensely practical reasons—most brittle and quasi-brittle materials can sustain only small deformations before widespread fracture.

The presented work in this section describes the damage evolution in a probabilistic manner, where the probability of material intact is expressed with damage variable having the value from 0 to 1. Here, I introduce a master equation which governs the rate of change of the probability density using ideas based on population dynamics [118]. The notable features of the approach presented here are:

1. The introduction of a finite number K of possible crack normals (or microplane two-forms) at each point.

2. A kinematical way to account for crack opening and closing, which is completely separated from the kinetics. This is a novel idea and substantially simplifies and broadens the applicability of the model.

3. The model assumes that the microcracking at a location is a random variable field with two possible values (1 = intact, 0 = broken) at each location. The model introduces the survival probability ϕ_i which is the probability that the i-th microplane is intact at time t.

4. The development of an equivalent elastic strain $\mathbf{E}^{\phi}$ which is the expectation (over the survival probability of the microcracks) of the normal strains across the open crack faces. This plays a similar role as the elastic strains in plasticity models.

5. The use of the master equation for the evolution of the survival probability with time with a nonlocal transition probability. The irreversibility of fracture or the possibility of healing can be enforced here.

6. A model for the nonlocal interactions based on probabilistic population dynamics.

The present model is developed based on the use of the Clausius–Duhem inequality. The model is specialized for quasi-brittle material fracture and obtains values for the constants from experimental data in the literature. The model then shows by means of a simple homogeneous deformation

(a) (b)

Figure 2.1: (a) A three-dimensional view of the possible micro cracks or fracture microplanes intersecting at a material point, (it shows only six microplanes but many more can be accommodated) and (b) the corresponding normal directions to the fracture microplane surfaces at the material point.

response that its rate dependent microcracking response as well as the bilinear response due to crack closure can be simulated.

2.1 Constitutive theory development

The model considers a (uncracked) body occupying its reference configuration at time t=0. The typical material point of the body in this configuration is location $\mathbf{x}$. Let $\mathbf{u}(\mathbf{x}, t)$ be the displacement field of the body. The model assumes that the body undergoes a small deformation during which it is capable of undergoing damage in the form of numerous micro cracks (more on this shortly). Let $\mathbf{v} = \dot{\mathbf{u}}$ be the velocity of a material point and $\boldsymbol{\sigma}$ represent the stress for the body. The usual balance laws are assumed to hold irrespective of whether the body cracks or not, that is (in the absence of body forces)

$$\operatorname{div} \boldsymbol{\sigma} = \rho \dot{\mathbf{v}} , \quad \boldsymbol{\sigma} = \boldsymbol{\sigma}^{\top} \tag{2.1}$$

where ρ represents the material density.

To illustrate the possible microplane cracks or micro cracks at a material point, The model is guided by the schematic diagram shown in Fig. 2.1(a) displaying the possible crack planes

intersecting at a material point. Each crack plane surface is identified by a normal direction to the crack plane *cf.* Fig. 2.1(b). At each location $\mathbf{x}$, the model assumes that there can be at most N microcrack surfaces or fracture microplanes with surface normals $\mathbf{n}_i$ where integer $i = 1, 2, \ldots, K$, and that these crack normal directions are known a *priori*[2]. I will discuss the choice of these crack normals in Section 3. Since these cracks are internal, the model has no way of knowing whether any of the possible cracks are really open or not. To account for this, the model provides a probabilistic description of the state of any microplane, that is, any microplane can be in a state S which can take one of two values: "intact" ($S = 1$) and "fractured" ($S = 0$). The model now introduces $\phi_i(\mathbf{x})$ which represents the "intactness" or "survival probability" of the ith microcrack surface, so that $\phi_i(\mathbf{x}, t)$ is the probability that the ith microplane at $\mathbf{x}$ is intact at time t. Thus, $\phi_i(\mathbf{x}) = 1$ implies that the ith crack at $\mathbf{x}$ has definitely not occurred while $\phi_i(\mathbf{x}) = 0$ implies that the ith crack at $\mathbf{x}$ has definitely occurred.

2.1.1 Damage in crack plane

Let $\boldsymbol{\varepsilon}$ denote the small strain tensor for the body. As the body deforms, the nominal strain across the crack face is given by $e_i := \boldsymbol{\varepsilon} \bullet (\mathbf{n}_i \otimes \mathbf{n}_i)$.

To write this in a more convenient way and to keep the notation simple, The model utilizes the Voigt vector notation and define a 6×1 strain column vector $\mathbf{E}$ as

$$\mathbf{E} := [\boldsymbol{\varepsilon}_{xx}, \boldsymbol{\varepsilon}_{yy}, \boldsymbol{\varepsilon}_{zz}, \sqrt{2}\,\boldsymbol{\varepsilon}_{yz}, \sqrt{2}\,\boldsymbol{\varepsilon}_{xz}, \sqrt{2}\,\boldsymbol{\varepsilon}_{xy}]^\top \tag{2.2}$$

In the above definition, the model has used a factor of $\sqrt{2}$ on the off-diagonal terms to ensure that the vector and symmetric matrix norms agree.

Similarly the model will define a 6×1 column vector $\mathbf{N}_i$ as

$$\mathbf{N}_i := [n_{ix}^2, n_{iy}^2, n_{iz}^2, \sqrt{2}\,n_{iy}n_{iz}, \sqrt{2}\,n_{ix}n_{iz}, \sqrt{2}\,n_{ix}n_{iy}]^\top, \quad i = 1, 2, \ldots, K \tag{2.3}$$

[2]While the fact that there can be only *K* cracks of known normals is limiting from a theoretical point of view, the model points out that when the body is discretized, it will have no option but to limit the number of cracks anyway.

In terms of these variables, the model can see that

$$e_i = \mathbf{N}_i \bullet \mathbf{E} \tag{2.4}$$

Turning now to crack face i, it is easy to see that the spatial length between two points on the crack face normal which are at a distance dl_i apart can be obtained as $(1 + e_i)\, dl_i$. However, if the crack is open, and the model measures the "material distance", that is, if it is measured by counting only the material points and skipping the open crack, they will be the same as the original length dl_i, i.e., the "material elastic strain" will be zero. Of course, the situation is different for a closed crack. Here the "material elastic strain" will be the total strain.

Since the probability that there is no crack is ϕ_i , the *expected* value of the material elastic strain across the crack face is then

$$e_i^e = \begin{cases} \phi_i e_i \text{ if } e_i > 0 \\ e_i \text{ if } e_i \leq 0 \end{cases} \tag{2.5}$$

which can be conveniently written as

$$e_i^e = (\phi_i - 1) < e_i > + e_i \tag{2.6}$$

where $< x >:= (x + |x|)/2$ is the "ramp function" which is zero if $x < 0$ and x if $x > 0$. The above definition of material elastic strain across the crack face allows for accounting for crack closure and for opening in an extremely simple kinematically plausible way rather than obtaining it through the use of different energy functions in tension and compression and the difficulties associated with defining these correctly.

2.1.2 Material equivalent strain tensor

Equivalent elastic strain tensor $\mathbf{E}^{\phi}$ is assumed to be (at least approximately) the strain in the body at the same state of stress if there were no cracks. This is similar to the notion of an elastic strain in an elasto-plastic material as well as the idea of an equivalent undamaged body. However,

here this notion is defined in a purely kinematical way.

The model postulates that, the equivalent elastic strain tensor should reduce to (2.6) across each crack normal, that is, $\mathbf{N}_i \bullet \mathbf{E}^\phi = e_i^e$. However this is impossible unless there are exactly six independent crack normals at a given point. For finite elements using tetrahedral simplices, this condition is very conveniently and uniquely satisfied if the normals $\mathbf{n}_i$ are taken to be parallel to the element edges, that is, the cracks are assumed to propagate perpendicular to the element edges. If the model uses more than six crack normals, the model can define an equivalent elastic strain that satisfies the above condition in a *least-squares* sense, that is,

$$\mathbf{E}^\phi := \text{argmin}_{\mathbf{A}} \sum_i (|| \, \mathbf{N}_i \bullet \mathbf{A} - e_i^e \, ||^2) \tag{2.7}$$

where $\mathbf{A}$ represents a 6×1 matrix. A routine calculation involving the minimization of a quadratic function reveals that the model can obtain an explicit representation for the equivalent elastic strain of the form

$$\mathbf{E}^\phi = \sum_i e_i^e \, \mathbf{B}[\mathbf{N}_i] \tag{2.8}$$

where the 6×6 matrix $\mathbf{B}$ is given by

$$\mathbf{B} := \left(\sum_i \mathbf{N}_i \mathbf{N}_i^\top \right)^+ \tag{2.9}$$

where $\mathbf{B}$ is the *pseudo-inverse* of matrix $\sum_i \mathbf{N}_i \mathbf{N}_i^\top$. It is also important to emphasize that $\mathbf{B}$ is *unique* and that

$$\mathbf{B} = \left(\sum_i \mathbf{N}_i \mathbf{N}_i^\top \right)^{-1} \quad \text{if} \quad \sum_i \mathbf{N}_i \mathbf{N}_i^\top \quad \text{is not singular}$$

Since the mathematical descriptions for the microplane fracture surfaces and slip systems in crystal plasticity are analogous, the model has used the pseudo-inverse method for calculating quantity $\mathbf{B}$.

The quantities $\mathbf{B}$ and $\mathbf{N}_i$ are not functions of time, and therefore it can be written as

$$\mathbf{E}^{\phi} = \sum_i e_i^e \, \mathbf{Z}_i \quad \text{where} \quad \mathbf{Z}_i := \mathbf{B}[\mathbf{N}_i] \tag{2.10}$$

Several observations can be made about the equivalent elastic strain $\mathbf{E}^{\phi}$:

1. If there are exactly 6 possible independent crack normals, then $\mathbf{E}^{\phi}$ will satisfy $\mathbf{N}_i \bullet \mathbf{E}^{\phi} = e_i^e$ exactly.

2. It vanishes only if all the possible cracks are guaranteed to be broken, that is, $\phi_i = 0$ for all i.

3. It accounts for crack closure on each crack front in a least-squares sense.

4. In two dimensions it reduces to the form developed by Khodabakhshi *et al.* [119, 120].

5. It is not explicitly related to any constitutive model, being purely kinematic in nature. This allows for the approach presented here to be used in conjunction with *any* constitutive relation of choices.

6. Due to the crack closure conditions it can be noted that $\mathbf{E}^{\phi}$ is *not* linear in $\mathbf{E}$ even for small deformations, so that the behavior of this material is fundamentally nonlinear (this will become obvious with the simulation results from the homogeneous cracking response where crack closure and the bilinear response will become evident under cyclic loading).

2.1.3 Constitutive modeling

Note that up until now, no mention has been made about stresses or constitutive relations, further highlighting the fact that entire approach including conditions for crack closure are entirely kinematical in nature.

A definition of the constitutive relations can be started with the specific Helmholtz potential, ψ

as a function of the equivalent elastic strain $\mathbf{E}^{\phi}$ of the form

$$\psi = \psi_0(\mathbf{E}^{\phi}) + \psi_1(\phi_1, \phi_2, \ldots, \phi_K) \tag{2.11}$$

Here the first term on the right-hand side is due to the strain energy of the cracked solid while the second term on the right-hand side accounts for the surface energy created by cracking. The model now introduces the stress $\boldsymbol{\sigma}$ and its six dimensional vector version $\mathbf{T}$ as

$$\mathbf{T} := [\sigma_{xx}, \sigma_{yy}, \sigma_{zz}, \sqrt{2}\,\sigma_{yz}, \sqrt{2}\,\sigma_{xz}, \sqrt{2}\,\sigma_{xy}]^{\top} \tag{2.12}$$

With this notation, the mechanical dissipation equation (that is, the isothermal form of the Clausius–Duhem inequality) becomes

$$\mathbf{T} \bullet \dot{\mathbf{E}} - \dot{\psi} = \mathbf{T} \bullet \dot{\mathbf{E}} - \dot{\psi}_0 - \dot{\psi}_1 = \xi \geq 0 \tag{2.13}$$

where ξ denotes the mechanical dissipation density. By repeated use of the chain rule and taking the time derivative of e_i^e in (2.6), the model can obtain

$$\dot{e}_i^e = \dot{\phi}_i < e_i > \; + \; (1 + (\phi_i - 1)H(e_i))\, \dot{e}_i \tag{2.14}$$

where $H(e_i)$ is the unit step function of quantity e_i .

The use of step and ramp functions to describe the elastic response of bilinear materials that have different responses in tension and compression, is unavoidable. Our approach moves this all to kinematics which is really the source of this bilinearity in these quasi-brittle materials.

Using this notation, the model can show that (2.13) can be rewritten as

$$(\mathbf{T} - \mathbf{T}^{\phi}) \bullet \dot{\mathbf{E}} \; - \; \sum_i (a_i < e_i >)\, \dot{\phi}_i = \xi \geq 0 \tag{2.15}$$

where the elastic stress $\mathbf{T}^{\phi}$ is

$$\mathbf{T}^{\phi} := \frac{\partial \psi}{\partial \mathbf{E}} = \sum_i \{(1 + (\phi_i - 1)\, H(e_i))\sigma_i \mathbf{N}_i\} \quad \text{with} \quad \sigma_i := \frac{\partial \psi_0}{\partial \mathbf{E}^{\phi}} \bullet \mathbf{Z}_i \tag{2.16}$$

and σ_i is the normal stress component on each possible crack face i. The model also has

$$a_i = \sigma_i - \frac{\partial \psi_i}{\partial \phi_i} \tag{2.17}$$

as the cracking force for the ith crack face.

2.1.4 Crack closure properties of the model

Notice that the elastic stress in the body is the sum of the stress across each crack face i modified by $(1 + (\phi_i - 1)H(e_i))$. If crack i is guaranteed to be intact (that is, $\phi_i = 1$) then this modification disappears and the model gets the usual elastic stress. On the other hand, if $\phi_i = 0$, crack i is definitely present and then the model obtains a *bimodal* response, that is, if $e_i > 0$ then the crack has no strength at all whereas if $e_i < 0$ the crack is fully shut and the material behaves elastically as if there is no crack.

With the crack growth driving force on each microplane $\gamma_i \equiv a_i < e_i >$, the model now assumes that, in the absence of crack growth ($\dot{\phi}_i = 0$ for all i) the material is elastic so that $\mathbf{T} = \mathbf{T}^{\phi}$. Furthermore, for each microplane i, the condition $\gamma_i > 0$ must be satisfied during crack growth, that is, $\dot{\phi}_i < 0$.

2.1.5 Evolution of survival probability

The model borrows from probability theory where “master equations" (see e.g. [121] eqn. 7) are used to describe the time evolution of a system that is a probabilistic combination of discrete states and the switching between states is determined by a transition rate function. Suppressing the integer i for the moment (for the sake of clarity), in our case any microplane can exist in only two states: intact (I) or fractured (F). Correspondingly, the probability of a microplane being in either state is $\phi^I := \phi$ and $\phi^F = 1 - \phi$.

The model now considers details of how the survival probability of a fracture microplane evolves. As with other Markov processes, the survival probability can be written in terms of a master equation. There are only two transitions possible for every microplane – transition from intact to fractured (leading to crack growth) and transition from fractured to intact (indicating healing). In a time interval dt, the rate of change of the probability density is given by the well-known master equation (involving events that move into the state – those that move out)

$$d\phi = -\phi G(I \rightarrow F)dt + (1-\phi)G(F \rightarrow I)dt \tag{2.18}$$

where the transition probability $G(I \rightarrow F)$ is the probability of breakage of the microplane, and $G(F \rightarrow I)$ is the probability of spontaneous healing. Our current assumption is that $G(F \rightarrow I) = 0$ so that *no healing is possible*. With this assumption, the master equation for the ith fracture microplane reduces to

$$\frac{\partial \phi_i}{\partial t} = -G_i \phi_i \tag{2.19}$$

It is a simple matter to see that the above equation together with the condition $\mathbf{T} = \mathbf{T}^{\phi}$, the dissipation inequality (2.15) reduces to

$$\sum_i (a_i < e_i >)\, G_i \phi_i \geq 0 \tag{2.20}$$

Since G_i which represents the transition rate must be greater than zero, the above condition indicates that G_i must depend upon the driving force for crack opening $a_i < e_i >$, and the model will make this dependence explicit by requiring that G_i be nonzero only if a_i and e_i are greater than zero. Henceforth, the model will then refer to G_i as the “fracturing rate".

2.1.6 Nonlocal damage calculation of fracture process zone

A formulation of the model is now led to the development of the constitutive relation for the state transition rate function (i.e., fracture rate) $G_i(\mathbf{x}, t)$. As is commonly utilized in fracture mechanics, the region around a microcrack has an extremely complex distribution of strains and

usually the simplifying assumption is made that the fracture at a particular microplane at any point is influenced by the state of strain in a small but finite *fracture process zone* (FPZ) of the material point in question [122]. There are two approaches to the development of such ideas: using higher gradients of the state variables (such as the approach underlying phase field models) or using an integral approach using kernel functions [123]. The latter approach is more suited and natural to the probabilistic approach presented here. The model borrows from the work on spatial population distribution models (see [118] eqs. 3-8) from population biology when developing the transition probability functions that it is described here.

The core idea here is that the fracturing probability is influenced by other locations through an integral expression using a “competition kernel" [118]. This kernel is a function of the distance from the current point and represents the interaction of the current microplane with the others in its vicinity. In the current context it is more appropriate to call it the influence kernel.

To begin the development of this kernel and the general fracturing probablity, at each point x the model defines the *expected number of survivors* as

$$\Phi(\mathbf{x}) = \sum_i \phi_i(\mathbf{x}, t) \tag{2.21}$$

where Φ is a real number between 0 and N (the maximum number of microplanes at $\mathbf{x}$) and is exactly equal to zero if no microplane is intact and N if all microplanes survive. This implies that the average survival probability of any crack at point $\mathbf{x}$ is $\omega(\mathbf{x}) = \Phi(\mathbf{x})/N$.

From fracture mechanics, the rate of cracking depends upon the strain field of its immediate surrounding [124, 125]. However it should be excluded from the model consideration of those points that are already fully cracked since they have no load bearing capacity under tension. In ecological terms only those animals or plants that are in the immediate vicinity of the current animals or plant that are alive can participate. Thus the influence is modified the probability that both the microplane at $\mathbf{x}$ and the microplanes at other points $\mathbf{y}$ are intact or not.

The joint survival probability of microplane i at location $\mathbf{x}$ and the microplanes at location $\mathbf{y}$

(assuming independence) is

$$P_i(\mathbf{x}, \mathbf{y}) = \phi_i(\mathbf{x})\, \omega(\mathbf{y}) \tag{2.22}$$

With this definition, the net influence of the strain at point $\mathbf{y}$ on the cracking at point $\mathbf{x}$ is defined as

$$I_i(\mathbf{x}) = (1/A(\mathbf{x})) \left\{ \int \Omega(\mathbf{x} - \mathbf{y}) P_i(\mathbf{x}, \mathbf{y}) \mathbf{E}(\mathbf{y})\, dV \right\} \bullet \mathbf{N}_i(\mathbf{x}) \tag{2.23}$$

where $\Omega(\mathbf{x} - \mathbf{y})$ is the influence kernel which delineates the FPZ, and $A(\mathbf{x})$ is the normalization factor defined by

$$A(\mathbf{x}) = \int \Omega(\mathbf{x} - \mathbf{y})\, \omega(\mathbf{y})\, dV \tag{2.24}$$

with dV being the volume element. Following [126], the model takes the influence kernel $\Omega(\mathbf{x} - \mathbf{y}) = H(\, r_\phi - |\mathbf{x} - \mathbf{y}|\,)$ where $r_\phi > 0$ is a *material parameter* which sets the size of the FPZ. Hence, r_ϕ is an intrinsic material length scale which controls the fracture process in the material. Turning now to the main task, the model knows that

1. The fracture rate G_i must be zero when either the cracking force a_i or the normal strain on the microplane i are negative.

2. It will grow only as long as the crack continues to open only as long as $\dot{e}_i > 0$.

3. G_i depends upon the state of the FPZ through the influence function I and will not rupture until the influence exceeds a critical threshold I_i^c.

A close examination of Eq.(2.23) reveals that the I_i can be considered as an *equivalent normal strain* on microplane i. Given these criteria, the model now assumes that the fracture rate function is given by

$$G_i = G_0 H(a_i) H(e_i) < I_i - I_i^c >< \dot{e}_i > \tag{2.25}$$

where $G_0 > 0$ is a constant which is assumed to be the same for all microplanes everywhere.

2.1.7 Rate dependence of fracture response

The constitutive relations that have been developed so far allow for two different sources for rate dependent behavior: 1. The stress response $\mathbf{T}$ can be rate dependent [127]. Such a possibility indicates that the material is rate dependent even in the absence of cracks. 2. the crack growth threshold I^c is *rate dependent* [127].

To be specific, if I_i^c is constant, it can easily be verified from a close perusal of Eqs. (2.19) and (2.25) that the equation for the crack growth rate will be homogeneous of order 1 in strain-rates, indicating that the response will be rate independent (although irreversible).

However, for materials like concrete, it is well-known from experiments that bond rupture in the fracture process zone (FPZ) of concrete is sensitive to loading rates, that is, the cracking process is *rate-dependent* even with the bulk concrete sample deforming under quasi-static loading rates. Experimental data indicates that the cohesive strength against cracking *increases* with *increasing* applied strain-rate [127–130]. A general constitutive relation of the form $I_i^c = I_o^c + f(\dot{e}_i)$ can then account for rate dependent response and strengthening effect that can be seen in such materials. Here the model is guided by the experimental results in [128] which show the fracture response of the material being rate independent until the crack opening rate exceeds a critical value:

$$I_i^c/I_o^c = \begin{cases} (\dot{e}_i/\dot{e}_o)^{c_o} \ \text{ for } \ \dot{\epsilon}_i > \dot{\epsilon}_o \\ 1 \ \text{ for } \ \dot{\epsilon}_i \leq \dot{\epsilon}_o \end{cases}$$

where $I_o^c > 0$ is a constant *threshold* resistive strain against cracking, and $c_o > 0$ a constant dimensionless power-law coefficient.

2.2 Finite element simulations: Microcracking response for homogeneous deformation

The developed constitutive equations have been implemented into the Abaqus/Explicit [131] finite-element program through a vectorized user-material (VUMAT) subroutine. The efficacy of the theory is enough to model the response of cementitious materials with the baseline material parameters listed in Table 2.2. In this work, the simulations only consider homogeneous deformation

Node number	Coordinates	Displacement boundary & loading conditions		
		X direction	Y direction	Z direction
1	(-1,0,0)	·	Fixed	Fixed
2	(1,0,0)	·	Fixed	Fixed
3	(0,1,0)	Fixed	·	Fixed
4	(0,0,$\sqrt{2}$)	Fixed	Fixed	Velocity profile

Table 2.1: Boundary and loading conditions imposed on the simulation domain for simulating simple tension/compression stress states.

cases. This is admittedly an extremely simple problem meant for illustrating some aspects of the theory alone. Since the deformation is assumed homogeneous, the nonlocal effects are vastly simplified and the model can consider only the effects of loading rates and crack closure. In particular, the net influence function on each microplane i of any representative volume element reduces to the local form

$$I_i(\mathbf{x}) = \phi_i \, \mathbf{E} \bullet \mathbf{N}_i(\mathbf{x}) \,, \quad i = 1, 2, \ldots, 6. \tag{2.26}$$

As our intention is to develop a numerical scheme based on simplex shapes (triangles in two dimensions and tetrahedra in three dimensions), finite-element simulations are performed using one tetrahedron element shown in Fig. 2.2 where this element is sufficient to represent homogeneous deformation. Fig. 2.2(a) shows the three-dimensional view of the element, and Fig. 2.2(b) shows the plan view of the element. In the simulation domain, there are a total of 4 nodes with 3 nodes at the base of the element which lies on the $X - Y$ plane, and one node at the apex of the element which lies on the Z-axis. Therefore, there are 3 edges at the base of the tetrahedron element, and the remaining 3 edges of the tetrahedron element will be termed as the *side edges*.

The boundary conditions and loading conditions imposed on the domain for simulating simple tension/compression stress states are listed in Table 2.1. It can be emphasized again that the model allow a maximum possibility of six microplanes (that is, each volume element can possibly contain at most 6 cracks). In Fig. 2.2c, a three-dimensional visualization is described for the 6 possible fracture microplanes within a tetrahedron element.

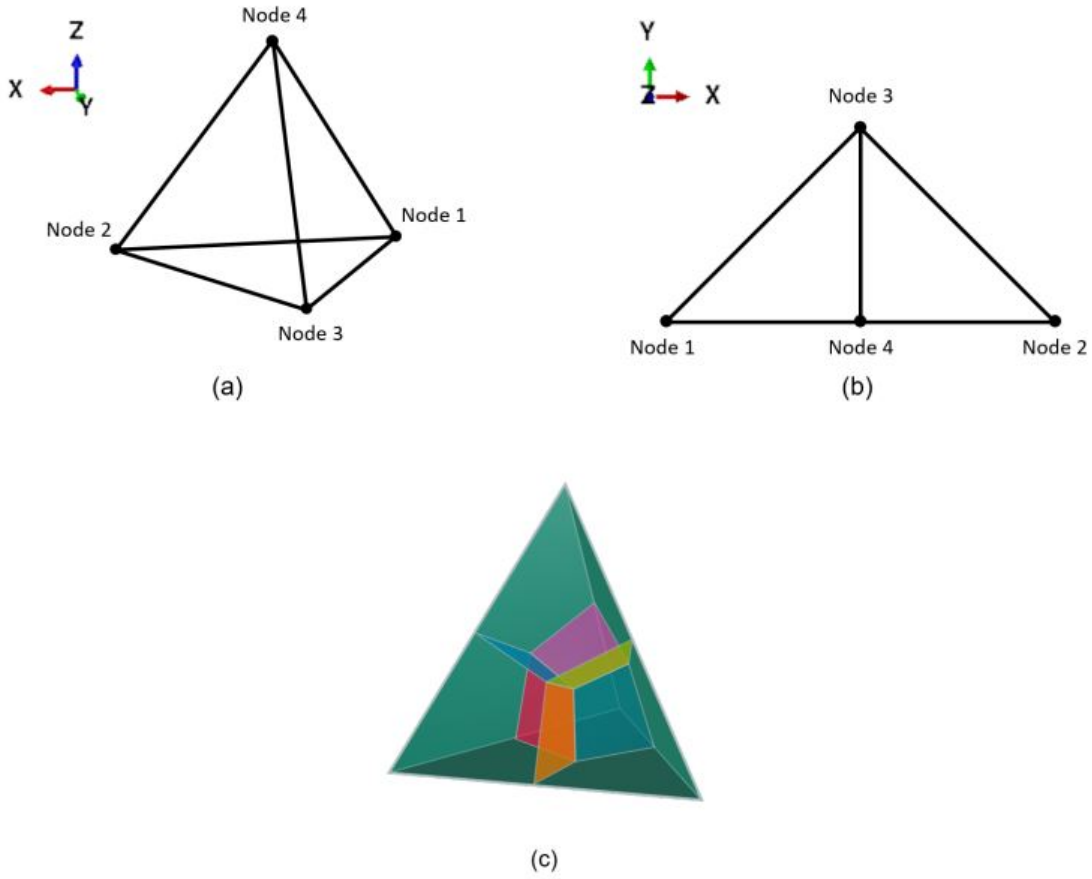

Figure 2.2: The initially-undeformed (a) three-dimensional view, and (b) plan view of the simulation domain used to perform the finite-element simulations. The element is meshed using one Abaqus C3D4 continuum three-dimensional tetrahedron element. The nodal coordinates for the tetrahedron element are listed in Table 2.1. (c) A three-dimensional visualization of the 6 possible fracture microplanes within a tetrahedron element.

Parameters	Y (GPa)	ν	ρ (kg/m^3)	$\dot{e}_o$ (/s)	I_o^c	G_0	c_o
Value	18	0.2	2400	3×10^{-6}	2×10^{-4}	2×10^{9}	0.057

Table 2.2: Baseline material parameters for concrete.

2.2.1 Fracture in a quasi-brittle material

Using the baseline material parameters listed in Table 2.2, monotonic simple tension simulations are performed with varying values of I_o^c and G_o, and plot the corresponding stress-strain responses in Figs. 2.3(a) and 2.3(b), respectively. The simulated stress-strain curves show similar trends which is typical of a quasi-brittle material: starting from the initial state of zero stress and zero strain, applied deformation will result in a (nominally) linear elastic stress-strain response until a peak stress value is attained. Further deformation beyond the peak stress level results in a strain-softening stress-strain response [72, 125]. From the simulated stress-strain curves shown in Fig. 2.3(a), it can be seen that the peak stress value is controlled by I_o^c where the peak stress value increases with increasing I_o^c. Furthermore, from Fig. 2.3(b), it can be ascertained that G_o controls the diffuseness of the transition from a linear elastic stress-strain response to a strain-softening stress-strain response once the deformation exceeds the critical applied strain to initiate the fracture process, e_c^a. Once the applied deformation exceeds e_c^a, increasing G_o yields in a sharper transition from a linear elastic stress-strain response to a strain-softening stress-strain response.

Next, the effect of element geometry on the fracture response can be studied by changing the location of the node located at the apex (that is, node 4) shown in Fig. 2.2. Figure 2.4 shows the monotonic simple tension stress-strain response with varying z-coordinate for the apex node of the tetrahedron element. Note that increasing the value for the z-coordinate of the apex node results in a lower value for the peak stress, and this is not surprising since an increasing value for apex node's z-coordinate results in the side edges of the tetrahedron element becoming more favorably oriented to the principal loading direction, and this in turn yields in a lower applied stress for fracture initiation, that is, the peak stress.

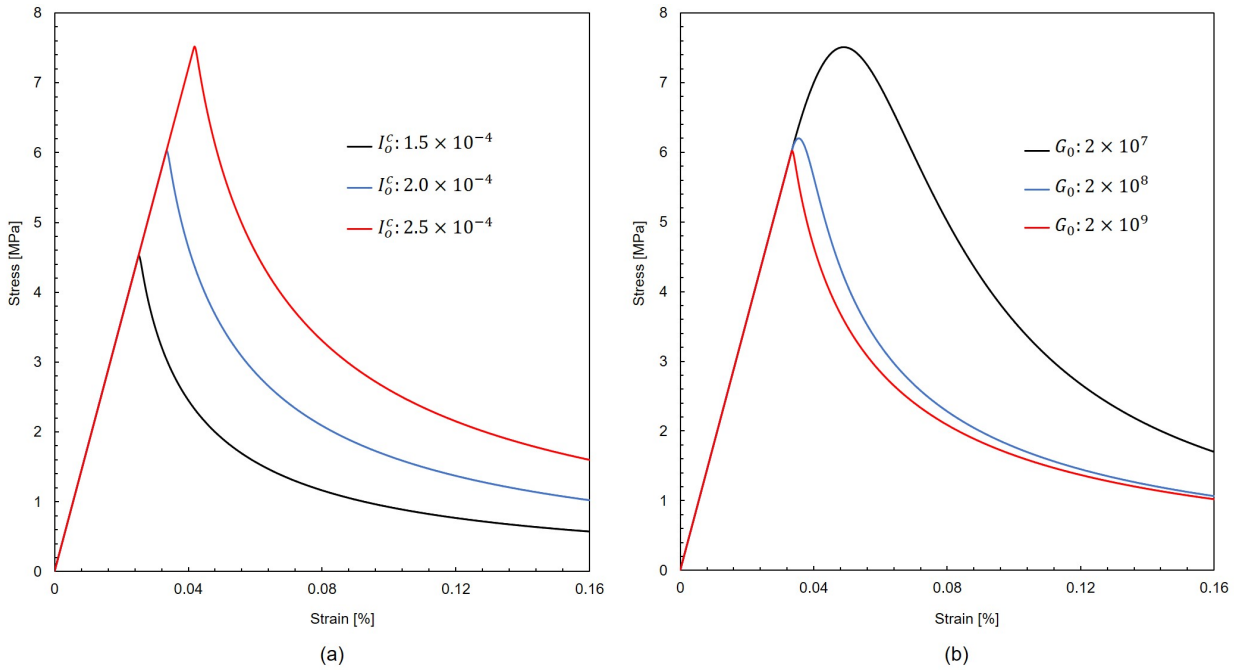

Figure 2.3: Monotonic simple tension stress-strain response, obtained from the FEM simulations using the simulation domain shown in Fig. 2.2. Using the baseline material parameters shown in Table 2.2, the effect of varying (a) I_o^c and (b) G_o on the stress-strain responses are displayed.

Following this, the simulations can use the baseline material parameters shown in Table 2.2, and model the crack closure response in a concrete by performing a simple tension/compression cyclic loading simulation. This is done by imposing the applied strain profile plotted in Fig. 2.5(a) on the simulation domain shown in Fig. 2.2 along with the imposed boundary and loading conditions on the element listed in Table 2.1. The corresponding stress-strain curve obtained from the applied strain profile shown in Fig. 2.5(a) is plotted in Fig. 2.5(b), and this simulated stress-strain response is qualitatively similar to that simulated by Miehe *et al.* [72]. For ease of comparison, the monotonic simple tension stress-strain response is also plotted using the baseline materials listed in Table 2.2 (see Fig. 2.3) in Fig. 2.5(b). The cyclic loading stress-strain response plotted in Fig. 2.5(b) can be described as follows: starting from an initially-uncracked state of zero stress and zero strain, an applied tensile strain to 0.045% results in a stress-strain response equal to that of the monotonic simple tension case (see the description in Section 3.1). At a tensile strain 0.045%, reverse loading to a strain of zero results in a reduction of stress to zero *but* with a reduction in ten-

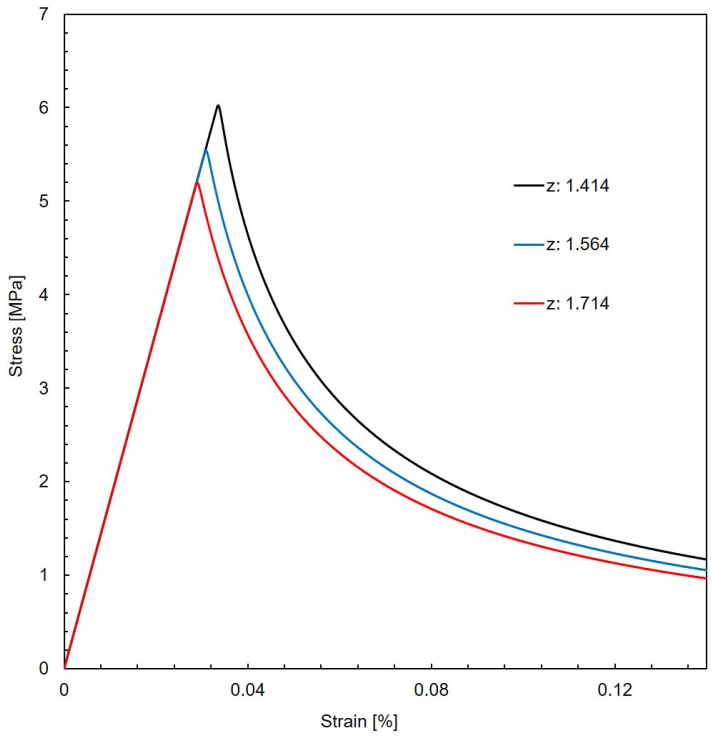

Figure 2.4: Monotonic simple tension stress-strain response, obtained from the FEM simulations using the simulation domain shown in Fig. 2.2. Using the baseline material parameters listed in Table 2.2, the effect of the geometry by varying the z-coordinate of the node located at the element's apex, on the stress-strain and fracture response is shown. Note that fracture is more easily initiated with increasing value of the element's z-coordinate since this results in the side edges of the tetrahedron becoming more favorably oriented with respect to the direction of applied deformation (that is, direction-Z.).

sile stiffness due to some degree of cracking in the material. However, further reverse loading from zero strain to a compressive strain of 0.064% results in a compressive stress-strain response of stiffness equal to that of the initially-uncracked material in tension. This indicates that a perfect crack closure response is obtained in simple compression even with some degree of cracking in material. By reversing the applied deformation from a compressive strain of 0.064% to a tensile strain of 5% results in a retracing of the stress-strain response due to the deformation from a tensile strain of 0.045% to a compressive strain of 0.064%. Continued deformation from a tensile strain of 0.045% to a tensile strain of 0.056% results in the strain-softening response which perfectly overlaps the stress-strain response obtained from the monotonic simple tension stress-strain response. The reverse loading from a tensile strain of 0.056% to zero strain results in an unloading stress-strain response with the tensile stiffness being further reduced due to further cracking in the material induced by the tensile deformation from an applied strain of 0.045% to 0.056%. Further reverse loading to a compressive strain of 0.064% again results in a compressive stress-strain response of stiffness equal to that of the initially-uncracked material in tension. This again indicates that perfect crack closure conditions are modeled in simple compression. The final stage of the cyclic loading profile involves a deformation from a compressive strain of 0.064% to a tensile strain of 0.16%. For this stage, the stress-strain response from a compressive strain of 0.064% to a tensile strain of 0.056% perfectly retraces the stress-strain response due to the previously-obtained deformation from a tensile strain of 0.056% to a compressive strain of 0.064%. However, a continued deformation from a tensile strain of 0.064% to a tensile strain of 0.16% results in further cracking in the material, and a stress-strain response which perfectly overlaps the monotonic simple tension stress-strain response. Therefore, from this FEM calculation, it can be concluded that crack closure can be perfectly simulated using our relatively-simple computational procedure where in compression, the material is able to regain its initially-uncracked stiffness.

The effect of applied strain-rate is also investigated on the simple tension deformation of the simulation domain shown in Fig. 2.2 by varying the applied strain-rate from 1×10^{-7}/s to 1×10^{-4}/s (which are typical applied strain-rates for investigating the quasi-static response of concrete, except

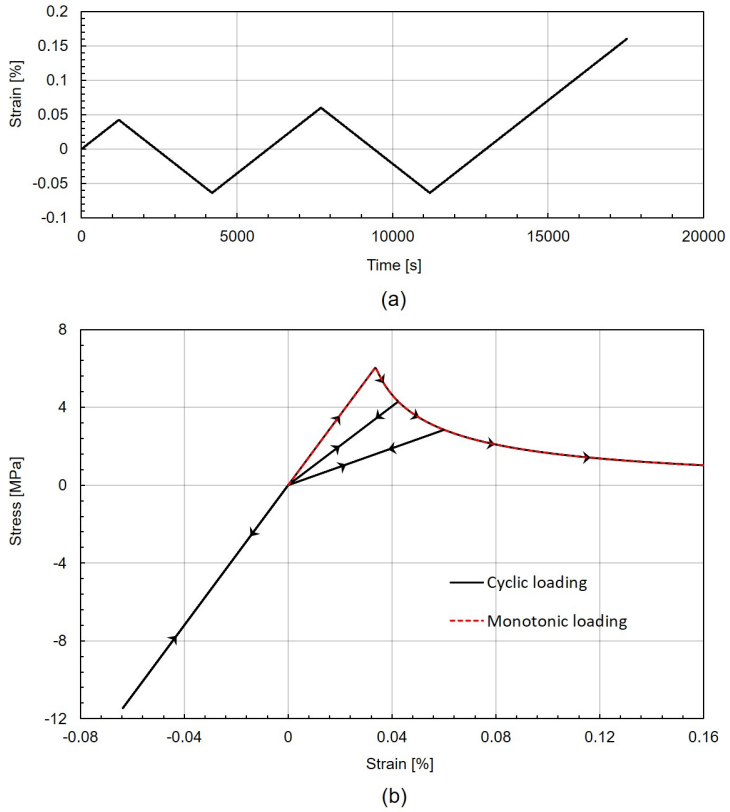

Figure 2.5: (a) The applied strain profile for the crack closure simulation for a concrete, and (b) its corresponding simple tension-compression cyclic loading stress-strain response. Note that a perfect crack closure response is obtained since the stiffness in compression is equal to the stiffness of the uncracked material in tension.

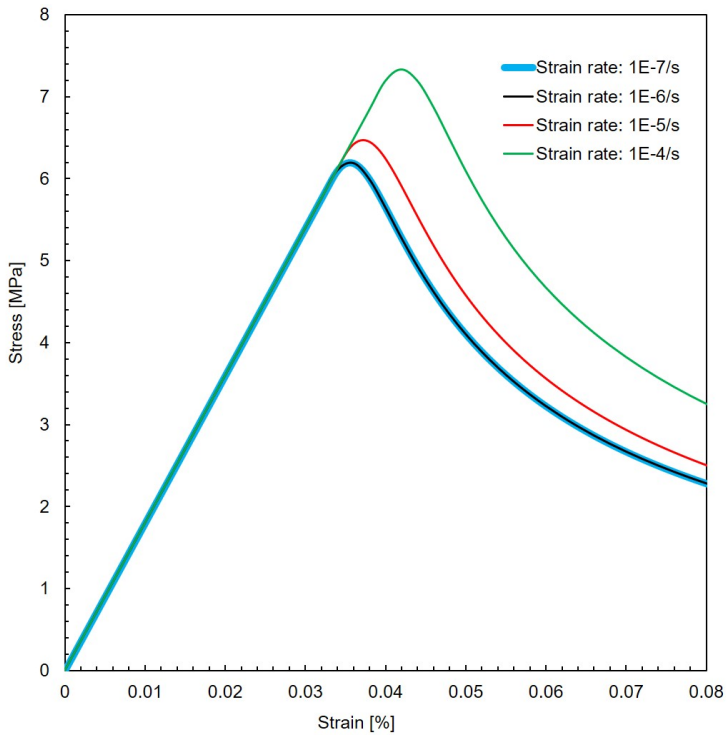

Figure 2.6: The monotonic simple tension stress-strain response under varying applied strain-rates. The stress required to sustain the cracking process in the material increases with increasing applied strain-rate beyond a critical applied strain-rate, below which the stress-strain response is insensitive to applied strain-rates.

for the strain rate 1×10^{-4}/s). The material parameters in Table 2.2 were used for the study but with $G_0 = 2 \times 10^8$. The corresponding stress-strain responses obtained from these applied strain-rates are plotted in Fig. 2.6. Note that the stress-strain response from the simulations performed under an applied strain-rate of 1×10^{-7}/s to 1×10^{-6}/s are identical, and as the applied strain-rates are increased, the peak stress levels also increase, indicating that the stress required to sustain the cracking in the material increases with increasing applied strain-rate beyond a critical applied strain-rate.

To further confirm the crack closure capability of the proposed method, a fully three-dimensional boundary value problem is simulated under cyclic shear deformation using the experimental specimen geometry proposed by Bazant and Prat [132]. The meshed configuration of the circumferentially notched cylinder specimen is shown in Fig. 2.7(a). The boundary and loading conditions

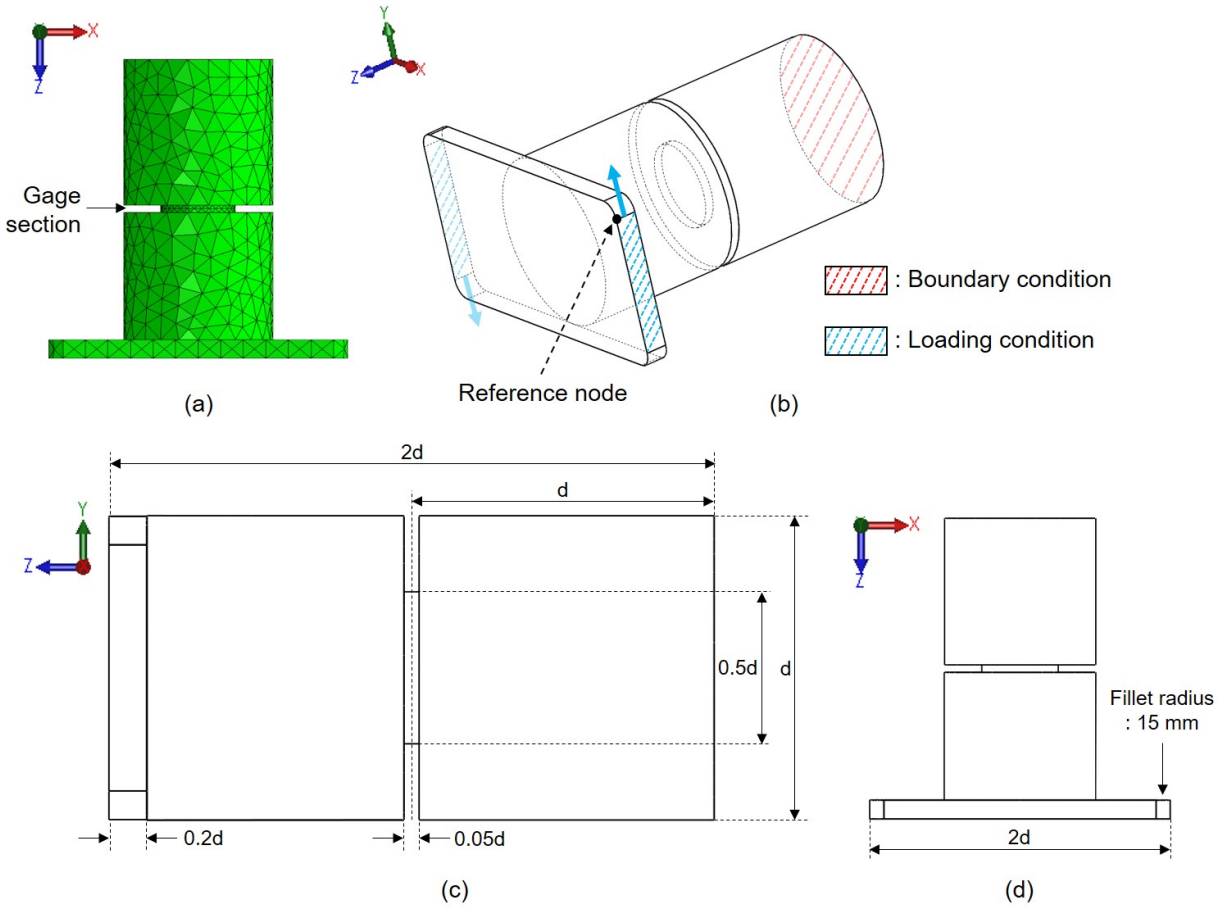

Figure 2.7: (a) The three-dimensional mesh configuration of the circumferentially-notched cylinder specimen used in the cyclic-shear simulation. The notched cylinder is meshed with the Abaqus C3D4 elements. (b) Boundary and loading conditions imposed on the sample shown in (a). These imposed conditions will result in the cracking of the specimen's gauge section. Plan view of the specimen along (c) X-axis, and (d) Y-axis of the notched cylinder specimen with $d = 160$ mm.

imposed on the specimen are shown in Fig. 2.7(b), where the Z = -d surface is imposed with the fixed boundary condition in all translational movement. The displacement profile in the Y axis is given as a loading condition on two surfaces, which are the X = -d surface and the X = d surface. The magnitude of the displacement profile given to the X = d surface is exactly equal to the magnitude of the displacement profile imposed to X = -d surface *except* that the displacement at the X = d surface is along the positive Y axis whereas the the displacement at the $X = -d$ surface is along the negative Y axis. This loading profile along with the imposed boundary conditions create a torque on the gauge section of the sample to induce cracking [see Fig. 2.7(b)]. Figs. 2.7(c) and 2.7(d) show the dimensions of the sample where diameter of the cylindrical specimen is d = 160 mm with the width of the circumferential notch being 8 mm and the round fillet at each corner of the loading plate having a radius of 15 mm.

For this simulation, the simulation uses the baseline material parameters presented in Table 2.2 *except* for $G_0 = 2 \times 10^8$. Fig. 2.8(a) shows the imposed deformation profile on the reference node of the sample shown in Fig. 2.7(b). The resulting force-displacement response from this cyclic shear deformation simulation is shown in Fig. 2.8(b) where the force and displacement data is obtained from the reference node [see Fig. 2.7(b)]. The cyclic loading force-displacement curve plotted in Fig. 2.8(b) can be described as follows: starting from an initially-undamaged state at zero force and zero displacement, a deformation from a displacement of 0 mm to 0.26 mm and back to 0 mm results in a *cracking* of the sample in the gauge section, as evidenced by the significant hysteresis in the force-displacement response, and also the reduced stiffness of the sample when the deformation is reversed from a displacement of 0.26 mm to 0 mm. Note that the hysteretic response is closed-loop. However, further reverse loading from zero displacement to a displacement of -0.05 mm shows the stiffness recovery of the damaged specimen to the initially-undamaged state of the sample. This indicates that a perfect crack closure response is obtained for the cyclic shear loading simulation. Hence, the presented numerical simulation shows the crack closure capability of our proposed method for a three-dimensional boundary value problem of importance.

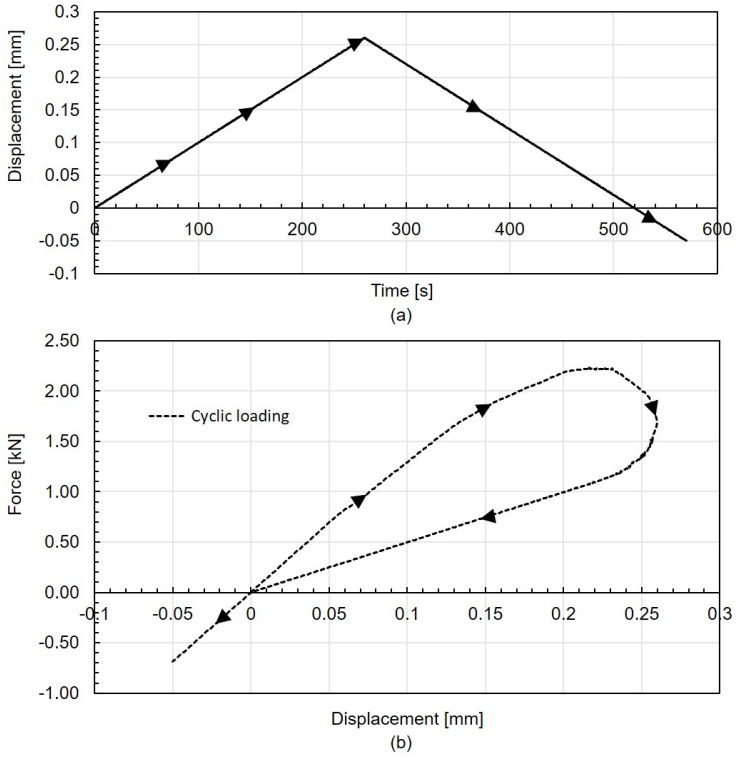

Figure 2.8: (a) The applied displacement profile for the three-dimensional cyclic shear simulation, and (b) its corresponding cyclic loading force-displacement response. The crack closure result in the cyclic shear loading-induced fracture case is confirmed by the stiffness recovery in the negative displacement regime.

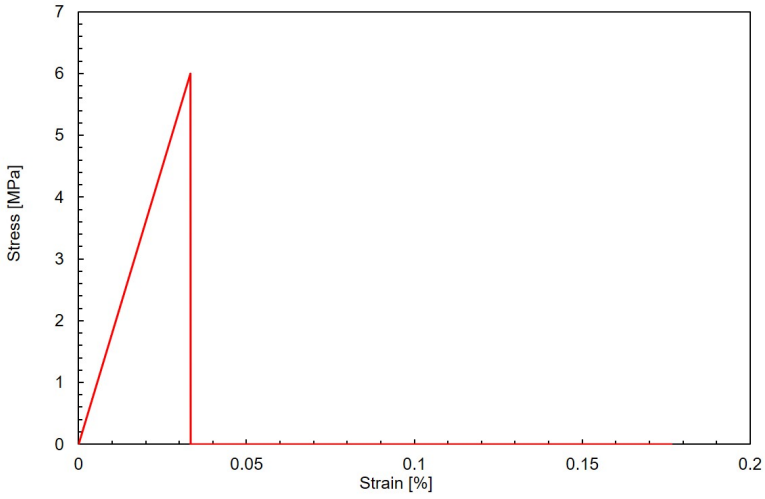

Figure 2.9: The monotonic simple tension stress-strain response for a brittle material. Note that deformation beyond the strain level at peak stress results in a precipitous drop in stress from the peak stress to zero stress, and the inability of the material to further sustain tensile stresses.

2.2.2 Fracture in brittle materials

It is important to note that our computational framework is also able to model brittle fracture since this case is a special case of quasi-brittle failure, that is, brittle fracture is modeled by setting $G_0 \to \infty$. In our FEM simulations, the simulations use the baseline material parameters listed in Table 2.2 but set $G_0 = 1 \times 10^{20}$ to mimic the conditions for brittle fracture. Using the element shown in Fig.2.2 along with the boundary and loading conditions listed in Table 2.1, a monotonic simple tension FEM simulation is performed and plot the corresponding stress-strain curve in Fig. 2.9. From this figure, it can be clearly seen that the theory and FEM implementation is able to model a brittle fracture response, namely deformation beyond the strain level at peak stress results in a precipitous drop in stress from the peak stress to zero stress, and the inability of the material to further sustain tensile stresses. This simulation result is qualitatively similar to that obtained by other researchers [133].

Finally, the cyclic tension-compression stress-strain response is simulated for a brittle elastic material to investigate the ability of our computational framework in modeling crack closure in brittle elastic materials using the baseline material parameters listed in Table 2.2 but with $G_0 = 1 \times 10^{20}$. The applied strain profile on the element shown in Fig. 2.2 for this simulation is plotted in Fig. 2.10(a), and it is the same profile as shown in Fig. 2.5(a). The corresponding stress-strain response obtained from this applied strain profile is displayed in Fig. 2.10(b). Starting from an initially-uncracked state at zero stress and zero strain, a tensile deformation to a strain of 0.045% results in an initially elastic stress-strain response, and a precipitous drop in tensile stress from a peak stress value to zero stress at a tensile strain of 0.032%. Once this “event" (or in actuality, a very fast process) occurs, the material will be further unable to bear tensile stresses. However, when the strain in the material is compressive, the material is able to fully-recover its initially-uncracked stiffness as evident by the stress-strain slope in compression [see Fig. 2.10(b)]. Therefore, our relatively-simple computational procedure is also able to simulate a perfect crack closure response for brittle elastic materials as well.

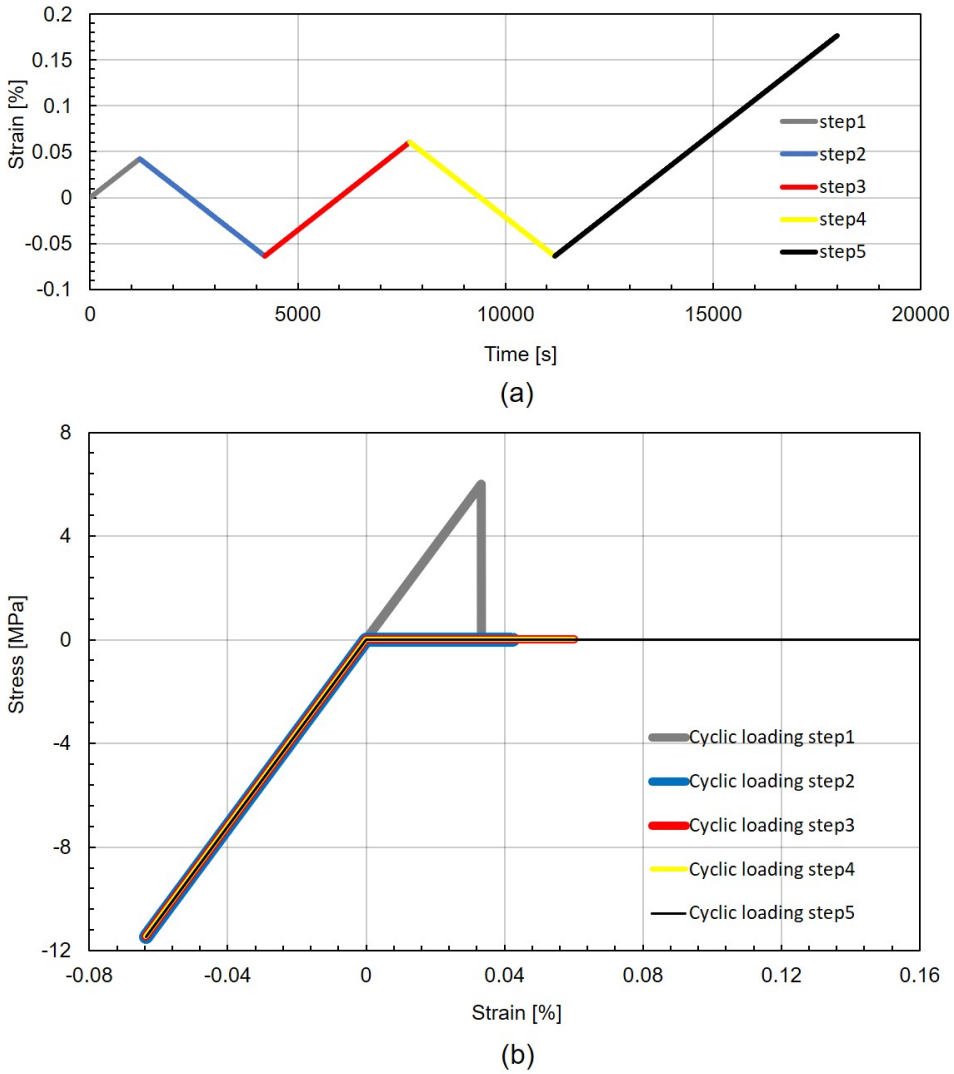

Figure 2.10: (a) The applied strain profile for the crack closure simulation for an elastic-brittle material, and (b) its corresponding simple tension-compression cyclic loading stress-strain response. Note that a perfect crack closure response is obtained since the stiffness in compression is equal to the stiffness of the uncracked material in tension. Furthermore, after the material experiences a load drop to zero stress during the first portion of applied tensile strain profile, it is further unable to bear tensile stresses.

3. TWO-DIMENSIONAL GRAFEA SIMULATION VALIDATION: DROP WEIGHT IMPACT EXPERIMENTS[1]

High-strength (or performance) concrete (HSC) is one of the most commonly used materials for building structures such as offshore platforms, nuclear power plants, highway bridges, high-rise buildings *etc.* [134–136]. When deployed, these structures can be exposed to high intensity short duration time dependent loads due to impact, explosion or earthquake during their service life. This can potentially result in the catastrophic fracture of such structures. Hence, it is imperative for any developed computational framework for modeling quasi-brittle response to be able to *ascertain* and *quantity* the effect of dynamics and loading rates on the fracture properties of HSC.

Therefore, the following objectives are set for this section: (a) to verify the GraFEA approach for modeling fracture in HSC at deformation rates higher than quasi-static conditions, (b) to ascertain if the calibration of material parameters using low-strain-rate experimental data allows the satisfactory prediction for the macroscopic response *e.g.* cracking profile, load-time (impulse) responses *etc.* of HSC fracture under impact conditions, and (c) to independently validate experimental crack propagation speed data obtained from the impact of HSC samples.

The highlights of this chapter are:

- With the material parameters calibrated using a quasi-static experimental data, the GraFEA model is able to accurately predict the load-time impulse data obtained from impact experiments;
- The experimental crack speed data measured from impact experiments are also matched to good accord using material parameters calibrated from quasi-static experimental data.

[1]Reprinted from the original reference of "On simulating impact fracture in high-strength concrete using GraFEA" by H.Y. Shin, P. Thamburaja, A.R. Srinivasa and J.N. Reddy, 2022. *Extreme Mechanics Letters*, 52, 101618.

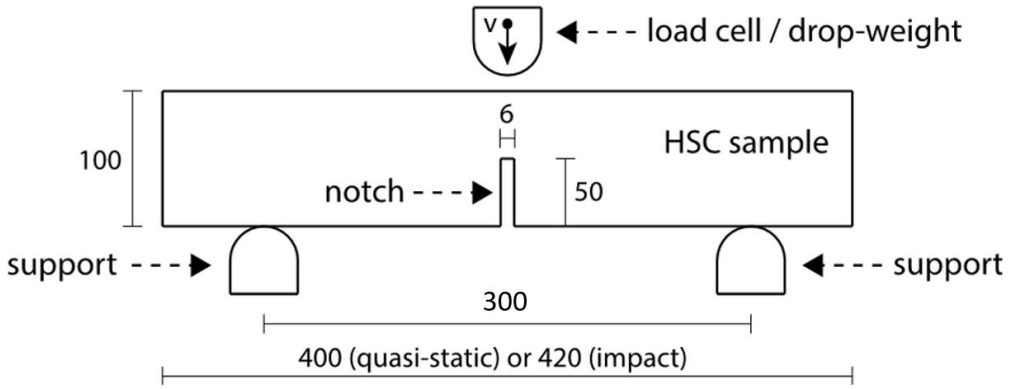

Figure 3.1: Set-up for the three-point bending experiments conducted on a HSC sample [137,141]. For quasi-static experiments, a velocity profile, v is imposed on the load cell to deform the sample [141]. For the impact experiments, a drop-weight experiment at different heights were conducted resulting in different initial impact velocities, v on the HSC sample [137]. All dimensions are in mm. The notch width is inferred to be 6 mm.

3.1 Quasi-static response: calibration of material parameters

The elastic response of the fully-intact material is assumed to be isotropic and hence can be quantified by the Young's modulus Y and the Poisson's ratio ν.

An outline of the procedure for determining the material parameters in the model is following, that is, $\{ Y , \nu , r_\phi , G_o , \epsilon_o^c , \dot{\epsilon}_o , c_o , \rho \}$. The HSC has a material density of $\rho = 2368$ kg/m^3 [137]. The Poisson's ratio is taken as ν = 0.2 [138]. Furthermore, the maximum aggregate size (or diameter) in the HSC is between 6 mm to 12 mm [139]. Hence, following the procedure of [140], the simulation takes the intrinsic material length-scale $r_\phi = 4.5$ mm. Finally, since there is a paucity of experiments conducted on the HSC of Zhang *et al.* [141] at various strain-rates in the quasi-static regime, it was not possible to calibrate the material parameters $\dot{\epsilon}_o$ and c_o for HSC. Therefore, as a first-cut assumption, the parameters are set as $\dot{\epsilon}_o = 3 \times 10^{-6}$/s and $c_o = 0.055$ [140].

The remaining material constants $\{Y, G_o, \epsilon_o^c\}$ are fit to a macroscopic force-displacement ($P - \Delta$) data obtained from a (symmetric) three-point bend experiment conducted under quasi-static conditions [141]. Fig. 3.1 shows the set-up for the three-point bending experiments conducted on HSC [137, 141]. The experimental program for the quasi-static and impact experiments are

described in the caption of Fig. 3.1.

The quantification of the quasi-static and impact experimental response is conducted using FEM simulations. In our ABAQUS/Explicit [131] FEM simulations, mesh for the HSC sample is generated as shown in Fig. 3.1 using constant-strain continuum triangular elements, and all FEM simulations are conducted using a set of 3 random crack plane orientations assigned to each Gauss point of the continuum elements used to mesh the HSC sample, that is, $K = 3$. To ensure mesh-independent $P - \Delta$ responses, it is ensured that there are at least 4 elements spanning the diameter of the ZOI [140] at Gauss points in the region where cracks are expected to form. The load cell/drop weight and supports are modeled as analytical rigid surfaces which is available in Abaqus. The impact simulations impose a mass of 120.6 kg for the drop-weight [137], and the impact force is taken to be equal to the absolute-value of the mass of the drop-weight $\times$ the deceleration of the drop-weight as impact occurs. Finally, all the FEM simulations were conducted under a *plane stress* condition, and the effect of friction has also been ignored in the numerical simulations.

Fig. 3.2 shows the $P - \Delta$ response obtained from the quasi-static symmetric three-point bend experiment of Zhang *et al.* [141]. For this experiment, the load cell moves at a constant speed of 5.5×10^{-4} mm/s (Experiment 1). The material parameters are decided by following the fitting procedure. The initial response is used to fit the Young's modulus, Y, the transient response is used to calibrate the strain softening rate, G_o, and the steady-state response is used to fit the rate-independent threshold strain, ϵ_o^c. A FEM simulation[2] is conducted using half of the HSC sample shown in Fig. 3.1 (due to symmetry of the sample geometry and boundary/loading conditions), and compare the fit of the $P - \Delta$ response obtained from this FEM simulation (Simulation 1) to the $P - \Delta$ response determined from Experiment 1, in Fig. 3.3. The FEM simulated $P - \Delta$ response fits the $P - \Delta$ experimental data obtained from Experiment 1 to good accord, and the list of material parameters used to conduct the fit are shown in Table 3.1.

The inset of Fig. 3.3 also shows the FEM determined survival probability contours in the HSC sample, obtained at the completion of Simulation 1. As expected, the crack forms in the sample's

[2]The FEM simulation conducted in the quasi-static regime was sped up using the mass scaling option in ABAQUS/Explicit [131] while still ensuring quasi-static conditions prevail during the FEM simulation.

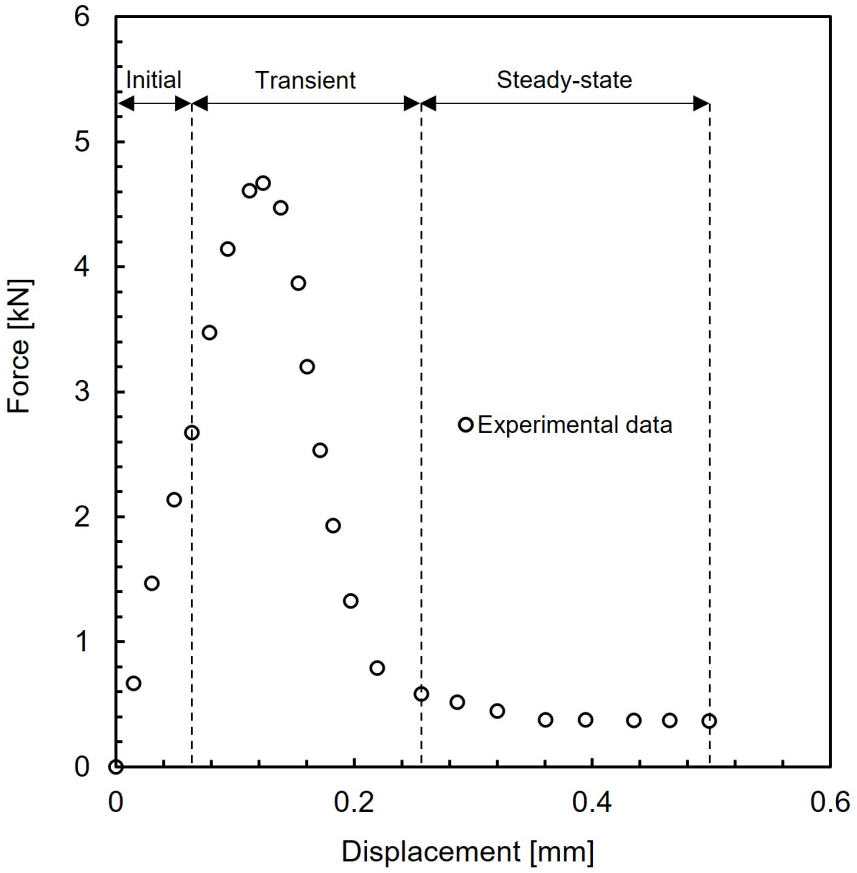

Figure 3.2: A quasi-static force-displacement experimental response of a HSC beam under symmetric three-point bending loading [141]. The initial response is used to fit the Young's modulus, Y, the transient response is used to calibrate the strain softening rate, G_o, and the steady-state response is used to fit the rate-independent threshold strain, ϵ_o^c.

plane of symmetry as seen in experiments [28, 141, 142]. Therefore, the material parameters in the constitutive model are successfully calibrated.

3.2 Impact response: independent verification

Using the list of calibrated material parameters (see Table 3.1), simulations are conducted to independently verify experimental data obtained from impact experiments. Fig. 3.4 shows the *mean* impact load-time (I-T) data obtained from the experiments of Zhang *et al.* [137], with an initial impact speed of 8.81×10^2 mm/s (Experiment 2), 1.76×10^3 mm/s (Experiment 3) and 2.64×10^3 mm/s (Experiment 4). Although the experimental I-T data plotted in Zhang *et al.* [137] (which

Table 3.1: Material constants for HSC [137, 141]

$Y = 18$ GPa	$\nu = 0.2$	$\epsilon_o^c = 1.3 \times 10^{-4}$	$G_o = 450$
$r_\phi = 4.5$ mm	$\dot{\epsilon}_o = 3 \times 10^{-6}$/s	$c_o = 0.055$	$\rho = 2368$ kg/m^3

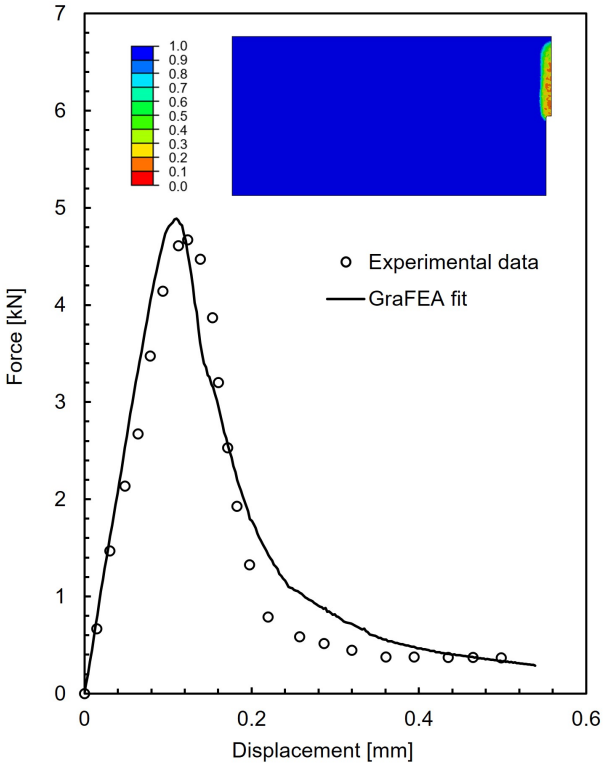

Figure 3.3: The experimentally-determined force-displacement ($P - \Delta$) response from a quasi-static symmetric three-point bending experiment [141]. The load cell is imposed loading speed of 5.5×10^{-4} mm/s. The FEM simulated $P - \Delta$ response conducted at a loading speed of 5.5×10^{-4} mm/s is also shown. The experimental $P - \Delta$ data is accurately fit by the $P - \Delta$ output from the FEM simulation. Shown inset of the figure is the FEM simulated cracking pattern in the half-sample, obtained at the completion of the simulation. The experimentally-determined cracking pattern [28, 141, 142] is also well-reproduced by the FEM simulation.

is displayed in Fig. 3.4) only showed the mean response, it must be emphasized that scatter in the experimental results is inherent in impact tests on concrete as mentioned in Banthia *et al.* [143]. Furthermore, it is also important to note that the experimental results shown in Fig. 3.4 are the time-shifted [3] or corrected experimental data.

[3] A strategy of shifting the experimental I-T responses is conducted along the time axis by projecting the initial slope of the experimental signal to the zero load line, and taking the intercept to represent the commencement of

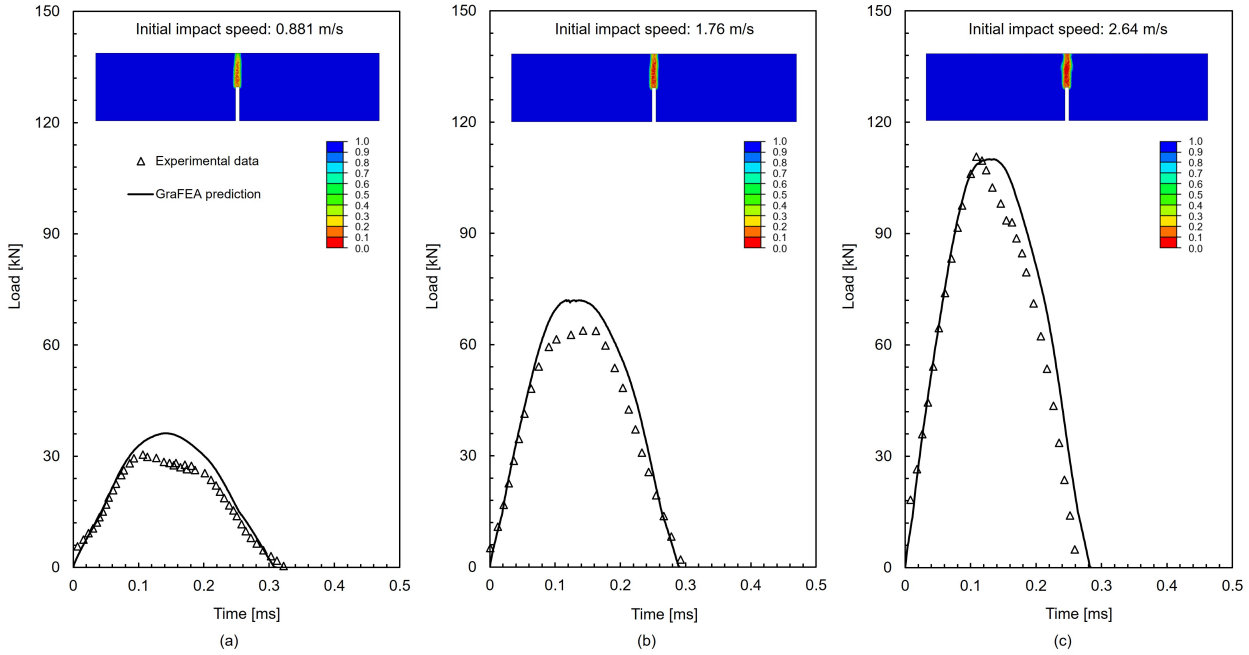

Figure 3.4: The raw experimental impact load-time (I-T) data obtained from Zhang et al. [137] for an initial drop-weight impact speed of (a) 0.881×10^3 mm/s, (b) 1.76×10^3 mm/s, and (c) 2.64×10^3 mm/s. The prediction from the GraFEA FEM simulation for each case is also plotted, and the experimental I-T responses are well-predicted by the FEM simulations once a time-shift is applied to the raw data. The simulated cracked pattern in the HSC sample for each initial impact speed, obtained at the completion of each simulation, is also shown inset of each figure, and these predictions match the experimentally-determined cracking pattern in the sample (see Fig. 1 of [137]).

Two major trends can be noticed from the impact experimental data: (a) the peak impact load increases with increasing initial impact speed, and (b) the peak loads observed in the impact experiments are an order magnitude larger than the peak loads observed in the quasi-static experiments *cf.* Fig. 3.3 vs. Fig. 3.4.

Then FEM simulations of the impact experiments are performed with the drop-weight imparted with an initial speed of 8.81×10^2 mm/s (Simulation 2), 1.76×10^3 mm/s (Simulation 3) and 2.64×10^3 mm/s (Simulation 4) using the material parameters listed in Table 1. The resulting I-T response obtained from each impact FEM simulation are also plotted in Fig. 3.4. From this figure, it can be seen that the FEM simulations are able to independently quantify the (a) peak

"actual" loading.

impact loads, and (b) width of the I-T responses (measured along the time axis), to good accord. In particular, the FEM simulations are able to: (i) predict the increasing peak impact load with increasing initial impact speed, and (ii) predict the experimentally-determined cracking pattern in the HSC sample under impact conditions (compare the contour plots shown inset of Figs. 3.4(a)-(c) to Fig. 1 of Zhang *et al.* [137]).

To summarize, using the results plotted in Fig. 3.4, it can be ascertained that the model has successfully predicted the response from impact experiments ($\sim$1m/s) conducted at loading rates that are 6 to 7 orders of magnitude higher than the loading rate used for calibrating the material parameters ($\sim 1 \times 10^{-7}$m/s). Our next task is to compare the FEM-simulated crack propagation speeds in the HSC sample under impact loading to experimental data.

3.3 Prediction of crack propagation speeds in impact experiments

In the experiments of Zhang *et al.* [137] conducted under different impact speeds (see Fig. 3.4), crack propagation speeds at different positions in the HSC beam were measured using four strain gauges (SGs) placed at various positions in the notched beam [see Fig. 3.5(a)], and the experimental data are plotted in Fig. 3.5(b). The crack propagation speed at locations in the mesh of the HSC beam corresponding to the locations of the attached SGs in the sample, obtained from the FEM simulations conducted under different initial impact speeds (see Sec. 3.2), are also plotted in Fig. 3.5(b).

Before proceeding further, it is crucial to describe the method for determining the crack speeds from our FEM simulations: in the simulations, the strain profile data is sampled in each element at a very large rate. Next, the *area-averaged* strain profile is calculated for the elements located in the region occupied by each strain gauge in the HSC sample. As described in Zhang *et al.* [137], each strain gauge has dimensions of 6 mm (measured along the x-axis) by 2.8 mm (measured along the y-axis). It is assumed that the area-averaged strain profile data for each region is the area-averaged strain profile data at the centroid of each respective strain gauge. Upon obtaining the raw area-averaged strain profile data at each strain gauge centroid, the data is post-processed with a Python script to smoothen the area-averaged strain profile response using a least-squares approach. From

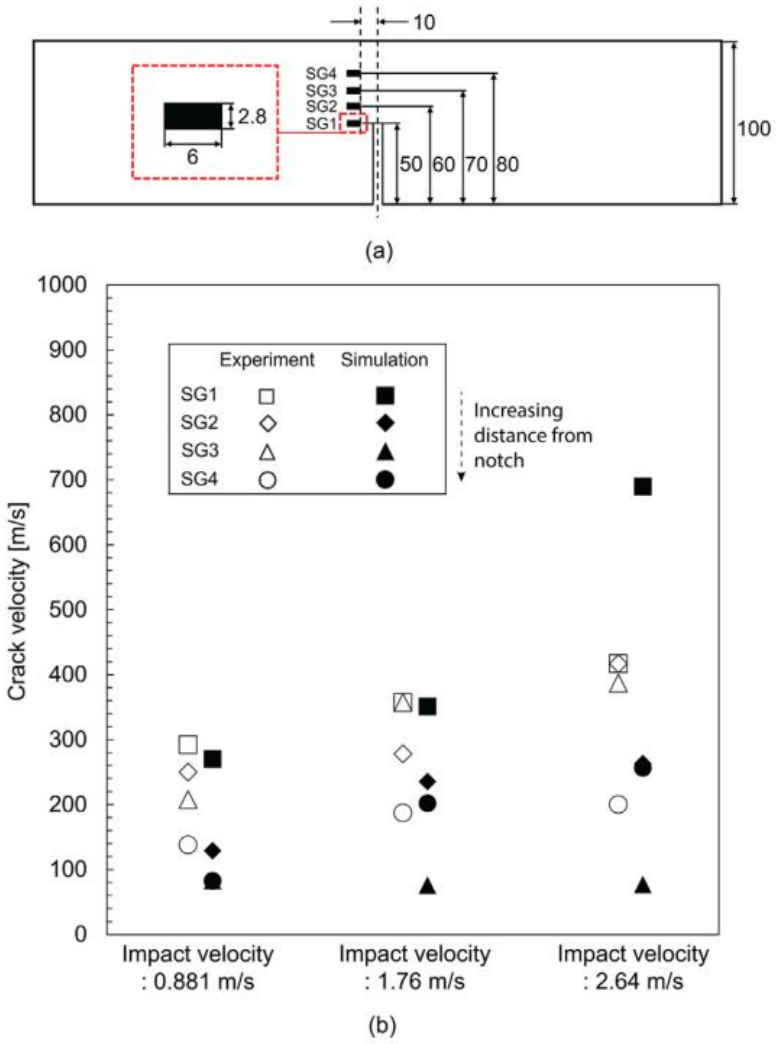

Figure 3.5: (a) The location for the strain gauges (SGs) used to measure crack speeds in the impact experiments of Zhang *et al.* [137] conducted on notched high-strength concrete (HSC) samples. All dimensions are in mm. (b) The experimentally-determined crack propagation speeds in the impact experiments of Zhang *et al.* [137], obtained at different strain gauge locations for various initial drop-weight impact velocities. The corresponding FEM-determined crack propagation speeds obtained from the GraFEA impact simulations are also plotted with respect to experimental data, and the overall comparison between the experimental & simulation data are reasonable. The Rayleigh wave speed for the material, $v_r \approx 1600$ m/s.

the smoothened area-averaged strain data profile at each strain gauge centroid, the exact times are determined when peaks and inflection points occur, and then the crack speeds are calculated at each strain gauge using the procedure outlined by Zhang *et al.* [137].

By comparing the experimental and simulated data shown in Fig. 3.5(b), it can be ascertained that the experimental crack propagation speeds are reasonably well-validated by the FEM simulations.

Finally, it is also important to compare the simulated crack propagation speeds to the Rayleigh wave speed, v_r. The Rayleigh wave speed is calculated by [137]:

$$v_r = v_s \frac{0.862 + 1.14\nu}{1 + \nu} \tag{3.1}$$

where v_s is the shear wave speed. Using the value for the Young's modulus and Poisson's ratio calibrated in Table 3.1, the Rayleigh wave speed is determined for the material to be $v_r \approx 1.6$ km/s. Therefore, from the results shown in Fig. 3.5(b), it can be clearly seen that the FEM simulated crack propagation speeds are well-below the Rayleigh wave speed.

4. FRACTURE LENGTH SCALE CONTROLLED QUASI-BRITTLE MATERIAL EXPERIMENTS[1]

Although the previously listed experiments show characteristics of concrete damage behavior, limitations exist to study the physical phenomenon of fracture in quasi-brittle solids in a conventional laboratory setting. Since concrete samples have a wide range distribution of the aggregate size from fine to coarse, it is hard to find a clear insight of the material intrinsic length scale of fracture. Also, a relatively large coarse aggregate size makes it difficult to design a controlled experiment using smaller sample sizes. The concrete samples which are to be tested in a laboratory need to be large enough to have a statistical representation of the actual structure in deployment in order to obtain a smooth enough response at the continuum level of interest. Therefore, due to the requirement of large sample sizes, the experimental set-ups for the concrete fracture test, either quasi-static or impact testing, are required to have high-capacity load cells and relatively large-scale testing facilities [23, 29, 144]. This is particularly true for the experimental characterization of impact loads (for example, as done through a hammer drop test experimental set-up) where the experienced impact loads can exceed hundreds of kNs [145]. Hence, the requirement of a large capacity experimental set-up prevents conventional laboratories from performing a large number of detailed experiments for characterizing the impact fracture of concrete structures under various loading rates.

To overcome the limitations of performing impact experiments on concrete samples using conventional laboratory Universal Testing machines, laboratory-scale tests with a gypsum-based composite material (or Plaster of Paris) are proposed in this study to obtain insight on concrete fracture due to the similar nature of behavior, that is, these materials have a quasi-brittle response [146]. Since the fracture process zone of quasi-brittle materials is influenced by the size of the aggregates in the material [38,147], a single type of coarse aggregate within a narrow size range is mixed in the

[1]Reprinted from the original reference of "Modeling impact fracture in a quasi-brittle solids using a 3D nonlocal graph-based finite element analysis: Theory, finite element simulations, and experimental verification" by H.Y. Shin, P. Thamburaja, A.R. Srinivasa and J.N. Reddy, 2023. *Journal of the Mechanics and Physics of Solids*, 170, 105097.

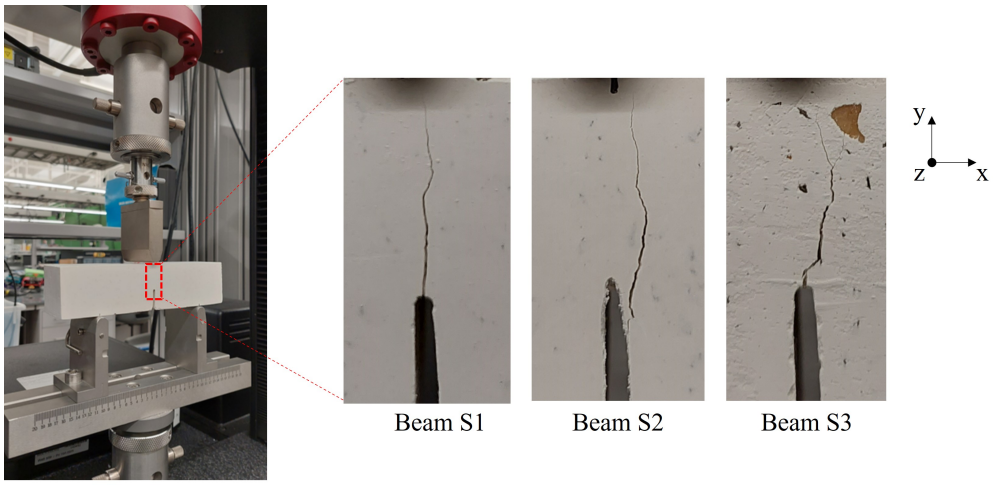

Figure 4.1: (a) Experimental set-up of the three-point bending test with the gypsum-based composite material, and (b) the crack propagation path of the notched beam samples. The crack path generally follows the middle plane of the beam samples, but it deviates and bifurcates due to the presence of aggregates.

gypsum-based composite material to better control the intrinsic material length scale which governs the fracture process. To perform the impact experiments, a simple ball drop impact test set-up is designed to give low-velocity impact on the Plaster of Paris samples, which generates a clear crack propagation path in a smaller size sample compared to that of concrete sampled. The results from the conducted experiments are then used in the validation process of the three-dimensional nonlocal GraFEA simulations.

4.1 Specimen preparation

In this section, the experimental approach is described for characterizing the deformation and fracture response a quasi-brittle solid made out of a gypsum-based composite material commonly known as Plaster of Paris. The advantage of this material is that it is able to have a controlled size single type of aggregate in the experimental test samples in order to have a clear insight into the effective intrinsic material length scale on the fracture response. A more detailed experimental program which explores the effect of aggregate size on the intrinsic fracture length scale will be pursued in our future works.

Three-point bending tests and ball drop tests are conducted with relatively small size samples to find out the material characteristics and damage behavior of the gypsum-based composite material. The procedure of the validation is similar to the two-dimensional concrete beam impact test case, where the material parameters are fitted based on the force-displacement curves obtained from the quasi-static loading conditions and the fitted material parameters are used in predicting impact damage behavior [148]. Through the validation process, the capability of the three-dimensionally oriented microcracks on predicting crack propagation in the three-dimensional domain can be fully revealed.

The dried calcium sulfate (gypsum powder) is mixed with the controlled size silica aggregates (diameters in the range of 3-5 mm) to make the plaster/aggregate heterogeneous material. The gypsum powder is provided by DAP Global Inc. (Baltimore, MD, U.S.A) with the name Plaster of Paris. The chemical composition of the product is following: Dried calcium sulfate 60-80wt%, Limestone 10-30wt%, and Quartz 0.5-1.5wt%. The weight ratio of water to the plaster powder (w/p) is chosen as 0.6 to match the w/p of the construction plaster sample [149, 150]. The weight ratio of the aggregates to the plaster powder is chosen as 1.0. The component mixing process starts with a dry mix of the plaster powder and the aggregates in a large bowl. Following this, the mixed grains are slowly poured and mixed in a water bowl to make a plaster/aggregate mixture. The mixture is then poured into the mold in a predetermined shape to make the desired samples. After the demolding, the samples are placed on the flat surface and dried for 7 days under a temperature of 23 ± 2°C and an air relative humidity of around $50 \pm 5\%$ [151].

4.2 Three-point bending test

A notched Plaster of Paris beam sample is used in the symmetrical three-point bending test. The experimental set-up of the three-point bending test appears in Fig. 4.1(a). The configuration and dimensional information of the notched beam appears in Fig. 4.2. A hammer is used to load the sample at the top surface of the sample, and the hammer lies directly above the notch. Furthermore, the notch is symmetrically-placed between the bottom supports of the beam. The dimension of the beam is given as (length $\times$ width $\times$ depth $= 160 \times 40 \times 40$ mm^3), with a notch width of 2 mm and

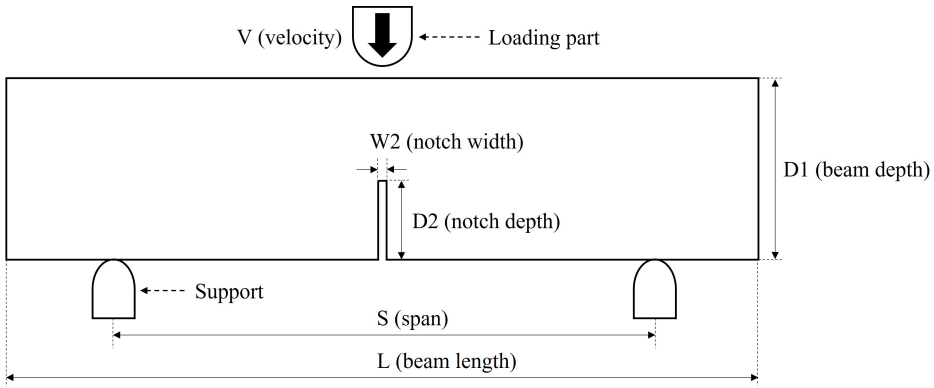

Figure 4.2: Experimental set-up for the three-point bending test. For quasi-static loading conditions, a velocity profile of the loading part is imposed with a specific velocity. The velocity of the impact loading conditions is controlled by changing the drop height of the loading part to achieve the desired velocity. The dimension of the plaster beam is (length $\times$ width $\times$ depth $= 160 \times 40 \times 40$ mm^3) with 100 mm of clear span. The width and depth of the notch are 2 mm and 20 mm. The concrete beam has dimension of (length $\times$ width $\times$ depth $= 420 \times 100 \times 100$ mm^3) with 300 mm of clear span. The width and depth of the notch are 6 mm and 50 mm.

notch depth of 20 mm. The beam span for the test is set as 100 mm, that is, the distance between the two bottom supports of the beam is 100 mm. A 68TM-10 INSTRON universal testing system is used for the bending test with a load cell of 10 kN capacity. For the quasi-static experiments, a loading rate of 5.5×10^{-4} mm/s is used, and the experiments are stopped once the samples are fully-fractured. The crack propagation path of each beam sample at the end of the tests appears in Fig. 4.1(b). Due to the presence of coarse aggregates in the sample, a deviation of the crack path from the center plane and bifurcation of the crack can be found in the crack path images [142]. Furthermore, from the generated crack surface for each sample shown in Fig. 4.3(a), the dispersed aggregates can be seen within the test samples.

4.3 Ball drop impact test

An impact testing set-up and geometry of the gypsum composite sample are designed to conduct ball drop tests to generate out-of-plane damage propagation. Disc samples are made with the gypsum composite having a diameter of 100 mm and a thickness of 10 mm. It should be noted that these sample sizes are much smaller than the concrete sample size considered at the low-speed impact tests [144, 152].

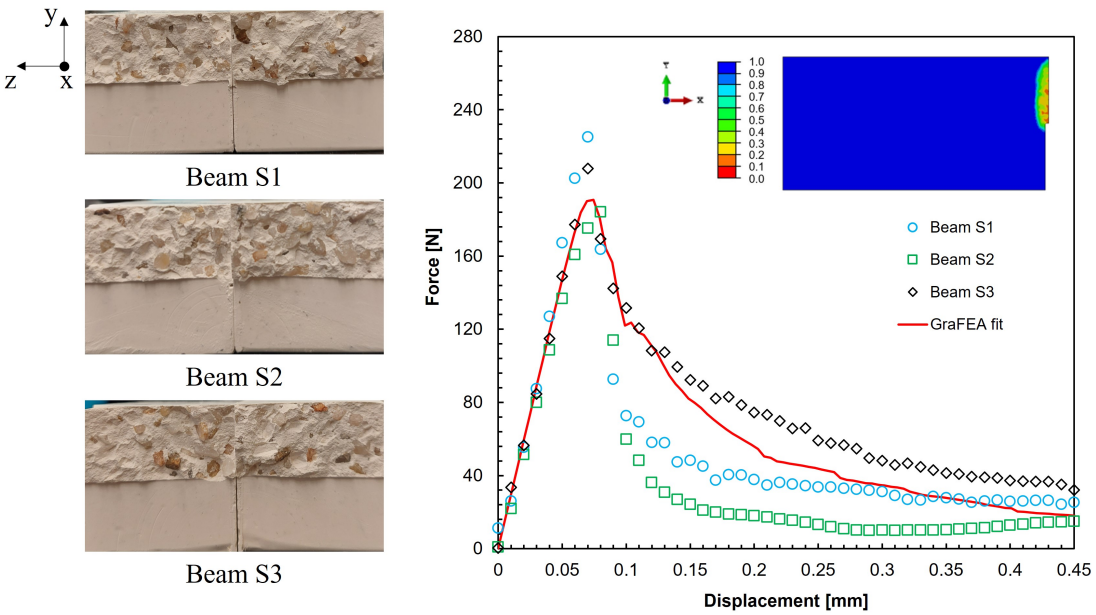

(a) (b)

Figure 4.3: (a) Generated crack surface on each beam sample from the three-point bending test. The beam sample is fractured into two pieces after the test and the images show generated surfaces from the fracture. The crack surfaces show the dispersed aggregates in the beam samples. (b) Force-displacement curves from the raw experimental data and the fitted two-dimensional GraFEA simulation. The quasi-static loading condition is imposed at the load cell with a velocity of 5.5×10^{-4} mm/s. The inset figure shows the contour plot of the average survival probability at the material point of each element. The cracking pattern obtained from the half-beam sample simulation matches well with the experimental data [145]. The peak loads of the experimental results range from 172 N to 228 N and the steady-state responses appear from 15 N to 32 N. It is important to emphasize that although the material composition is the same for the beam samples (S1-S3), the force-displacement curves show a scattered response which is typical of quasi-brittle solids such as concrete [142].

The configuration of the testing set-up appears in Fig. 4.4(a). A steel ball with a mass of 0.5 kg is dropped at a certain height to apply impact force on the disc sample. The guide tube and stand are used to make the ball drops in a straight line. An impact force is applied at the center of the disc sample to generate crack paths. At the current work, the ball is dropped from the height of 182 mm to make an impact velocity of 1.89×10^3 mm/s at the top surface of the plaster disc sample. Below the plaster disc sample, a steel ring is placed to make a gap region between the plaster sample and the steel disc to prevent the crushing of the sample. A sensor is placed below the center of the steel

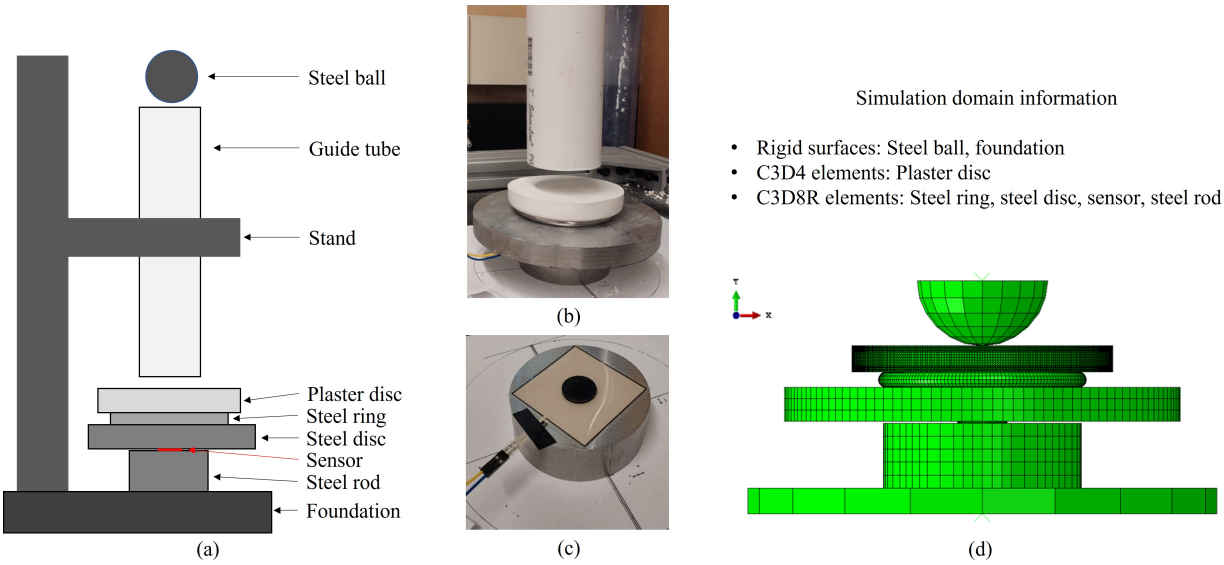

Figure 4.4: (a) The configuration of the ball drop testing set-up for low-speed impact loading conditions. The steel ball drops at a specific height to achieve the desired impact velocity. The actual image of the set-up appears in (b) multiple supports for the sensor system, and (c) pressure sensing sensor. (d) Simulation domain for the ball drop test. Each part of the domain is discretized with either deformable elements or rigid surfaces. Each C3D4 element is a tetrahedral element.

disc. A steel rod is positioned on top of the foundation as a base support for the sensor. Actual images of the drop test set-up appear in Fig. 4.4(b) and Fig. 4.4(c). An A502 Flexiforce sensor from Tekscan Inc. (Boston, MA, U.S.A) is used as a sensor for the testing set-up, where the sensor changes the resistance according to the applied pressure. An inverting operational amplifier circuit is constructed with an LF356N linear amplifier from Texas Instruments (Dallas, TX, U.S.A) to measure the voltage output according to the change in the sensor's resistance due to the applied impact force. The electric circuit diagram for the impact testing is shown in Fig. 4.5(a). An input voltage to the electric circuit is set as V_{in}=-0.5 V, which is following the range given by the sensor manual. The reference resistance is set as RF1 =10 kΩ and the output voltage from the circuit is measured based on the equation shown in the figure. By using the constructed sensor circuit, a 3-point calibration method is used to obtain a force-voltage relationship. Fig. 4.5(b) shows the voltage outputs from static loads given by steel plates. One steel plate weighs 22.0725 N and three points for the calibration are chosen as follows: 0 N from 0 steel plate, 22.0725 N from one steel

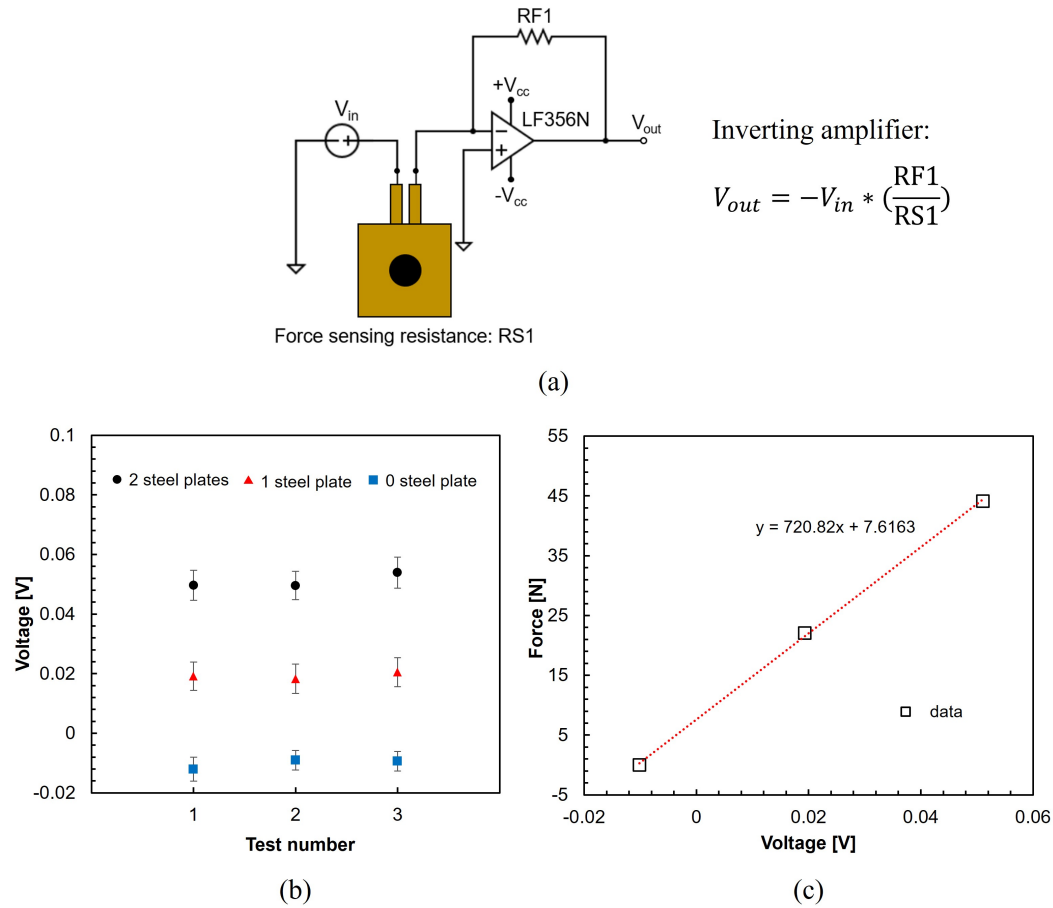

Figure 4.5: (a) Electric circuit diagram for the pressure sensing sensor. Inverting amplifier circuit is used to obtain a linear relationship between the input and output voltage. (b) Three-point calibration data with linearly varying weights. (c) Force-voltage relation derived from the calibration data. The linear regression equation is used in converting the voltage output from the impact force to the force value.

plate, and 44.145 N from two steel plates. The total average of three tests for each calibration condition is used to derive linear regression relation, and the regression plot and calibration data points appear in Fig. 4.5(c). The obtained regression relationship is used to convert voltage output to force value at impact testing.

5. THREE-DIMENSIONAL GRAFEA SIMULATION VERIFICATION ON FRACTURE OF QUASI-BRITTLE MATERIAL[1]

The main objectives of the current chapter are as follows: (a) to develop and implement the nonlocal three-dimensional GraFEA constitutive theory for modeling fracture in quasi-brittle materials into a parallelized CPU/GPU hybrid mode computing framework to accelerate the finite-element simulations; and (b) verify the developed three-dimensional nonlocal GraFEA constitutive theory and its parallelized CPU/GPU hybrid mode computational implementation with respect to experimental force-displacement data, load-time impulse data and crack patterns in samples, obtained from physical experiments on gypsum-based particulate composite test specimens and also for concrete samples.

The Compute Unified Device Architecture (CUDA) parallel computing is implemented in the calculation of damage driving force to increase the total computational performance. GPU-based parallel computing is getting attention in the implementation of the finite element method by changing the implementation structure in element level deformation calculations [153, 154] or using a subroutine to speed up the calculation at specific tasks [155]. The current work is implementing the parallel computing method in the nonlocal strain calculation subroutine, since this calculation step is a bottle neck in total computational performance. The three-dimensional nonlocal GraFEA simulations are performed to predict the fracture behavior of the gypsum-based composite material under impact loading conditions and the results are validated with the obtained experimental data. Finally, the efficacy of the three-dimensional nonlocal GraFEA simulation on simulating concrete fracture is shown under various loading conditions.

[1]Reprinted from the original reference of "Modeling impact fracture in a quasi-brittle solids using a 3D nonlocal graph-based finite element analysis: Theory, finite element simulations, and experimental verification" by H.Y. Shin, P. Thamburaja, A.R. Srinivasa and J.N. Reddy, 2023. *Journal of the Mechanics and Physics of Solids*, 170, 105097.

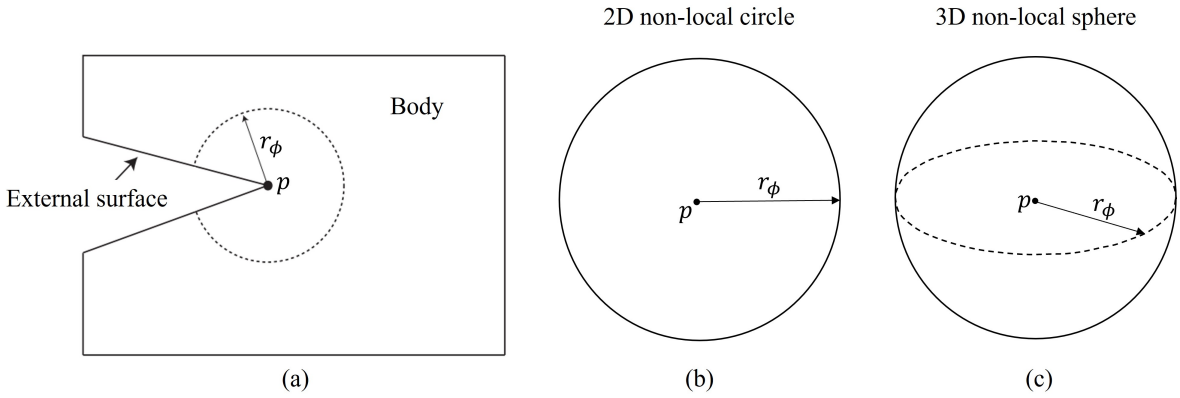

Figure 5.1: (a) Nonlocal fracture influence zone for a (b) two-dimensional case, and (c) three-dimensional case. The zone of influence (ZOI) is defined by the radius r_ϕ from material point $\mathcal{P}$. It represents the intrinsic material length scale governing the fracture process. The fracture response at material point $\mathcal{P}$ is influenced by the properties at material points within the ZOI. For the two-dimensional case, the ZOI is a circle whereas for the three-dimensional case, the ZOI is a sphere.

5.1 Three-dimensional nonlocal fracture process zone

Damage in quasi-brittle material starts from the numerous flaws in the material, such as voids or existing cracks, to form a microcracks. Generated microcracks link and coalescence with each other to form a fracture process zone and finally show visible macrocracks. A complex distribution and interaction of strains at the edge of microcracks are simplified through the assumption that a damaged state of a particular microplane is influenced by the state of strain and damage of material points that fall into a finite-sized fracture process zone. In the multiple cracking model, an integral-based nonlocal approach is used to represent fracture process zone, which is based on a nonlocal mechanics-based approach [156, 157], and it can be briefly described as follows:

Consider an arbitrary material point $\mathcal{P}$ in a body which is located at position $\mathbf{x}$ [see Fig. 5.1(a)]. A fracture zone of influence (ZOI) can be defined at material point $\mathcal{P}$ as a circular (for the two-dimensional case) or spherical (for the three-dimensional case) region $\mathcal{R}_f$ of radius r_ϕ. The material points within the ZOI influences the fracture properties at material point $\mathcal{P}$. Hence, r_ϕ represents an intrinsic material length scale governing the fracture process. Next, using a population dynamics-based approach [158], A joint survival probability of the i th crack plane can be de-

fined at location $\mathbf{x}$ considering the damage state of the crack planes at location $\mathbf{y}$, $P_i(\mathbf{x},\mathbf{y})$ through Eq. (5.1):

$$P_i(\mathbf{x},\mathbf{y}) = \phi_i(\mathbf{x})\,\omega(\mathbf{y}), \quad \omega(\mathbf{y}) = \frac{\sum_{i=1}^{K}\phi_i(\mathbf{y})}{K} \tag{5.1}$$

where $\omega(\mathbf{y})$ is the average survival probability at location $\mathbf{y}$. With dV representing the differential volume of an element, the expected nonlocal normal strain on the i th crack plane can be expressed at material point $\mathcal{P}$, $I_i(\mathbf{x})$ as Eq. (5.2):

$$I_i(\mathbf{x}) = (1/\bar{A}(\mathbf{x}))\left\{\int_{\mathcal{R}_f}\mathcal{H}(r_\phi - |\mathbf{x}-\mathbf{y}|)P_i(\mathbf{x},\mathbf{y})\,\mathbf{E}(\mathbf{y})\,dV\right\}\cdot\,\mathbf{N}_i(\mathbf{x}) \tag{5.2}$$

where $\mathcal{H}(*)$ represents the Heaviside step function of a given quantity $*$, and $\bar{A}(\mathbf{x})$ is the normalization factor at material point $\mathcal{P}$. The expression for $\bar{A}(\mathbf{x})$ appears in Eq. (5.3):

$$\bar{A}(\mathbf{x}) = \int_{\mathcal{R}_f}\mathcal{H}(\,r_\phi - |\mathbf{x}-\mathbf{y}|\,)\,\omega(\mathbf{y})\,dV. \tag{5.3}$$

The expected nonlocal normal strain represents the net influence of the strain and damage state at location $\mathbf{y}$ on location $\mathbf{x}$. This quantity is considered as the driving force for crack survival probability degradation. The developed constitutive theory of three-dimensional nonlocal GraFEA simulation has been implemented into the ABAQUS/Explicit [131] finite element program through a vectorized user-material (VUMAT) subroutine, where the detailed numerical implementation is provided in [140].

5.2 Numerical implementation with CPU/GPU hybrid computation

The GraFEA formulation is an integral based nonlocal damage model, and a damage evolution law uses the nonlocal strain as a driving force for damage growth. Each element inside the numerical domain has its own nonlocal zone, and the nonlocal zone consists of neighbor elements to represent the fracture ZOI. In the finite-element simulations, the quasi-brittle solid is meshed using reduced integration elements where the Gauss point of an element is located at the centroid of the element. Each Gauss point in a quasi-brittle simulation domain represents a material point.

<abaqus_v6.env> file

```
fortCmd = 'nvfortran'

compile_fortran = [fortCmd, '-fPIC', '-cuda', '-Mfree', '-c']

link_sl = [fortCmd,
        '-fPIC', '-shared', '-Mcuda',
        '%E', '-Wl,-soname,%U', '-o', '%U', '%F', '%A', '%L', '%B', '-Wl,-Bdynamic', '-llapack']

del fortCmd
```

Figure 5.2: Changes in ABAQUS environmental file settings. NVIDIA FORTRAN compiler (nvfortran) is used instead of the reference INTEL FORTRAN compiler. The necessary modifications are made in compile commands ('compile_fortran') and shared library linking commands ('link_sl') to use CUDA parallelization in the VUMAT code.

For the two-dimensional simulations, the quasi-brittle solid is meshed using continuum triangular elements whereas for the three-dimensional simulations, the quasi-brittle solid is meshed using tetrahedral elements. Moreover, for the two-dimensional calculations, it is set $K = 3$, and for the three-dimensional calculations, it is set $K = 6$. The quasi-brittle modeling domain is meshed to ensure that the diameter of the fracture ZOI spans at least 5 elements to ensure a mesh insensitive response [140].

The nonlocal strain calculation requires the source code to access the geometric and deformation information of every nonlocal neighbor element for each calculation time step. The loop calculation of this process using CPU-based sequential computing consumes a large portion of total computational time even though this part is only calculated once at the end of every time step increment. To reduce computational expense, this repetitive element loop level calculation can be spread into many-core computational environments, and a GPU can be utilized to perform this task [159, 160].

A GPU is designed to have many-core processing units, which is different from a multi-core processing unit of a CPU. A collection of a large number of simple processing units of GPU gives the best performance in highly parallel computing environments. A GPU developed by NVIDIA has a number of streaming multiprocessor (SM), which contains a set of low clock rate cores with a small cache. The main task of SM is the execution of parallel computing with its GPU cores. The

NVIDIA GPU is based on the platform of the CUDA, which is a hybrid programming framework utilizing CPU and GPU together for the computational task. The main execution steps of the logical process, serial computing, and memory transfer are performed by the host (CPU), while the parallel processing task is handled by the device (GPU). The parallel computing output from the GPU cores is transferred to the host by global memory, which is connected between the host and the device [161].

The reference compiler for the ABAQUS explicit solver is the Intel compiler, and for utilizing the CUDA packages for parallel computing, the ABAQUS environment file (the .env file) should be modified to enable the NVIDIA HPC compiler. Adding to the change in using the specific compiler, the compiler flags and dynamic library linking commands should also be modified to use the CUDA toolkit for GPU accelerated computations. An adequately modified environmental file should be located in the working directory to apply necessary changes in environmental settings. For the reference of the readers, wthe modified ABAQUS environmental file is shown for using CUDA computing in Fig. 5.2.

Next, an implementation of the computational algorithm and the time-integration procedure into the ABAQUS/Explicit solver is described using a VUMAT subroutine. The schematic flow-chart of the time-integration procedure and its implementation into a VUMAT subroutine is shown in Fig. 5.3.

The first step of the simulation is to initialize the ABAQUS platform by given discretized domain and simulation conditions, such as boundary and loading conditions. After the problem initialization, the ABAQUS/Explicit solver calculates the displacement of nodes in every time step increment based on the VUMAT subroutine. The task of the VUMAT subroutine is to calculate the stress and energy state of the elements for the given time step based on the defined constitutive model. The stress and energy states of elements are passed to the next time step with the user-defined solution dependent state variables. The time step increment is decided automatically by ABAQUS based on the material properties and the characteristic lengths of the deformed elements. The algorithm blocks for the GraFEA VUMAT are shown in the broken red box on the flow-chart.

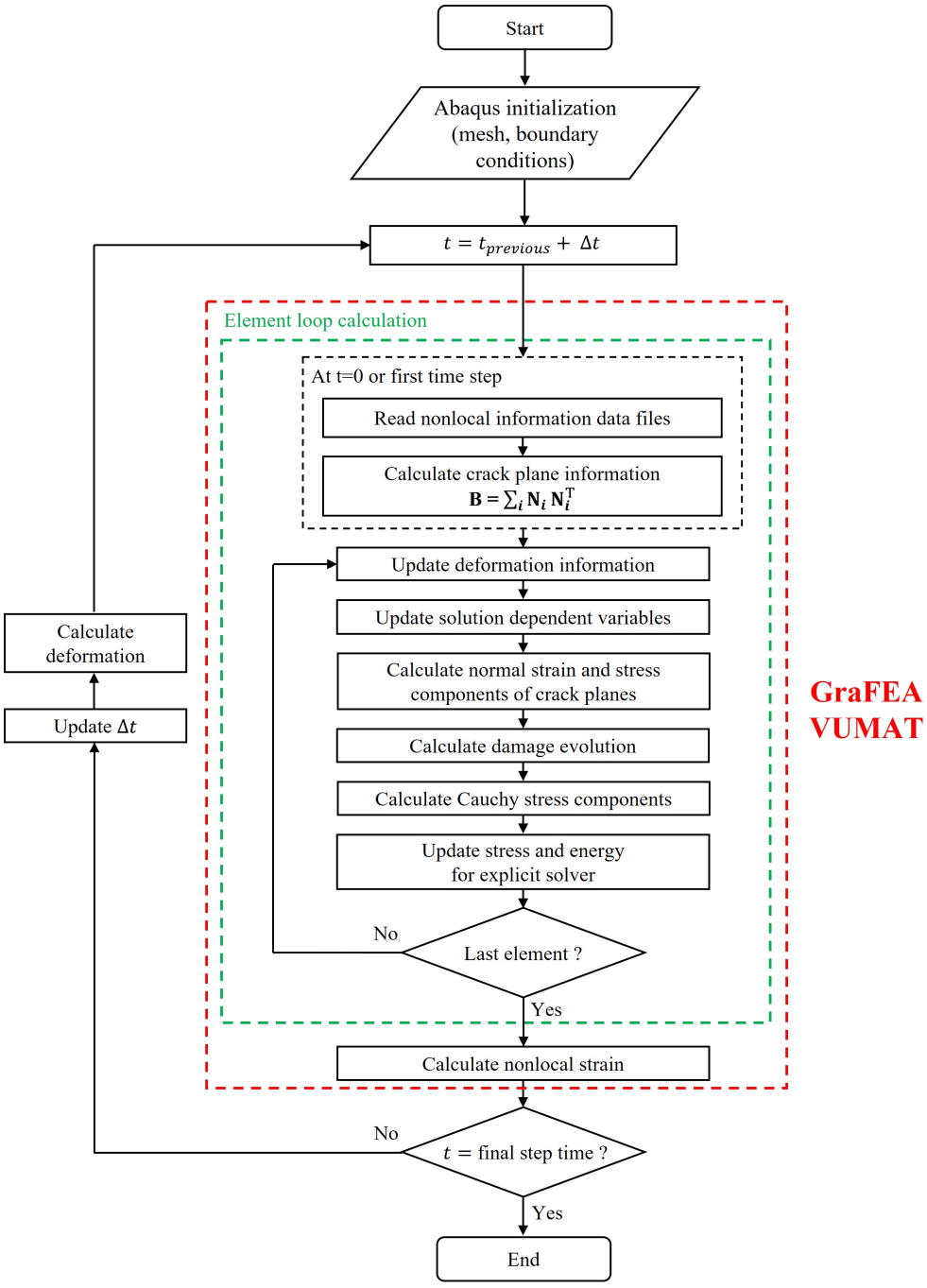

Figure 5.3: Flow chart of the three-dimensional ABAQUS/Explicit solver with nonlocal GraFEA VUMAT code. The nonlocal zone and crack plane direction information are imported at the initial stage of the VUMAT subroutine. The damage evolution is calculated inside of the element loop calculation and the nonlocal strain calculation is activated after the finish of the element loop calculation. The GPU computing is implemented at the nonlocal strain calculation step, and the rest of the code is executed by CPU.

CPU/GPU hybrid mode

```
!Assign block and grid size
blockSize = dim3(1024,1,1)
gridSize = dim3(ceiling(real(number_element)/real(blockSize%x)),1,1)
!Allocate host and device arrays
allocate(non-local_zone_volume(number_element))
allocate(device_non-local_strain(number_element,3,3))
allocate(device_local_strain(number_element,3,3))
allocate(device_average_damage(number_element))
!Calculate non-local zone volume
Transfer device_average_damage from host to device
call non-local_volume<<<gridSize, blockSize>>>(…)
 attributes(global) subroutine non-local_volume(…)
 id = (blockidx%x-1)*blockdim%x + threadidx%x
  if (id <= number_element) then
   Initialize non-local_zone_volume(id)
   do j=1,number_non-local(id)
    Calculate non-local_zone_volume(id)
   enddo
  endif
 end subroutine non-local_volume
istat = cudaDeviceSynchronize()
!Initialize non-local strain array
do i=1,number_element
 Initialize non-local_strain array
enddo
!Calculate non-local strain array
Transfer device_non-local_strain from host to device
Transfer device_local_strain from host to device
call non-local_compute<<<gridSize, blockSize>>>(…)
 attributes(global) subroutine non-local_compute(…)
 id = (blockidx%x-1)*blockdim%x + threadidx%x
  if (id <= number_element) then
   if(non-local_zone_volume(id) > 0.0)then
    do j=1,number_non-local(id)
     Calculate non-local_strain(id,1,1)
     Calculate non-local_strain(id,1,2)
                    ⋮
     Calculate non-local_strain(id,3,3)
    enddo
   endif
  endif
 end subroutine non-local_compute
Transfer device_non-local_strain from device to host
!Deallocate host and device arrays
deallocate(non-local_zone_volume)
deallocate(device_non-local_strain)
deallocate(device_local_strain)
deallocate(device_average_damage)
```

CPU sequential mode

```
!Calculate non-local zone volume
do i=1,number_element
   Initialize non-local_zone_volume(i)
  do j=1,number_non-local(i)
   Calculate non-local_zone_volume(i)
  enddo
enddo
!Initialize non-local strain array
do i=1,number_element
 Initialize non-local_strain array
enddo
!Calculate non-local strain array
do i=1,number_element
 if(non-local_zone_volume(i) > 0.0)then
  do j=1,number_non-local(i)
   Calculate non-local_strain(i,1,1)
   Calculate non-local_strain(i,1,2)
                  ⋮
   Calculate non-local_strain(i,3,3)
  enddo
 endif
enddo
```

Figure 5.4: Nonlocal strain calculation with (a) CPU/GPU hybrid mode and (b) CPU sequential mode. The CPU sequential model is composed of multiple loop calculations. The nonlocal zone volume calculation is activated first and used in the nonlocal strain calculation. The main structure of the CPU/GPU hybrid mode is the same as the CPU sequential mode. The dynamic memory allocation is used for arrays related to the nonlocal strain calculation. The nonlocal zone volume subroutine and nonlocal strain subroutine are parallelized using CUDA computing, and these steps are highlighted in the green broken boxes.

The nonlocal information data flies are imported at the initial time and first time step increment. From the imported nonlocal information, the crack plane information is calculated once and saved as common variables through the simulation's lifetime and used when necessary. The normal strain is calculated from the local strain components and crack plane directional information. The survival probability is calculated based on the evolution law, which utilizes nonlocal strain as the driving force of damage. The nonlocal strain from the current step is passed to the next time step calculation by solution dependent variable. The calculated survival probability for the current time step is used in equivalent strain calculations, and the Cauchy stress tensor calculation follows. Each element's loop calculation is finished when the stress, energy, and solution dependent variables are updated for the next time step calculation. After finishing the element loop calculation, the GraFEA VUMAT activates the nonlocal strain calculation.

The code structures of nonlocal strain calculation for different computing modes are shown in Fig. 5.4. The left column shows CPU/GPU hybrid mode, and the right column shows CPU sequential mode. The CPU sequential model is composed of multiple simple loop calculations. The first loop is related to calculating the total volume of the nonlocal zone by considering the damage state and volume of each element. After the initialization of the nonlocal strain array, the code executes a loop calculation for nonlocal strain components. The first part of the CPU/GPU hybrid mode is the initialization of the variables, which are related to the nonlocal strain calculation but only used in the device. This part is executed once at the first step time when the main code processes nonlocal information and calculates crack plane information. The elemental volume data and nonlocal zone data are imported and stored in the device global memory through the lifetime of the simulation. A process of nonlocal strain calculation of CPU/GPU hybrid mode is similar to CPU sequential mode, but the data transfer between the host and device is required. Three-dimensional type variables are used to assign a number of threads per block (blockSize) and a number of blocks per grid (gridSize). The thread numbers per block is fixed as 1024 and the grid size is decided by a ceiling function. The dynamic memory allocation is used to allocate a nonlocal zone volume array at the host, and the strain and damage arrays in the device. The damage array is

transferred from the host to the device, and the device kernel subroutine is activated to calculate the total volume of the nonlocal zone. The code structure of the kernel subroutine appears in the green broken box. The CUDA device management function follows to make the host wait for all stream processors to finish the execution. The initialization step of the nonlocal strain array is the same as the CPU sequential mode. The nonlocal strain calculation starts with the data transfer of the local strain array and the initialized nonlocal strain array. The kernel subroutine for nonlocal strain calculation is activated at the device, and the device array is transferred to the host nonlocal strain array after the calculation. Finally, the nonlocal calculation step is finished with the deallocation of the arrays.

The ABAQUS/Explicit solver is used to solve the boundary value problem through the implementation of the constitutive theory into a vectorized user material subroutine (VUMAT) interface. The Abaqus/Explicit VUMAT is written using the FORTRAN language. The ABAQUS/Explicit solver with the GraFEA VUMAT is run on the Intel x86-64 Linux cluster, and the cluster server uses the SLURM job scheduling system. A single core of an Intel Xeon 6248R (Cascade Lake) at 3.0 GHz clock speed is used as the main processor. The total allocatable memory of the system is 384 GB DDR4 ram, and different memory space is assigned to the simulation depending on the memory size of the problem. For the device calculation, a NVIDIA A100 GPU is used with an available memory space of 40 GB. The ABAQUS 2021 version is used for the simulations, and the NVIDIA HPC Software Development Kit (SDK) is used to utilize necessary compilers, libraries, and software tools for the GPU parallel computing.

5.3 Verification of CPU/GPU hybrid three-dimensional GraFEA simulation in concrete fracture

The developed three-dimensional nonlocal GraFEA simulation with the GPU implemented parallel computing is used in this section to show the efficacy of the developed method on simulating the fracture of concrete beam samples under impact loading conditions. Previously, the fracture of a high-strength concrete beam sample under low-speed impact loading conditions is simulated with the two-dimensional nonlocal GraFEA simulation using a CPU sequential execution. Fur-

Table 5.1: Material constants for high strength concrete [148]

$Y = 18$ GPa	$\nu = 0.2$	$I_0^c = 1.3 \times 10^{-4}$	$G_0 = 450$
$r_\phi = 4.5$ mm	$\dot{e}_0 = 3 \times 10^{-6}$/s	$c_0 = 0.055$	$\rho = 2368$ kg/m^3

thermore, a complicated three-dimensional boundary value problem is simulated involving crack closure in a concrete cylinder sample under cyclic shear loading conditions.

5.3.1 Concrete beam impact fracture

The developed multiple cracking model under the three-dimensional GraFEA framework is used in simulating the damage behavior of high-strength concrete under impact loading conditions. The load-time (impulse) curves and cracking patterns from the simulations are validated through the experimental reference data obtained by Zhang *et al.* [145]. A configuration of the notched beam specimen is shown in Fig. 4.2. The dimension of the beam is (length $\times$ width $\times$ depth = 420 $\times$ 100 $\times$ 100 mm^3), with a notch width of 6mm and notch depth of 50 mm. The span of the beam sample is 300 mm. At the reference experiment, three different impact velocities were tested by changing the drop height of the steel hammer with a mass of 120.6 kg, where the obtained velocities were 0.881, 1.76, and 2.64$\times$ 10^3 mm/s. The reaction force from the impact was measured through the load cell attached to the hammer.

For the three-dimensional nonlocal GraFEA simulation, the notched concrete beam is discretized using reduced integration four-noded tetrahedral elements (C3D4 ABAQUS elements). The supports and hammer are modeled as analytical rigid surfaces. The reference nodes for the rigid support are fixed in translational and rotational movement. An impact velocity is imposed on the reference node of the rigid hammer as an initial condition in the ABAQUS input file. The impact force on the concrete sample is given by the absolute value of multiplication between the mass of the hammer and its deceleration due to an impact reaction. A general contact method is used (*CONTACT) for surface interactions between elements and rigid surfaces, where the friction effect is ignored.

The material parameters in the constitutive theory, $\{ Y , \nu , r_\phi , G_0 , I_0^c , \dot{e}_0 , c_0 , \rho \}$, used for the

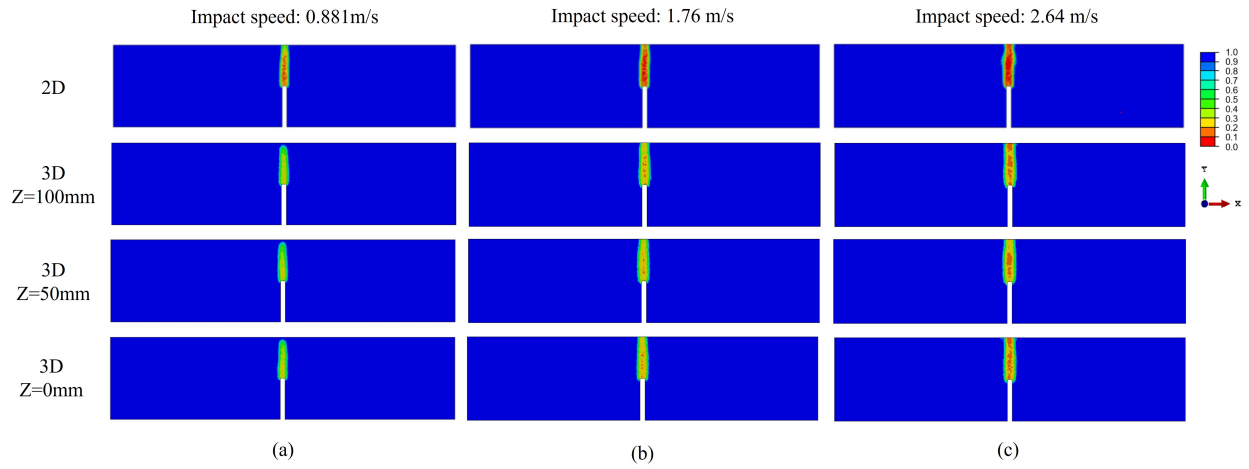

Figure 5.5: The crack propagation paths obtained from the two- and three-dimensional nonlocal GraFEA simulation for an initial impact speed of (a) 0.881×10^3 mm/s, (b) 1.76×10^3 mm/s, and (c) 2.64×10^3 mm/s. The contours of average survival probability are displayed. The two-dimensional images only show the generated crack path at one surface plane, but the three-dimensional cases can show crack paths on different cross-sectional planes of the front surface ($Z = 100$ mm), middle plane ($Z = 50$ mm), and back surface ($Z = 0$ mm). The crack path that appears in the two- and three-dimensional cases matches well with the experimental result, where the crack starts from the notch tip and fractures the beam sample into two pieces.

three-dimensional impact simulations, are obtained from the previous two-dimensional concrete beam fracture simulations [148]. These parameters are listed in Table. 5.1. The comparison of the crack paths between the two- and three-dimensional simulations are shown in Fig. 5.5. The crack paths from the different impact velocities start from the tip of the notch, and the damage evolution reaches the loading surface. From the generated crack, the concrete samples fractured into half in both two- and three-dimensional simulations, which are the same as the experimental result. It should be emphasized that both the two- and three-dimensional simulations use the nonlocal zone size $r_\phi = 4.5$ mm, and it appears in the formulation as the nonlocal circle for the two-dimensional case and the nonlocal sphere for three-dimensional simulations. The crack paths for both two- and three-dimensional simulations show similar width, which represents the fracture process zone size is well preserved in the three-dimensional GraFEA simulation. In the three-dimensional simulation results, a generated crack path in the middle plane of the thickness direction can be observed at

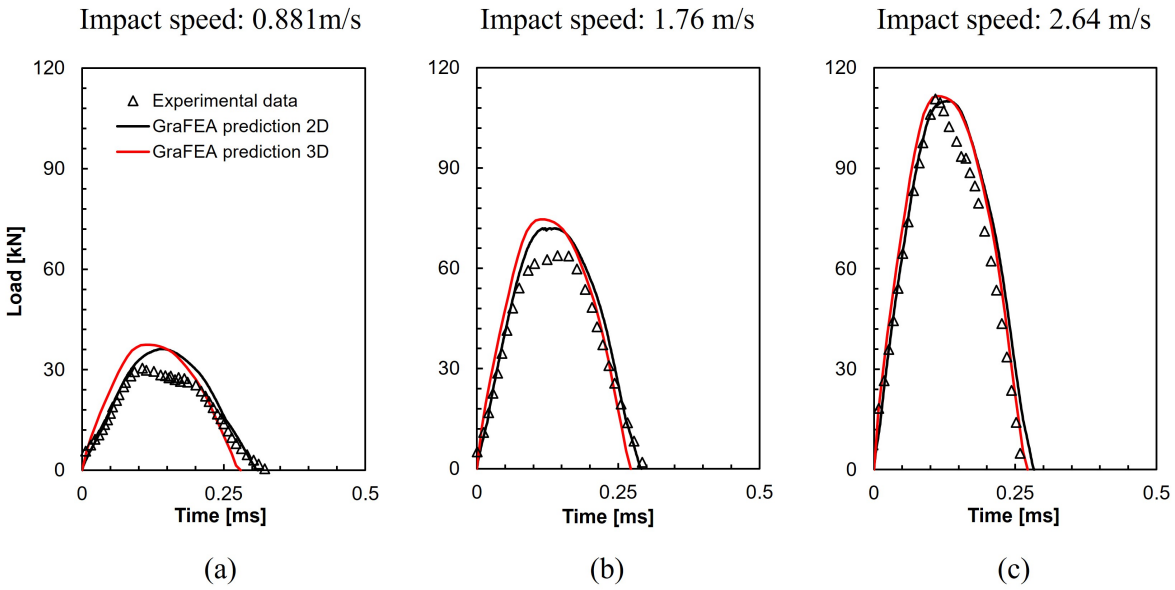

Figure 5.6: The impact load-time curves obtained from the raw experimental data [145] and two- and three-dimensional GraFEA simulations for an initial impact speed of (a) 0.881×10^3 mm/s, (b) 1.76×10^3 mm/s, and (c) 2.64×10^3 mm/s. The impact impulse response is well predicted in both the two- and three-dimensional simulation results once the raw experimental data are properly shifted. The initial slope of the load-time curves and the peak loads are slightly over-predicted in the three-dimensional simulation.

the $Z = 50$ mm plane. The crack path of the $Z = 100$ mm plane shows the damage at the front surface of the beam sample and the cross-sectional view at $Z = 0$ mm shows crack path at the back surface. From the given crack paths in three cross-sectional planes, the crack growth in the whole region of thickness direction can be confirmed, which shows a three-dimensional crack propagation characteristic.

The load-time curves from the three-dimensional GraFEA simulations are shown in Fig. 5.6. The two-dimensional GraFEA simulation results are also included in Fig. 5.6 for comparison purposes. From the simulation results shown in Fig. 5.6, it can be concluded that the three-dimensional GraFEA calculations are also able to quantitatively match the experimental force-displacement response for all three loading rates to good accuracy. In particular, the three-dimensional calculations are also showing that increasing drop hammer kinetic energy results in increasing peak load. Furthermore, the simulated duration of the impact loading are also in good agreement with

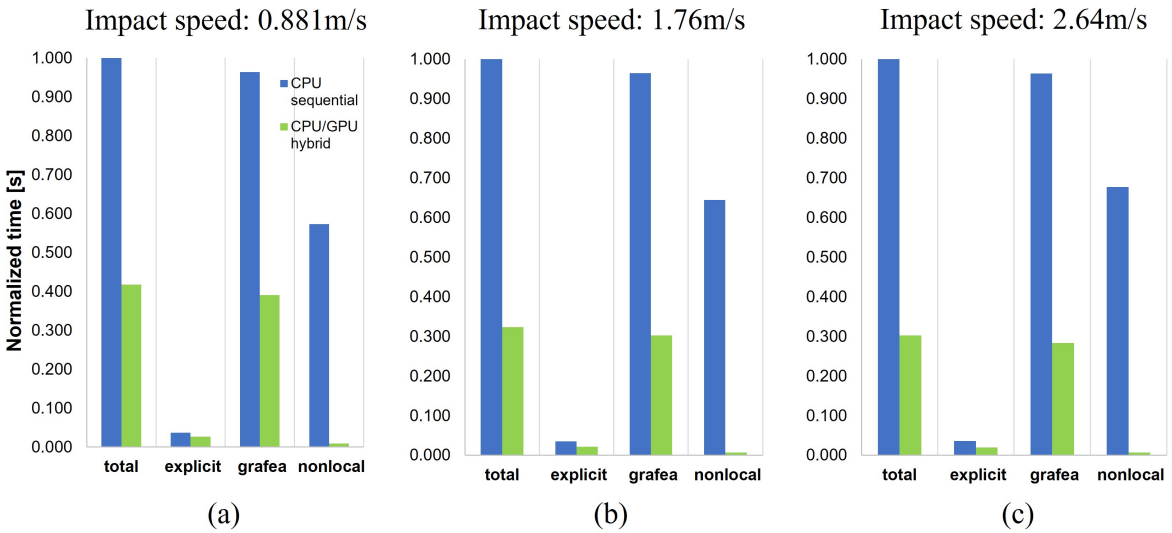

Figure 5.7: Normalized computational time for each calculation step of ABAQUS explicit three-dimensional GraFEA VUMAT simulation for an initial impact speed of (a) 0.881×10^3 mm/s, (b) 1.76×10^3 mm/s, and (c) 2.64×10^3 mm/s. The computational time for each step is normalized by the total computation time of the CPU sequential mode. The speed-up achieves at the nonlocal step calculation with the CPU/GPU hybrid mode is $63 - 113$ times compared to the CPU sequential mode. From this, the total computational time of the hybrid mode reduces to 30-42% compared to the sequential mode.

experimental data, for both the two- and three-dimensional simulations. Although the trend of the simulation curve matches well with the experimental data, the GraFEA results show an over-prediction at some peak loads. The mismatch in the load value can be attributed from the absence of capability in the proposed model in describing the damage from compression state and plasticity, which can manifest under compressive loads [162]. Overall, it can also be concluded that the two- and three-dimensional simulations produce matching results to a sufficiently high degree (with little differences in the impulse response), thus reinforcing the choice of modeling this experiment using a two-dimensional framework as pursued in the previous work [148].

A computational time comparison between the CPU sequential mode and the CPU/GPU hybrid mode for this boundary value problem is shown in Fig. 5.7. The comparison is made for the time consumed at the different steps of the simulation life cycle. The total step represents the computational time taken for the entire simulation process. The explicit step shows time consumed

at the ABAQUS explicit solver, which is outside the VUMAT calculation process. The GraFEA step shows the time used in the three-dimensional nonlocal GraFEA VUMAT calculation, and the nonlocal step represents the time consumption of the nonlocal strain calculation, which is inside the GraFEA VUMAT code. The bar graphs show the normalized time, where each step time is divided by the CPU sequential mode total computational time. A small portion of time is consumed at the explicit calculation step, which is 4% of the total computation time in the CPU sequential mode. At the CPU sequential mode, most of the computational time took from the GraFEA VUMAT calculation, which is 96% of the total simulation time. Inside the GraFEA VUMAT code, the nonlocal strain calculation step takes the largest portion of time consumption which is 55-65% of the GraFEA VUMAT calculation time and 57-68% of the total computational time. Therefore, a focus is set on reducing the nonlocal strain calculation time to improve the total computational efficiency in terms of time. By using the CUDA enabled nonlocal strain calculation, the time taken at nonlocal strain calculation step is reduced tremendously to $0.6 - 0.9\%$ of the total simulation time. The speed-up achieved from the CUDA parallelization is $63 - 113$ times at the nonlocal strain calculation. From the saved time consumption at the nonlocal strain calculation step, the total simulation time of the hybrid mode reduces to $30 - 42\%$ compared to the sequential mode. Therefore, it is confirmed that the implementation of the CUDA parallel computing at the nonlocal strain calculation reduces computational time significantly.

5.3.2 Concrete cylinder cyclic loading condition

Finally, a simulation of boundary value problem under cyclic shear deformation is conducted to address the capability of the developed model in describing three-dimensional nonlocal crack closure. A circumferentially notched cylinder specimen is used in the simulation, originating from the experimental specimen proposed by Bazant and Prat [132]. The meshed configuration is shown in Fig. 5.8(a), where the domain is discretized with the four-node regular tetrahedron element (C3D4 ABAQUS element). The boundary and loading conditions appear in Fig. 5.8(b). The displacement of the nodes at the $Z = -d$ plane is fixed in all translational movements. Directions of the loading conditions appear with arrows, where the loading conditions are applied as velocity conditions to

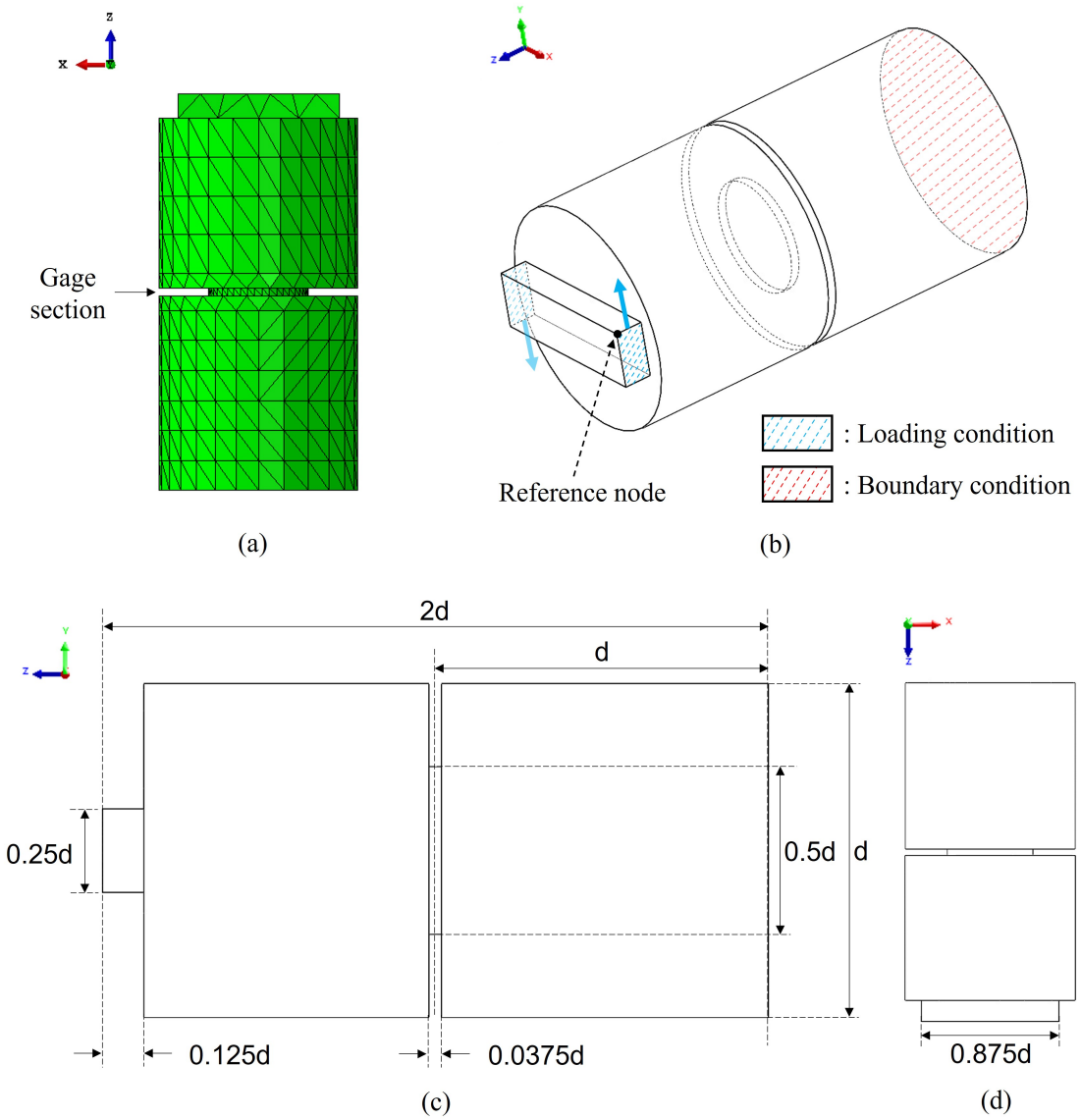

Figure 5.8: (a) The configuration of the circumferentially notched cylinder specimen discretized with the ABAQUS C3D4 tetrahedron elements. (b) Boundary and loading conditions imposed on the meshed domain shown in (a). The imposed cyclic shear loading conditions induce damage at the gauge section of the specimen. Plan view of the specimen in (c) X axis, and (d) Y axis with dimensional information. The diameter of the specimen is $d = 160$ mm.

the nodes at the highlighted surfaces. The displacement profile is applied to the $X = 0.4375d$ plane in the positive Y direction, whereas the $X = -0.4375d$ plane has the same magnitude of displacement but in the opposite direction. The imposed boundary and loading conditions impose a torsional force on the gauge section of the specimen. The dimensions of the specimen are shown

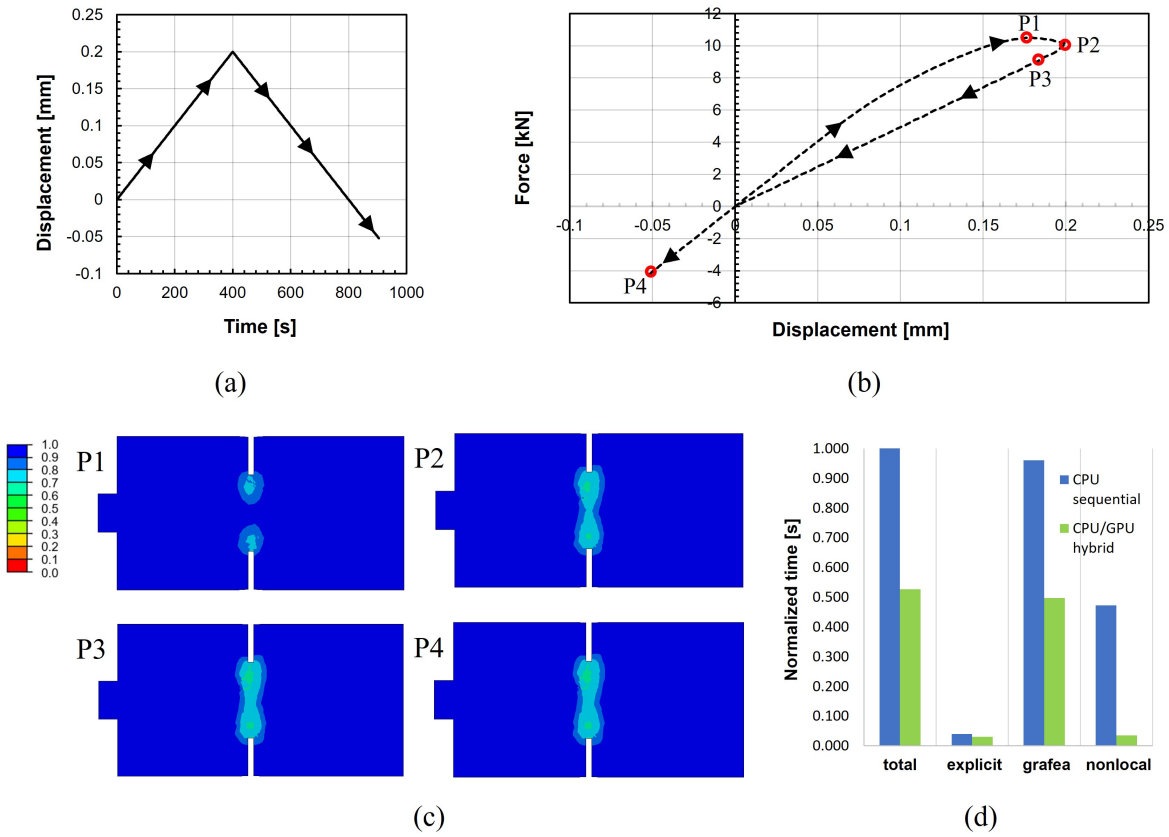

Figure 5.9: (a) The applied displacement profile at the loading surface to impose cyclic shear loading, and (b) its corresponding force-displacement curve of the cylinder specimen. The crack closure behavior appears as a recovery of the initial stiffness after the strain softening response. (c) The damage evolution history at the gauge section. Contours of average survival probability in the sample are plotted. The damage starts at the notch tip and evolves to the center line of the specimen. The damage stops growing in the reverse loading condition (from P3 to P4) since the opened crack planes are turning into closing mode. (d) Normalized computational time for each calculation step. The simulation times are normalized with respect to the total time taken to complete the CPU sequential model calculation. The total computational time of the CPU/GPU hybrid mode reduces to 53% of the CPU sequential mode.

in Figs. 5.8(c) and 5.8(d), where the cylinder diameter is $d = 160$ mm and the width of the center notch is 6 mm.

The material parameters used for the simulation are the same with the notched concrete beam samples at the impact testing (see Table. 5.1), but the softening parameter is changed to $G_0 = 4\times10^3$ to obtain a faster softening response. Using the imposed quasi-static displacement-time profile shown in Fig. 5.9(a) to load the sample, the simulated force–displacement response obtained from

the reference node of the sample [see Fig. 5.8(b)] is shown in Fig. 5.9(b). Starting from zero load and zero displacement, applied deformation results in a linear force-displacement response of the initially undamaged material, indicating elastic behavior. A damage generation starts before the peak load is attained, and the nonlinear response is observed due to the generated damage and cracking in the sample. A peak force is attained at an applied displacement of 0.178 mm, and the cross-sectional image of the damaged domain at the $x = 0$ plane is shown in Fig. 5.9(c) keyed to point P1 of the force–displacement response shown in Fig. 5.9(b). The damage starts from the tip of the circumferential notch, and the damage accumulation leads the material response to show strain–softening behavior. The loading direction is reversed at the displacement of 0.2 mm, and the damaged state at this point is shown in Fig. 5.9(c) keyed to point P2 of the force–displacement response shown in Fig. 5.9(b). The direction of the damage growth can be ascertained from images P1 and P2, that is, that damage starts from the tip of the notch and grows to the center line of the cylinder specimen to form a coalescence damage zone. Once reverse loading commences, a reduced stiffness can be seen in the force–displacement response [see Fig. 5.9(b)] caused by the generation of cracks in the sample during the forward loading step. The trace of the force under the reverse loading condition shows a sharp turn followed by a nominally linear response. The images of the damaged zone in the sample under the reverse loading are shown in Fig. 5.9(c) keyed to points P3 and P4 of the force–displacement response shown in Fig. 5.9(b). The comparison between images P2, P3 and P4 show no further damage evolution in the sample under the reverse loading step.

Once the simulated load-displacement response [see Fig. 5.9(b)] enters the third quadrant (negative displacement and negative load), it can be clearly seen from the simulated force–displacement response that the original stiffness of the sample has been recovered. In other words, the stiffness of the sample in the third quadrant of the force–displacement graph is equal to the stiffness of the sample in the forward loading step prior to any damage in the sample. Although the generated damage still remains in the sample [see P4 of Fig. 5.9(c)], the closed crack planes caused by the applied displacement entering the negative region, that is, crack closure results in the sample re-

covering its undamaged stiffness. Therefore, this result shows that the three-dimensional nonlocal GraEFA theory and finite-element simulation method can describe crack closure response under cyclic loading conditions.

Finally, a comparison is made on the simulation times for this three-dimensional boundary value problem using a CPU sequential mode and a CPU/GPU hybrid mode. The simulation time data comparison for these two computational modes are shown in Fig. 5.9d. The simulation times are normalized with respect to the total time taken to complete the CPU sequential mode calculations. By using the CUDA parallel computing in nonlocal strain calculation, the calculation time at the nonlocal step is 13 times smaller in a CPU/GPU hybrid mode compared to the CPU sequential mode. Eventually, for this boundary value problem, the total computational time taken from using the CPU/GPU hybrid mode is 53% less than the CPU sequential mode. From the data shown in Fig. 5.9d, it can be clearly seen the improvement in computing times when a CPU/GPU hybrid mode computing framework is pursued instead of just using a CPU sequential mode calculation. Finally, it should be noted that the simulation results obtained from using a CPU sequential mode or a CPU/GPU hybrid mode are identical.

5.4 Validation of the numerical model with the ball drop impact test

5.4.1 Material parameter fitting process

To determine the material parameters for the Plaster of Paris, it is required a combination of a fitting process of the constitutive model to the experimental force-displacement response which links information available in the literature and microstructural information. The force-displacement curves obtained from the quasi-static experiments are displayed in Fig. 4.3(b). The experimental curves are slightly shifted along the displacement axis to properly match the initial slope, as slack in the experimental testing setup is inherent. All the curves from the experimental data show an initial linear region of force increment and softening behavior after the peak load, where the general trend of the curves matched well with the damage behavior of quasi-brittle materials [26, 142]. The peak loads range from 172 N to 228 N and the steady-state responses appear

Table 5.2: Material constants for plaster/aggregate composite

$Y = 1.7$ GPa	$\nu = 0.2$	$I_0^c = 4.1 \times 10^{-4}$	$G_0 = 650$
$r_\phi = 2.5$ mm	$\dot{e}_0 = 3 \times 10^{-6}$/s	$c_0 = 0.002$	$\rho = 1600$ kg/m^3

from 15 N to 32 N. Finally, it is important to emphasize that although the material composition is the same for the beam samples (S1-S3), the force-displacement curves in Fig. 4.3(b) show a scattered response which is typical of quasi-brittle solids such as concrete [142].

For the fitting process, a two-dimensional nonlocal fracture GraFEA simulation is performed for a half-beam due to the symmetry of the imposed boundary conditions and loading conditions on the Plaster of Paris beam. Fig. 4.3(b) shows the force–displacement curve obtained from the FEM simulation and it quantitatively matches the experimental data to good accord. The contour plot displayed inset of Fig. 4.3(b) shows the average survival probability at each element within the beam, and it clearly displays a mode I type fracture response.

The material parameters for Plaster of Paris material are obtained using the following procedure: the density of the material is measured as $\rho = 1600$ kg/m^3 using Archimedes' principle; the Poissons's ratio is chosen as $\nu = 0.2$ where literature data show a distribution between 0.18 to 0.24 [163, 164]; the diameter of the nonlocal zone sphere is taken as $2r_\phi = 5$ mm to match the maximum size of the coarse aggregate following the procedure of [140]. This is based on the assumption that the fracture is dominated by the debonding of the particulates resulting in an undulating crack path with many microcracks. For this to occur, it is expected the zone size to be at least the size of the largest particle (so that the crack can grow around the particle). Of course, if the concentration of the particles is very low, so that distance between the particles in much larger than the particle size, then the crack growth is dominated by the intrinsic fracture properties of the base material (cement or gypsum) m (matrix cracking), the crack path is relatively unhindered, resulting in a very small zone size and very low strength, brittle response.

In this case, based on the work of Chandrasekhar [165] (p89, Eq. 676) it can be estimated that the average center distance between randomly dispersed particles in a region as $< r > \approx$

$0.554/n^{1/3}$), where n is the number of particles per unit volume. For spherical particles of radius R and volume fraction c, this reduces to

$$< r >= 0.893 \times R/c^{1/3} \tag{5.4}$$

for this case, the volume concentration of particles is about 29% with a mean particle diameter of about 4mm so that the mean distance between particles is $< r >= 2.6$ mm which is comparable to the large particle radius. This justifies the zone size being about $r_\phi = 2.5$ mm that was chosen here. The Young's modulus of the material in tension is determined as $Y = 1.7$ GPa by matching the initial linear elastic slope of the experimental force-displacement response; the rate-independent threshold strain is set at $I_0^c = 4.1 \times 10^{-4}$ to match the experimental steady-state force-displacement response; the softening rate parameter is taken as G_0 = 650 to match the general trend of the experimental force-displacement softening response; due to the lack of experimental data on the rate-dependent behavior of the gypsum-based composite, the threshold strain-rate for a rate-dependent cohesive response is set as $\dot{e}_0 = 3 \times 10^{-6}$/s where as a first-cut assumption, it is taken to be equal to that of plain concrete [140]; finally, $c_0 = 0.002$ is set to match the initial slope of the softening response. The material constants for the Plaster of Paris material are listed in Table. 5.2.

Using the calibrated material parameters listed in Table. 5.2, a validation is made for the constitutive theory and its numerical implementation with respect to three-dimensional impact experiments on the Plaster of Paris samples.

5.4.2 Impact response: independent verification

The simulation domain is constructed based on the impact experimental set-up. Each part of the discretized domain is shown in Fig. 4.4d with information on element types used. Analytical rigid surfaces are used to express the surface of the steel ball and foundation. The impact velocity of 1.89×10^3 mm/s is imposed on the steel ball reference point as an initial condition. A reference point of the foundation is fixed in translational and rotational movement. A plaster disc sample

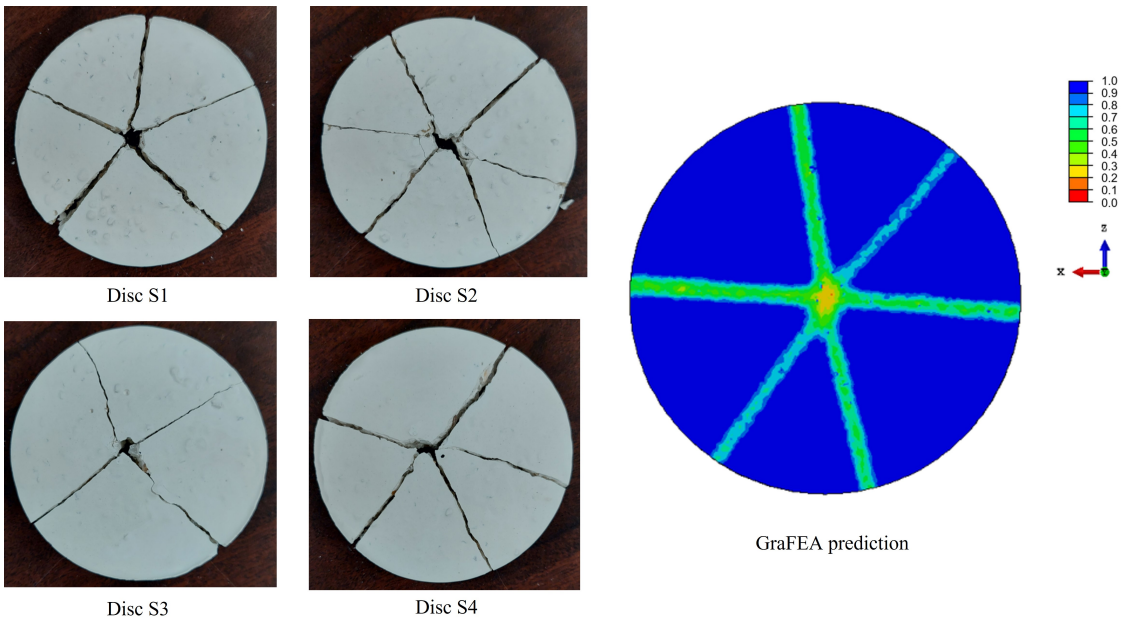

Figure 5.10: The crack propagation paths appear on the top surface of the gypsum disc samples in (a) experimental data and (b) simulation results. The experimental data show 4 to 6 macrocracks on the top surface from the ball drop tests. The prediction made from the three-dimensional nonlocal GraFEA simulation shows 6 macrocracks, which matches well with the Disc S2 experimental result.

is discretized with the four-node regular tetrahedron element (C3D4 ABAQUS element) and the remaining simulation domain is discretized with the eight-node brick element with reduced integration (C3D8R ABAQUS elements). A general contact method (*CONTACT) is used for all surface interactions, and a frictional effects are ignored in the simulations as a first-cut assumption.

The final crack paths obtained from the ball drop tests appear in Fig. 5.10(a) and Fig. 5.11(a), where the Fig. 5.10(a) pictures show viewpoint from the top surface and the Fig. 5.11(a) pictures show the bottom surface of the disc samples. The images in Fig. 5.10(b) and Fig. 5.11(b) show final crack paths from the three-dimensional nonlocal GraFEA simulation, where Fig. 5.10(b) shows generated final cracks in the top surface and Fig. 5.11(b) shows bottom surface crack paths. The experimental data show 4 to 6 generated macrocrack paths from the conducted ball drop impact tests. The final crack paths from the simulation show 6 major cracks and this matches well with the crack paths of the Disc S2 sample. The images of the damaged discs show more damage oc-

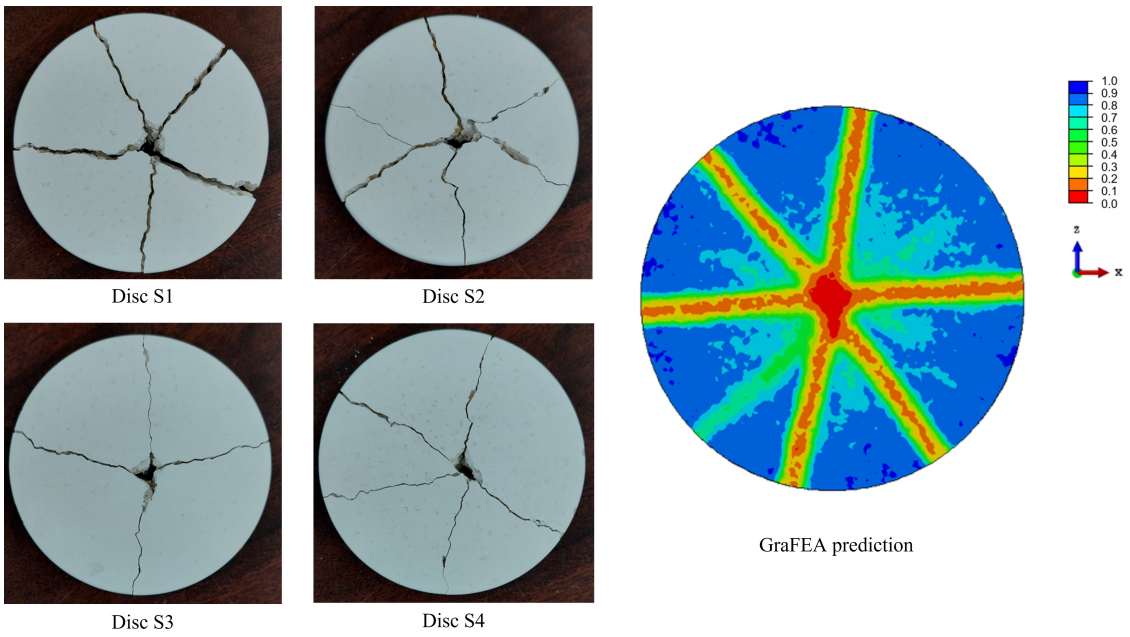

Figure 5.11: The crack propagation paths appear on the bottom surface of the gypsum disc samples in (a) experimental data and (b) simulation results. At the experimental data, the small spalling zone appears at the bottom surface right below the steel ball impact point. The simulation result shows a concentrated damage zone at the center of the bottom surface, which is considered the spalling zone.

curred at the center region of the disc bottom surface compared to the top surface center where the steel ball impacts the disc sample. This phenomenon is well captured with the three-dimensional GraFEA simulation, where the most damaged region appears at the bottom surface center.

The damage evolution history from the impact loading condition is well described in Fig. 5.12. The figure shows the time history of the average survival probability evolution at the top and bottom surfaces. The damage first appears at the bottom surface right below the steel ball impact point, but the top surface is not having damage at $t = 0.15$ ms. The damage at the bottom surface continuously grows to form a widely spreading damage zone at the bottom surface at $t = 0.35$ ms. At this time, the damage at the top surface can be observed. The wide dispersion of the damage at the bottom surface is then concentrated in some areas to form concentrated damage lines at $t = 0.45$ ms, which can be considered possible crack propagation paths. The final crack paths are

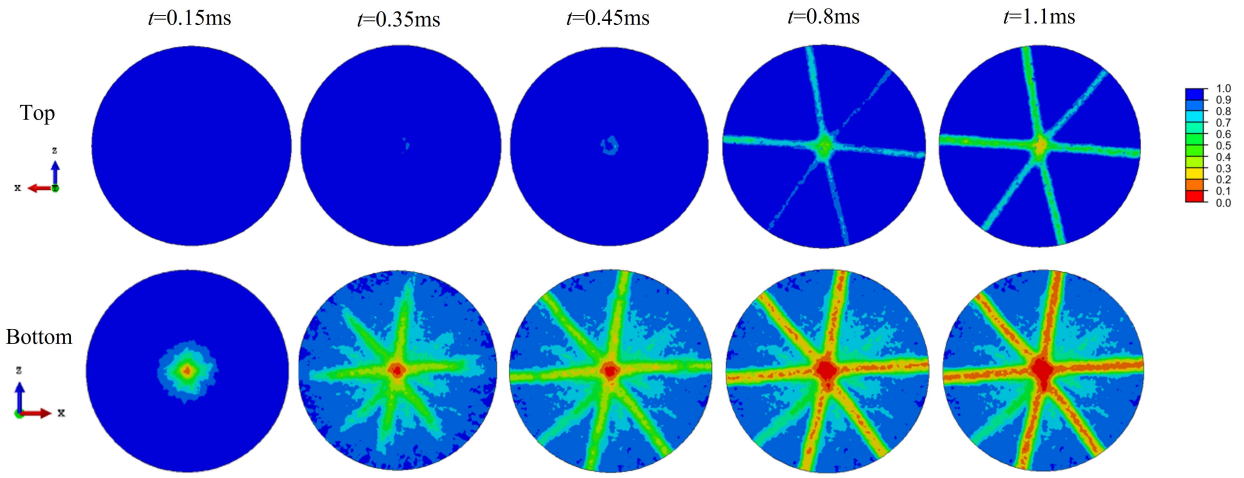

Figure 5.12: The simulation time history of the damage evolution at the top and bottom surface of the gypsum-based disc sample. The contours of average survival probability are displayed. The damage first appears at the bottom surface and is widely spread throughout the whole surface. The concentration of the damage clearly generates 6 major cracks, which start to appear at $t = 0.8$ ms. The damage zone smears into the top surface to form 6 major cracks aligned with the macrocracks that appear on the bottom surface.

clearly seen in the top and bottom surface images obtained at $t = 0.8$ ms. The 6 major crack paths first appear at the bottom surface, and then the damage evolves to reach the top surface. From this damage evolution history, the top surface does not show a wide damage dispersion but only shows a concentrated damage zone following the major crack paths. The final images of damage behavior at t=1.1ms show the final crack paths are well maintained and further damage growth is only concentrated in the major cracked regions.

The load-time (impulse) curves from the experimental data and simulation result are shown in Fig. 5.13(a). The load value is measured from the sensor at the support and the impulse response is appeared from the impact force with the multiple peak loads [166]. The experimental curves are properly shifted to match the second peak load to the simulation curve as in standard practice. The load-time curve determined from the three-dimensional nonlocal GraFEA simulation is obtained using the material parameters fitted from the quasi-static loading conditions (see Table. 5.2). A pure prediction is made for impact testing with the material parameters based on the quasi-static loading conditions, where the loading rate difference is about 6 to 7 orders of magnitude. From

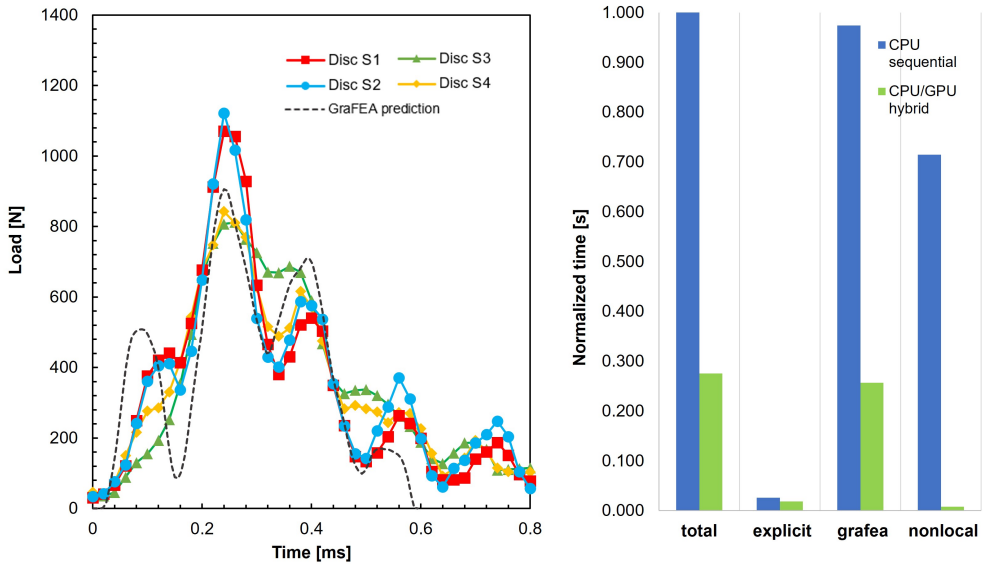

(a) (b)

Figure 5.13: (a) Load-time curves based on the experimental data and the three-dimensional GraFEA prediction. The experimental data are shifted to match the time at the second peak load to the GraFEA prediction. Although the load values are over-predicted at some load peaks, the GraFEA simulation predicts the impulse response of the experimental data well. (b) Normalized computational time from the simulation of low-speed impact fracture in gypsum-based disc sample. The time is normalized with respect to the total computational time of the CPU sequential mode. The total time is a summation of the explicit time and GraFEA time. The nonlocal step is included in the GraFEA calculation step. The total computational time of the CPU/GPU hybrid mode reduces to 28% of the CPU sequential computing due to the significant speed-up achieved from the nonlocal calculation step. The simulation results are identical for the CPU sequential mode and CPU/GPU hybrid mode.

the comparison of the experimental data and the FEM simulation result shown in Fig. 5.13(a), it can be seen that the GraFEA model is able to quantitatively predict the experimental data to good accuracy.

Note that as observed in the experiments, the numerical prediction also shows several peaks and trough loads occurring at different times [*cf.* Fig. 5.13(a)]. For the j th peak/trough load where integer $j = 1, 2, 3, 4$, it can be seen that the numerically-predicted time at the j th peak/trough load matches well with the experimentally obtained time at the j th peak/trough load. However, the simulated load response is zero from time of approximately 0.6 ms onwards although the experimental data shows a fifth peak load at a time of approximately 0.74 ms. Nevertheless, as a

first-cut attempt, the current GraFEA formulation is able to *independently* predict the experimental load-time impact response to good accord (see Fig. 5.13) given that the material parameters in the model were fit to an experimental force-displacement response conducted under quasi-static conditions, and the GraFEA model is also able to predict the experimentally-determined cracking patterns in the Plaster of Paris samples under low-velocity impact conditions (see Figs. 5.10 and 5.11).

Finally, a note can be made on the computational advance of the present work with regards to the comparison of simulation times between performing GraFEA calculations using a CPU sequential mode and CPU/GPU hybrid mode. The normalized computational times in the gypsum disc impact simulations are shown in Fig. 5.13(b). The time taken at each calculation step is normalized with respect to the total computational time of the CPU sequential mode. The CPU/GPU hybrid mode reduces the total computational time to 28% compared to the CPU sequential mode. The computational time saving is coming from the improved calculation performance from the nonlocal calculation step. The speed-up achieved at the nonlocal step by using CUDA parallel computing is 92 times compared to sequential computing.

6. SUMMARY AND CONCLUSIONS

A multiple cracking model has been developed for simulating quasi-brittle material fracture and the developed numerical model is implemented under the GraFEA framework. A literature survey has been done to characterize the features of the fracture process in quasi-brittle material and the physical characteristics of quasi-brittle fracture is incorporated in the developed numerical model. The key features of the quasi-brittle fracture implemented in the numerical model are follows: (1) a strain-softening behavior, which shows a gradual decrease in stiffness after the peak load is described by the survival probability evolution law; (2) the fracture process zone is realized by integral-based nonlocal strain formulation; (3) a purely kinematical approach to modeling crack opening and closing is introduced for simulating crack closure behavior; and (4) rate-dependent behavior is incorporated in the survival probability evolution law by power law expression. The developed numerical model is used in simulating fracture of quasi-brittle material in various loading rates.

In Chapter 2, a thermodynamically-consistent three-dimensional small-strain-based theory to describe the deformation and fracture in quasi-brittle and brittle elastic solids was presented. The description for fracture at a material point resembles the microplane fracture but the present theory has the following novel features: (a) a probabilistic description of fracture propagation is used, developing evolution equations for the probability of a microcrack occurring at a given location and (b) a kinematical approach to modeling crack opening and closing. The new three-dimensional constitutive theory has been computationally implemented within a Graph-based Finite-Element Analysis framework and it has also been implemented into the dynamics-based Abaqus/Explicit finite-element program through a vectorized user-material subroutine interface. Our computational approach for fracture modeling is intra-element-based, which is central to the GraFEA approach rather than inter-element fracture, as is done in cohesive zone-based numerical methods, together with selective nonlocality where the nonlocality is only for probability evolution motivated by population dynamics models that allows us to perform efficient implementation of the code without

special elements or other numerical artefacts. In particular, it is shown that the computational procedure is able to model crack closure in solids in a robust, relatively-simple and elegant manner.

In Chapter 3, a GraFEA framework developed for modeling deformation and nonlocal fracture in quasi-brittle materials is used to simulate the fracture response of high-strength concrete (HSC) samples under impact loads. By fitting the material parameters in the theory to match a macroscopic force-displacement response obtained from a three-point bending experiment conducted under quasi-static conditions, it is shown that the GraFEA computational method is able to independently validate the experimentally-determined impulse response, obtained from impact experiments conducted under various initial impact speeds imposed by a drop-weight on HSC samples that are 6 to 7 orders of magnitude higher than the quasistatic tests. Furthermore, the GraFEA-based FEM simulations are also able to reproduce experimental crack propagation speeds in a HSC sample under different initial impact speeds to good accord.

In Chapters 4 and 5, a novel nonlocal three-dimensional graph-based finite element approach has been developed and implemented for simulating fracture in quasi-brittle solids as an extension of our previous work in two dimensions. In order to validate the nonlocal aspects of the model, a gypsum-based particulate composite is fabricated with silica particles of specific dimensions and mass fractions, thus the length scale of the material is fixed by the particulate media. The GraFEA fracture model is implemented in a graphics processing unit parallel computing environment that allows substantial speed-up of the simulations in both cases of impact and quasi-static loading conditions. The improvement in computational performance is especially essential for caring out the simulation of parametric study. Comparison of the physical response of this specially designed composite with the three-dimensional nonlocal GraFEA shows that the model is capable of simulating fracture in such materials. Finally, the efficacy of simulating impact response of concrete including crack closure behavior is tested by simulating hammer drop test for the concrete beam sample and cyclic shear loading on the circumferentially notched concrete cylinder sample.

For the future work, the plastic deformation can be introduced to the GraFEA model to predict impact reaction forces more accurately to overcome the current mismatch in peak loads compared

to the experimental data. In the experimentation side, a high-speed camera can be used to validate the damage evolution history of the nonlocal simulation results with the captured crack propagation history. Also, the proposed experiment might help in determining rate-dependency parameters more precisely. Moreover, a further optimization of the GraFEA VUMAT code can be made to reduce wall-clock computation times. Finally, a more detailed experimental programs can be set to explore the effect of aggregate size on the intrinsic fracture length scale.

REFERENCES

[1] Z.-Q. He, Y. Li, T. Xu, Z. Liu, and Z. J. Ma, "Crack-based serviceability assessment of post-tensioned segmental concrete box-girder bridges," *Structures.*, vol. 30, pp. 1097–1108, 2021.

[2] A. Bascoul, "State of the art report—part 2: Mechanical micro-cracking of concrete," *Mater. Struct.*, vol. 29, no. 2, pp. 67–78, 1996.

[3] D. Hordijk, *Local approach to fatigue of concrete*. PhD thesis, Delft University of Technology, 1991.

[4] H. Y. Shin, C. Lawrence, K. R. Kota, P. Thamburaja, A. Srinivasa, T. E. Lacy, and J. Reddy, "Experimental, theoretical and numerical studies on plain concrete fracture in the low-strain rate regime—A state-of-the-art review," *Mech. Adv. Mater. Struct.*, pp. 1–45, 2021.

[5] T. E. Lacy, D. L. McDowell, P. A. Willice, and R. Talreja, "On representation of damage evolution in continuum damage mechanics," *Int. J. Damage Mech.*, vol. 6, no. 1, pp. 62–95, 1997.

[6] T. L. Anderson, *Fracture mechanics: fundamentals and applications*. CRC press, 2017.

[7] Z. P. Bažant, "Size effect in blunt fracture: concrete, rock, metal," *J. Eng. Mech.*, vol. 110, no. 4, pp. 518–535, 1984.

[8] B. Zech and F. Wittmann, "Part ii probabilistic approach to describe the behaviour of materials," *Nucl. Eng. Des.*, vol. 48, no. 2-3, pp. 575–584, 1978.

[9] A. Carpinteri and B. Chiaia, "Multifractal nature of concrete fracture surfaces and size effects on nominal fracture energy," *Mater. Struct.*, vol. 28, no. 8, pp. 435–443, 1995.

[10] M. A. Issa, M. A. Issa, M. S. Islam, and A. Chudnovsky, "Size effects in concrete fracture: Part i, experimental setup and observations," *Int. J. Fracture*, vol. 102, no. 1, pp. 1–24, 2000.

[11] M. A. Issa, M. A. Issa, M. S. Islam, and A. Chudnovsky, "Size effects in concrete fracture–part ii: Analysis of test results," *Int. J. Fracture*, vol. 102, no. 1, pp. 25–42, 2000.

[12] Z. P. Bažant and M. T. Kazemi, "Size dependence of concrete fracture energy determined by rilem work-of-fracture method," *Int. J. Fracture*, vol. 51, no. 2, pp. 121–138, 1991.

[13] Z. M. Wu, R. C. Yu, C. Y. Sun, Y. J. Wang, X. X. Zhang, and X. D. Fei, "A new test method for the complete load-displacement curve of concrete under mixed mode I-II fracture," *Theor. Appl. Fract. Mech.*, vol. 108, no. April, p. 102629, 2020.

[14] V. S. Gopalaratnam and S. P. Shah, "Softening response of plain concrete in direct tension," *J. Am. Concr. Inst.*, vol. 82, no. 3, pp. 310–323, 1985.

[15] L. G. Sorelli, A. Meda, and G. A. Plizzari, "Bending and Uniaxial Tensile Tests on Concrete Reinforced with Hybrid Steel Fibers," *J. Mater. Civil Eng.*, vol. 17, no. 5, pp. 519–527, 2005.

[16] H. Cornelissen, "Constant-amplitude tests on plain concrete in uniaxial tension and tension-compression," *Report: Stevin Laboratory, Concrete Structures 5-84-1*, 1984.

[17] D. Ren and L. Houben, "Determination of Fracture Energy of Early Age Concrete through a Uniaxial Tensile Test on an Un-Notched Specimen," *Materials*, vol. 13, no. 3, pp. 1–15, 2020.

[18] M. R. van Vliet and J. G. M. van Mier, "Experimental investigation of size effect in concrete and sandstone under uniaxial tension," *Eng. Fract. Mech.*, vol. 65, no. 2, pp. 165–188, 2000.

[19] A. Fernández-Canteli, L. Castañón, B. Nieto, M. Lozano, T. Holušová, and S. Seitl, "Determining fracture energy parameters of concrete from the modified compact tension test," *Frattura ed Integrità Strutturale*, vol. 8, no. 30, pp. 383–393, 2014.

[20] M. D. Wei, F. Dai, N. W. Xu, and T. Zhao, "Experimental and numerical investigation of cracked chevron notched Brazilian disc specimen for fracture toughness testing of rock," *Fatigue Fract. Eng. M.*, vol. 41, no. 1, pp. 197–211, 2018.

[21] L. Østergaard and J. F. Olesen, "Comparative study of fracture mechanical test methods for concrete," *Frac. Mech. Conc. Struct.*, pp. 455–462, 2003.

[22] P. E. Petersson, *Crack growth and development of fracture zones in plain concrete and similar materials*. PhD thesis, Lund Institute of Technology, 1981.

[23] H. A. Koermeling and H. W. Reinhardt, "Determination of the fracture energy of normal concrete and epoxy modified concrete," tech. rep., Technische Hogeschool Delft Stevin Lab, 1983.

[24] Z. P. Bažant, J. Kim, and P. A. Pfeiffer, "Nonlinear Fracture Properties from Size Effect Tests," *J. Struct. Eng.*, vol. 112, pp. 289–307, feb 1986.

[25] Z. P. Bažant and Q. Yu, "Universal Size Effect Law and Effect of Crack Depth on Quasi-Brittle Structure Strength," *J. Eng. Mech.*, vol. 135, no. 2, pp. 78–84, 2009.

[26] Y. Tang and H. Chen, "Characterizations on fracture process zone of plain concrete," *J. Civ. Eng. Manag.*, vol. 25, no. 8, pp. 819–830, 2019.

[27] Z. P. Bažant and B. H. Oh, "Crack band theory for fracture of concrete," *Mater. Struct.*, vol. 16, pp. 155–177, 1983.

[28] Z. M. Wu, H. Rong, J. J. Zheng, F. Xu, and W. Dong, "An experimental investigation on the FPZ properties in concrete using digital image correlation technique," *Eng. Fract. Mech.*, vol. 78, no. 17, pp. 2978–2990, 2011.

[29] Y. Yin, Y. Qiao, and S. Hu, "Four-point bending tests for the fracture properties of concrete," *Eng. Fract. Mech.*, vol. 211, no. November 2018, pp. 371–381, 2019.

[30] P. Bocca, A. Carpinteri, and S. Valente, "Size effects in the mixed mode crack propagation: Softening and snap-back analysis," *Eng. Fract. Mech.*, vol. 35, no. 1, pp. 159–170, 1990.

[31] Z. P. Bažant and P. A. Pfeiffer, "Shear fracture tests of concrete," *Mater. Struct.*, vol. 19, no. 2, pp. 111–121, 1986.

[32] S. E. Swartz and N. M. Taha, "Mixed mode crack propagation and fracture in concrete," *Eng. Fract. Mech.*, vol. 35, no. 1, pp. 137–144, 1990.

[33] B. J. Winkler, *Traglastuntersuchungen Von Unbewehrten Und Bewehrten Betonstrukturen Auf Der Grundlage Eines Objektiven Werkstoffgesetze für Beton*. PhD thesis, University of Innsbruck, 2001.

[34] B. Winkler, G. Hofstetter, and H. Lehar, "Application of a constitutive model for concrete to the analysis of a precast segmental tunnel lining," *Int. J. Numer. Anal. Met.*, vol. 28, no. 7-8, pp. 797–819, 2004.

[35] H. Cifuentes, M. Lozano, T. Holušová, F. Medina, S. Seitl, and A. Fernández-Canteli, "Modified Disk-Shaped Compact Tension Test for Measuring Concrete Fracture Properties," *Int. J. Concr. Struct. M.*, vol. 11, no. 2, pp. 215–228, 2017.

[36] Z. P. Bažant, T. B. Belytschko, and T. Chang, "Continuum theory for strain-softening," *J. Eng. Mech.*, vol. 110, no. 12, pp. 1666–1692, 1984.

[37] A. Hillerborg, M. Modeer, and P. E. Petersson, "Analysis of crack formation and crack growth in concrete by means of fracture mechanics and finite elements," *Cem. Concr. Res.*, vol. SP-249, pp. 225–237, 2008.

[38] K. Otsuka and H. Date, "Fracture process zone in concrete tension specimen," *Eng. Fract. Mech.*, vol. 65, pp. 111–131, 2000.

[39] E. Lorentz, "A nonlocal damage model for plain concrete consistent with cohesive fracture," *Int. J. Fracture*, vol. 207, no. 2, pp. 123–159, 2017.

[40] Z. P. Bažant and F. Lin, "Nonlocal smeared cracking model for concrete fracture," *J. Struct. Eng.*, vol. 114, no. 11, pp. 2493–2510, 1988.

[41] M. Jirásek, "Non-local damage mechanics with application to concrete," *Revue française de génie civil*, vol. 8, no. 5-6, pp. 683–707, 2004.

[42] Z. P. Bažant and G. Pijaudier-Cabot, "Measurement of characteristic length of nonlocal continuum," *J. Eng. Mech.*, vol. 115, no. 4, pp. 7557–767, 1989.

[43] C. Giry, F. Dufour, and J. Mazars, "Stress-based nonlocal damage model," *Int. J. Solids Struct.*, vol. 48, no. 25-26, pp. 3431–3443, 2011.

[44] R. H. Peerlings, M. G. Geers, R. De Borst, and W. A. Brekelmans, "A critical comparison of nonlocal and gradient-enhanced softening continua," *Int. J. Solids Struct.*, vol. 38, no. 44-45, pp. 7723–7746, 2001.

[45] R. H. Peerlings, R. de Borst, W. A. Brekelmans, and M. G. Geers, "Gradient-enhanced damage modelling of concrete fracture," *Mech. Cohes.-Frict. Mat.*, vol. 3, no. 4, pp. 323–342, 1998.

[46] I. Zreid and M. Kaliske, "Regularization of microplane damage models using an implicit gradient enhancement," *Int. J. Solids Struct.*, vol. 51, no. 19-20, pp. 3480–3489, 2014.

[47] J. H. de Vree, W. A. Brekelmans, and M. A. van Gils, "Comparison of nonlocal approaches in continuum damage mechanics," *Comput. Struct.*, vol. 55, no. 4, pp. 581–588, 1995.

[48] L. H. Poh and S. Swaddiwudhipong, "Over-nonlocal gradient enhanced plastic-damage model for concrete," *Int. J. Solids Struct.*, vol. 46, no. 25-26, pp. 4369–4378, 2009.

[49] A. P. Kfouri and K. J. Miller, "Stress, displacement, line integral and closure energy determinations of crack tip stress intensity factors," *Int. J. Pres. Ves. Pip.*, vol. 2, no. 3, pp. 179–191, 1974.

[50] Z. P. Bažant and P. G. Gambarova, "Crack shear in concrete: Crack band microplane model," *J. Struct. Eng.*, vol. 110, no. 9, pp. 2015–2035, 1984.

[51] A. P. Gómez, N. Moës, and C. Stolz, "Comparison between thick level set (tls) and cohesive zone models," *Adv. Model. and Simul. in Eng. Sci.*, vol. 2, no. 1, pp. 1–22, 2015.

[52] T. Hasegawa and Z. P. Bažant, "Nonlocal microplane concrete model with rate effect and load cycles. i: General formulation," *J. Mater. Civ. Eng.*, vol. 5, no. 3, pp. 372–393, 1993.

[53] J. Ožbolt, Y. Li, and I. Kožar, "Microplane model for concentre with relaxed kinematic constraint," *Int. J. Solids. Struct.*, vol. 38, no. 16, pp. 2683–2711, 2001.

[54] F. C. Caner and Z. P. Bažant, "Microplane model m7 for plain concrete. i: Formulation," *J. Eng. Mech.*, vol. 139, no. 12, pp. 1714–1723, 2013.

[55] Z. P. Bažant and G. Di Luzio, "Nonlocal microplane model with strain-softening yield limits," *Int. J. Solids Struct.*, vol. 41, no. 24-25, pp. 7209–7240, 2004.

[56] B. Sun, "A continuum damage mechanics method for fracture simulation of quasi-brittle materials," *Fatigue Fract. Eng. Mater. Struct.*, vol. 43, no. 8, pp. 1837–1850, 2020.

[57] N. Liu, X. Cui, J. Xiao, J. Lua, and N. Phan, "A simplified continuum damage mechanics based modeling strategy for cumulative fatigue damage assessment of metallic bolted joints," *Int. J. Fatigue*, vol. 131, p. 105302, 2020.

[58] J. Mazars and G. Pijaudier-Cabot, "Continuum Damage Theory—Application to Concrete," *J. Eng. Mech.*, vol. 115, pp. 345–365, 1989.

[59] E. Zafati and B. Richard, "Anisotropic continuum damage constitutive model to describe the cyclic response of quasi-brittle materials: The regularized unilateral effect," *Int. J. Solids Struct.*, vol. 162, pp. 164–180, 2019.

[60] B. Richard, F. Ragueneau, C. Cremona, and L. Adelaide, "Isotropic continuum damage mechanics for concrete under cyclic loading: Stiffness recovery, inelastic strains and frictional sliding," *Eng. Fract. Mech.*, vol. 77, no. 8, pp. 1203–1223, 2010.

[61] J. Lemaître and J. Chaboche, *Solid material mechanics*. Dunod, 2004.

[62] M. Hassanzadeh, *Behavior of fracture process zones in concrete influenced by simultaneously applied normal and shear displacements*. PhD thesis, Lund Institute of Technology, 1991.

[63] E. Schlangen, *Experimental and numerical analysis of fracture processes in concrete*. PhD thesis, Delft University of Technology, 1993.

[64] M. Brünig and A. Michalski, "A stress-state-dependent continuum damage model for concrete based on irreversible thermodynamics," *Int. J. Plasticity*, vol. 90, pp. 31 – 43, 2017.

[65] M. Brünig, "A framework for large strain elastic–plastic damage mechanics based on metric transformations," *Int. J. Eng. Sci.*, vol. 39, no. 9, pp. 1033 – 1056, 2001.

[66] C. Chow and J. Wang, "An anisotropic theory of continuum damage mechanics for ductile fracture," *Eng. Fract. Mech.*, vol. 27, no. 5, pp. 547 – 558, 1987.

[67] H. Kupfer, H. K. Hilsdorf, and H. Rüsch, "Behavior of concrete under biaxial stresses," *J. Am. Concr. Inst.*, vol. 66, pp. 656 – 666, 1969.

[68] C. La Borderie, Y. Berthaud, and G. Pijaudier-Cabot, "Crack closure effect in continuum damage mechanics: numerical implementation," in *Proc. 2nd Int. Conf. on'Computer aided analysis and design of concrete strucutures'. Zell am See, Austria*, pp. 975–986, 1990.

[69] M. Jirásek, "Non-local damage mechanics with application to concrete," *Revue française de génie civil*, vol. 8, no. 5-6, pp. 683–707, 2004.

[70] Y. Wang and H. Waisman, "From diffuse damage to sharp cohesive cracks: A coupled xfem framework for failure analysis of quasi-brittle materials," *Comput. Methods Appl. Mech. Eng.*, vol. 299, pp. 57–89, 2015.

[71] S. Zhou, X. Zhuang, H. Zhu, and T. Rabczuk, "Phase field modelling of crack propagation, branching and coalescence in rocks," *Theor. Appl. Fract. Mec.*, vol. 96, pp. 174–192, 2018.

[72] C. Miehe, F. Welschinger, and M. Hofacker, "Thermodynamically consistent phase-field models of fracture: Variational principles and multi-field FE implementations," *Int. J. Numer. Meth. Eng.*, vol. 83, no. 10, pp. 1273–1311, 2010.

[73] J. Kiendl, M. Ambati, L. De Lorenzis, H. Gomez, and A. Reali, "Phase-field description of brittle fracture in plates and shells," *Comput. Methods Appl. Mech. Eng.*, vol. 312, pp. 374–394, 2016.

[74] M. J. Borden, C. V. Verhoosel, M. A. Scott, T. J. Hughes, and C. M. Landis, "A phase-field description of dynamic brittle fracture," *Comput. Methods Appl. Mech. Eng.*, vol. 217-220, pp. 77–95, 2012.

[75] J. Y. Wu, "A unified phase-field theory for the mechanics of damage and quasi-brittle failure," *J. Mech. Phys. Solids.*, vol. 103, pp. 72–99, jun 2017.

[76] S. Narayan and L. Anand, "A gradient-damage theory for fracture of quasi-brittle materials," *J. Mech. Phys. Solids*, vol. 129, pp. 119–146, 2019.

[77] S. A. Silling, "Reformulation of elasticity theory for discontinuities and long-range forces," *J. Mech. Phys. Solids*, vol. 48, no. 1, pp. 175–209, 2000.

[78] S. A. Silling and E. Askari, "A meshfree method based on the peridynamic model of solid mechanics," *Comput. Struct.*, vol. 83, no. 17-18, pp. 1526–1535, 2005.

[79] T. Ni, Q. Zhu, L. Y. Zhao, and P. F. Li, "Peridynamic simulation of fracture in quasi brittle solids using irregular finite element mesh," *Eng. Fract. Mech.*, vol. 188, pp. 320–343, 2018.

[80] B. Kilic and E. Madenci, "An adaptive dynamic relaxation method for quasi-static simulations using the peridynamic theory," *Theor. Appl. Fract. Mec.*, vol. 53, no. 3, pp. 194–204, 2010.

[81] A. Tabiei and J. Wu, "Development of the DYNA3D simulation code with automated fracture procedure for brick elements," *Int. J. Numer. Meth. Eng.*, vol. 57, no. 14, pp. 1979–2006, 2003.

[82] D. Yang, X. He, S. Yi, and X. Liu, "An improved ordinary state-based peridynamic model for cohesive crack growth in quasi-brittle materials," *Int. J. Mech. Sci.*, vol. 153, pp. 402–415, 2019.

[83] S. A. Silling, M. Epton, O. Weckner, J. Xu, and E. Askari, "Peridynamic states and constitutive modeling," *J. Elasticity*, vol. 88, no. 2, pp. 151–184, 2007.

[84] E. Madenci, "Peridynamic integrals for strain invariants of homogeneous deformation," *Appl. Math. Mech.*, vol. 97, no. 10, pp. 1236–1251, 2017.

[85] D. Huang, G. Lu, and P. Qiao, "An improved peridynamic approach for quasi-static elastic deformation and brittle fracture analysis," *Int. J. Mech. Sci.*, vol. 94-95, pp. 111–122, 2015.

[86] H. W. Reinhardt, H. A. W. Cornelissen, and D. A. Hordijk, "Tensile Tests and Failure Analysis of Concrete," *J. Struct. Eng.*, vol. 112, no. 11, pp. 2462–2477, 1986.

[87] J. C. Gálvez, M. Elices, G. V. Guinea, and J. Planas, "Mixed mode fracture of concrete under proportional and nonproportional loading," *Int. J. Fracture*, vol. 94, no. 3, pp. 267–284, 1998.

[88] N. Rossi Cabral, M. A. Invaldi, R. Barrios D'Ambra, and I. Iturrioz, "An alternative bilinear peridynamic model to simulate the damage process in quasi-brittle materials," *Eng. Fract. Mech.*, vol. 216, p. 106494, 2019.

[89] A. Hillerborg, "The fictitious crack model and its use in numerical analyses," *Fract. Mech. Eng. Appl.*, pp. 667–669, 1979.

[90] N. Zhu, D. De Meo, and E. Oterkus, "Modelling of granular fracture in polycrystalline materials using ordinary state-based peridynamics," *Materials*, vol. 9, no. 12, p. 977, 2016.

[91] M. R. A. Van Vliet and J. G. M. Van Mier, "Size effect in tensile fracture of concrete and rock," *Heron*, vol. 45, pp. 91–108, 2000.

[92] P. Wu, J. Zhao, Z. Chen, and F. Bobaru, "Validation of a stochastically homogenized peridynamic model for quasi-static fracture in concrete," *Eng. Fract. Mech.*, vol. 237, p. 107293, 2020.

[93] Z. Chen, S. Niazi, and F. Bobaru, "A peridynamic model for brittle damage and fracture in porous materials," *Int. J. Rock Mech. Min.*, vol. 122, p. 104059, 2019.

[94] Y. D. Ha and F. Bobaru, "Studies of dynamic crack propagation and crack branching with peridynamics," *Int. J. Fract.*, vol. 162, pp. 229–244, 2010.

[95] Z. Xu, G. Zhang, Z. Chen, and F. Bobaru, "Elastic vortices and thermally-driven cracks in brittle materials with peridynamics," *Int. J. Fracture*, vol. 209, no. 1-2, pp. 203–222, 2018.

[96] A. Vervuurt, J. G. Van Mier, and E. Schlangen, "Analyses of anchor pull-out in concrete," *Mater. Struct.*, vol. 27, no. 5, pp. 251–259, 1994.

[97] T. Belytschko, R. Gracie, and G. Ventura, "A review of extended/generalized finite element methods for material modeling," *Model. Simul. Mater. Sc.*, vol. 17, p. 043001, 2009.

[98] N. Moës and T. Belytschko, "Extended finite element method for cohesive crack growth," *Eng. Fract. Mech.*, vol. 69, no. 7, pp. 813–833, 2002.

[99] J. F. Unger, S. Eckardt, and C. Könke, "Modelling of cohesive crack growth in concrete structures with the extended finite element method," *Comput. Methods Appl. Mech. Eng.*, vol. 196, no. 41, pp. 4087–4100, 2007.

[100] A. Zamani, R. Gracie, and M. Eslami, "Cohesive and non-cohesive fracture by higher-order enrichment of xfem," *Int. J. Numer. Meth. Eng.*, vol. 90, no. 4, pp. 452–483, 2012.

[101] S.-N. Roth, P. Léger, and A. Soulaïmani, "A combined XFEM–damage mechanics approach for concrete crack propagation," *Comput. Methods Appl. Mech. Eng.*, vol. 283, pp. 923–955, 2015.

[102] M. Elices, G. Guinea, J. Gómez, and J. Planas, "The cohesive zone model: advantages, limitations and challenges," *Eng. Fract. Mech.*, vol. 69, no. 2, pp. 137–163, 2002.

[103] K. Park and G. H. Paulino, "Cohesive Zone Models: A Critical Review of Traction-Separation Relationships Across Fracture Surfaces," *Appl. Mech. Rev.*, vol. 64, no. 6, p. 060802, 2013.

[104] M. G. Tijssens, B. L. Sluys, and E. van der Giessen, "Numerical simulation of quasi-brittle fracture using damaging cohesive surfaces," *Eur. J. Mech. A-Solid*, vol. 19, no. 5, pp. 761–779, 2000.

[105] J. Roesler, G. H. Paulino, K. Park, and C. Gaedicke, "Concrete fracture prediction using bilinear softening," *Cem. Concr. Compos.*, vol. 29, no. 4, pp. 300–312, 2007.

[106] Z. Yang, X. Su, J. Chen, and G. Liu, "Monte carlo simulation of complex cohesive fracture in random heterogeneous quasi-brittle materials," *Int. J. Solids Struct.*, vol. 46, no. 17, pp. 3222–3234, 2009.

[107] T. Most and C. Bucher, "Energy-based simulation of concrete cracking using an improved mixed-mode cohesive crack model within a meshless discretization," *Int. J. Numer. Anal. Met.*, vol. 31, no. 2, pp. 285–305, 2007.

[108] P. Grassl, "A lattice approach to model flow in cracked concrete," *Cem. Concr. Compos.*, vol. 31, no. 7, pp. 454–460, 2009.

[109] M. Abdellatef and M. Alnaggar, "Energy-Based Coarse Graining of the Lattice-Discrete Particle Model," *J. Eng. Mech.*, vol. 146, no. 5, p. 04020026, 2020.

[110] M. Alnaggar, G. Cusatis, and G. Di Luzio, "Lattice Discrete Particle Modeling (LDPM) of Alkali Silica Reaction (ASR) deterioration of concrete structures," *Cem. Concr. Compos.*, vol. 41, pp. 45–59, 2013.

[111] P. Grassl, D. Grégoire, L. Rojas Solano, and G. Pijaudier-Cabot, "Meso-scale modelling of the size effect on the fracture process zone of concrete," *Int. J. Solids Struct.*, vol. 49, no. 13, pp. 1818–1827, 2012.

[112] A. Fascetti, J. E. Bolander, and N. Nisticó, "Lattice Discrete Particle Modeling of Concrete under Compressive Loading: Multiscale Experimental Approach for Parameter Determination," *J. Eng. Mech.*, vol. 144, no. 8, p. 04018058, 2018.

[113] M. Abdellatef, J. Vorel, R. Wan-Wendner, and M. Alnaggar, "Predicting Time-Dependent Behavior of Post-Tensioned Concrete Beams: Discrete Multiscale Multiphysics Formulation," *J. Struct. Eng.*, vol. 145, no. 7, p. 04019060, 2019.

[114] H. Chen, E. Lin, Y. Jiao, and Y. Liu, "A generalized 2D non-local lattice spring model for fracture simulation," *Comput. Mech.*, vol. 54, no. 6, pp. 1541–1558, 2014.

[115] L. Davison and A. Stevens, "Thermomechanical constitution of spalling elastic bodies," *J. Appl. Phys.*, vol. 44, pp. 667–674, 1973.

[116] J. Marshal, P. M. Naghdi, and A. R. Srinivasa, "A macroscopic theory of microcrack growth in brittle materials," *Philos. Trans. Royal Soc. A.*, vol. 335, pp. 455–485, 1991.

[117] Z. P. Bažant, Y. Xiang, and P. C. Prat, "Microplane model for concrete. i: Stress-strain boundaries and finite strain," *J. Eng. Mech.*, vol. 122, no. 3, pp. 245–254, 1996.

[118] D. A. Birch and W. R. Young, "A master equation for a spatial population model with pair interactions," *Theor. Popul. Biol.*, vol. 70, no. 1, pp. 26–42, 2006.

[119] P. Khodabakhshi, J. N. Reddy, and A. Srinivasa, "GraFEA: a graph-based finite element approach for the study of damage and fracture in brittle materials," *Meccanica*, vol. 51, pp. 3129–3147, 2016.

[120] P. Khodabakhshi, J. N. Reddy, and A. Srinivasa, "A nonlocal fracture criterion and its effect on the mesh dependency of grafea," *Acta Mechanica*, vol. 230, pp. 3593–3612, 2019.

[121] M. Doi, "Stochastic theory of diffusion-controlled reaction," *J. Phys. A Math. Theor.*, vol. 9, no. 9, p. 1479, 1976.

[122] M. Galouei and A. Fakhimi, "Size effect, material ductility and shape of fracture process zone in quasi-brittle materials," *Comput. Geotech.*, vol. 65, pp. 126–135, 2015.

[123] J. De Vree, W. Brekelmans, and M. Van Gils, "Comparison of nonlocal approaches in continuum damage mechanics," *Comput. Struct.*, vol. 55, no. 4, pp. 581–588, 1995.

[124] G. Pijaudier-Cabot and Z. Bažant, "Nonlocal damage theory," *J. Eng. Mech.*, vol. 113, pp. 1512–1533, 1987.

[125] R. H. Peerlings, R. de Borst, W. A. Brekelman, and M. G. Geers, "Gradient-enhanced damage modelling of concrete fracture," *Mech. Cohes. Frict. Mat.*, vol. 3, pp. 323–342, 1998.

[126] P. Thamburaja, K. Sarah, A. Srinivasa, and J. N. Reddy, "Fracture of viscoelastic materials: Fem implementation of a non-local & rate form-based finite-deformation constitutive theory," *Comput. Methods Appl. Mech. Eng.*, vol. 354, pp. 871–903, 2019.

[127] Z. Bažant and R. Gettu, "Rate effects and load relaxation in static fracture of concrete," *ACI Materials Journal*, vol. 89, pp. 456–468, 1992.

[128] L. J. Malvar and J. E. Crawford, *Dynamic increase factors for concrete*. Naval Facilities Engineering Service Center, 1998.

[129] Z. Bažant, F. Caner, M. Adley, and S. Akers, "Fracturing rate effect and creep in microplane model for dynamics," *J. Eng. Mech.*, vol. 126, pp. 962–970, 2000.

[130] G. Cusatis, "Strain-rate effects on concrete behavior," *Int. J. Impact Eng.*, vol. 38, pp. 162–170, 2011.

[131] Abaqus/Explicit, *Reference manuals*. Simulia-Dassault Systémes, 2021.

[132] Z. P. Bažant and P. C. Prat, "Measurement of mode III fracture energy of concrete," *Nucl. Eng. Des.*, vol. 106, no. 1, pp. 1–8, 1988.

[133] C. Miehe, L. Schaenzel, and H. Ulmer, "Phase field modeling of fracture in multi-physics problems. part i. balance of crack surface and failure criteria for brittle crack propagation in thermo-elastic solids," *Comput. Methods Appl. Mech. Eng.*, vol. 294, pp. 449–485, 2015.

[134] A. Dancygier and D. Yankelevsky, "High strength concrete response to hard projectile impact," *Int. J. Impact Eng.*, vol. 18, no. 6, pp. 583–599, 1996.

[135] V. Kodur and L. Phan, "Critical factors governing the fire performance of high strength concrete systems," *Fire Safety J.*, vol. 42, no. 6-7, pp. 482–488, 2007.

[136] N. Pauzi, M. Jamil, R. Hamid, A. Abdin, and M. Zain, "The effects of using cathode ray tube (crt) glass as coarse aggregates in high-strength concrete subjected to high temperature," *J. Mater. Cycles Waste. Manag*, vol. 21, no. 6, pp. 1414–1425, 2019.

[137] X. X. Zhang, C. Y. Rena, G. Ruiz, M. Tarifa, and M. A. Camara, "Effect of loading rate on crack velocities in hsc," *Int. J. Impact Eng.*, vol. 37, no. 4, pp. 359–370, 2010.

[138] S. Peng, C. Rong, H. Cheng, X. Wang, M. Li, B. Tang, and X. Li, "Mechanical properties of high-strength high-performance reinforced concrete shaft lining structures in deep freezing wells," *Adv. Civil Eng.*, vol. 21, pp. 69–78, 2019.

[139] R. C. Yu, L. Saucedo, G. Ruiz, and X. Zhang, "Eight types of HSC," *Appl. Mech. Mater.*, vol. 147, pp. 293–297, 2012.

[140] P. Thamburaja, K. Sarah, A. Srinivasa, and J. N. Reddy, "Fracture modeling of plain concrete using nonlocal fracture mechanics and a graph-based computational framework," *Proc. R. Soc. A.*, vol. 477, no. 2252, p. 20210398, 2021.

[141] X. X. Zhang, G. Ruiz, R. Yu, and M. Tarifa, "Fracture behaviour of high-strength concrete at a wide range of loading rates," *Int. J. Impact Eng.*, vol. 36, no. 10-11, pp. 1204–1209, 2009.

[142] R. Wendner, J. Vorel, J. Smith, C. G. Hoover, Z. P. Bažant, and G. Cusatis, "Characterization of concrete failure behavior: a comprehensive experimental database for the calibration and validation of concrete models," *Mater. Struct.*, vol. 48, no. 11, pp. 3603–3626, 2015.

[143] N. Banthia, S. Mindess, and A. Bentur, "Impact behaviour of concrete beams," *Mater. Struct.*, vol. 20, no. 4, pp. 293–302, 1987.

[144] P. Sukontasukkul, *Impact behaviour of concrete under multiaxial loading*. PhD thesis, The University of British Columbia, 2001.

[145] X. X. Zhang, R. C. Yu, G. Ruiz, M. Tarifa, and M. A. Camara, "Effect of loading rate on crack velocities in HSC," *Int. J. Impact Eng.*, vol. 37, no. 4, pp. 359–370, 2010.

[146] H. Shin, P. Thamburaja, A. Srinivasa, and J. Reddy, "Modeling impact fracture in a quasi-brittle solids using a 3d nonlocal graph-based finite element analysis: Theory, finite element simulations, and experimental verification," *J. Mech. Phys. Solids.*, vol. 170, p. 105097, 2023.

[147] M. Elices and C. Rocco, "Effect of aggregate size on the fracture and mechanical properties of a simple concrete," *Eng. Fract. Mech.*, vol. 75, pp. 3839–3851, 2008.

[148] H. Y. Shin, P. Thamburaja, A. Srinivasa, and J. N. Reddy, "On simulating impact fracture in high-strength concrete using GraFEA," *Extreme Mech. Lett.*, vol. 52, p. 101618, 2022.

[149] P. V. Sáez, M. del Río Merino, M. Sorrentino, C. P. Amores, J. S. Cruz Astorqui, and C. V. Arrebola, "Mechanical characterization of gypsum composites containing inert and insulation materials from construction and demolition waste and further application as a gypsum block," *Materials.*, vol. 13, no. 1, pp. 1–14, 2020.

[150] D. Ferrández, M. Álvarez, P. Saiz, and A. Zaragoza, "Experimental Study with Plaster Mortars Made with Recycled Aggregate and Thermal Insulation Residues for Application in Building," *Sustainability.*, vol. 14, no. 4, 2022.

[151] L. Boquera, E. Olacia, C. Fabiani, A. L. Pisello, A. D'Alessandro, F. Ubertini, and L. F. Cabeza, "Thermo-acoustic and mechanical characterization of novel bio-based plasters: The valorisation of lignin as by-product from biomass extraction for green building applications," *Constr. Build. Mater.*, vol. 278, p. 122373, 2021.

[152] S. Mindess and C. Yan, "Perforatin of plain and fibre reinforced concretes subjected to low-velocity impact loading," *Cem. Concr. Res.*, vol. 23, pp. 83–92, 1993.

[153] Y. Cai, X. Cui, G. Li, and W. Liu, "A parallel finite element procedure for contact-impact problems using edge-based smooth triangular element and GPU," *Comput. Phys. Commun.*, vol. 225, pp. 47–58, 2018.

[154] W. Zhang, Z. hao Zhong, C. Peng, W. hai Yuan, and W. Wu, "GPU-accelerated smoothed particle finite element method for large deformation analysis in geomechanics," *Comput. Geotech.*, vol. 129, no. September 2020, p. 103856, 2021.

[155] A. Eghtesad, K. Germaschewski, and M. Knezevic, "Coupling of a multi-GPU accelerated elasto-visco-plastic fast Fourier transform constitutive model with the implicit finite element method," *Comput. Mater. Sci.*, vol. 208, no. March, p. 111348, 2022.

[156] A. C. Eringen and D. G. Edelen, "On nonlocal elasticity," *Int. J. Eng. Sci.*, vol. 10, no. 3, pp. 233–248, 1972.

[157] Z. P. Bazant and G. Pijaudier-Cabot, "Nonlocal continuum damage, localization instability and convergence," *J. Appl. Mech.*, no. 88, 1988.

[158] A. R. Srinivasa, H. Y. Shin, P. Thamburaja, and J. N. Reddy, "Multiple cracking model in a 3D GraFEA framework," *Contin. Mech. Thermodyn.*, vol. 33, no. 4, pp. 1409–1428, 2021.

[159] A. Lisjak, O. K. Mahabadi, L. He, B. S. Tatone, P. Kaifosh, S. A. Haque, and G. Grasselli, "Acceleration of a 2D/3D finite-discrete element code for geomechanical simulations using General Purpose GPU computing," *Comput. Geotech.*, vol. 100, no. March, pp. 84–96, 2018.

[160] Z. Zheng, M. Zang, S. Chen, and H. Zeng, "A GPU-based DEM-FEM computational framework for tire-sand interaction simulations," *Comput. Struct.*, vol. 209, pp. 74–92, 2018.

[161] X. Su, Q. Liang, and X. Xia, "A new GPU-accelerated coupled discrete element and depth-averaged model for simulation of flow-like landslides," *Environ. Model. Softw.*, vol. 153, no. March, p. 105412, 2022.

[162] H. Le Minh, S. Khatir, M. Abdel Wahab, and T. Cuong-Le, "A concrete damage plasticity model for predicting the effects of compressive high-strength concrete under static and dynamic loads," *J. Build. Eng.*, vol. 44, no. July, p. 103239, 2021.

[163] O. Gencel, J. J. Del Coz Diaz, M. Sutcu, F. Koksal, F. P. Alvarez Rabanal, G. Martinez-Barrera, and W. Brostow, "Properties of gypsum composites containing vermiculite and polypropylene fibers: Numerical and experimental results," *Energy. Build.*, vol. 70, pp. 135–144, 2014.

[164] C. Mayo-Corrochano, L. J. Sánchez-Aparicio, J. R. Aira, D. Sanz-Arauz, E. Moreno, and J. Pinilla Melo, "Assessment of the elastic properties of high-fired gypsum using the digital image correlation method," *Constr. Build. Mater.*, vol. 317, 2022.

[165] S. Chandrasekhar, "Stochastic problems in physics and astronomy," *Rev. Mod. Phys.*, vol. 15, no. 1, p. 1, 1943.

[166] D.-B. Zhao, W.-J. Yi, and S. K. Kunnath, “Shear Mechanisms in Reinforced Concrete Beams under Impact Loading,” *J. Struct. Eng.*, vol. 143, no. 9, 2017.